A national laboratory of the U.S. Department of Energy
Office of Energy Efficiency & Renewable Energy

NREL National Renewable Energy Laboratory

Innovation for Our Energy Future

Subcontract Report
NREL/SR-520-43909
August 2008

Identifying the Electronic Properties Relevant to Improving the Performance of High Band-Gap Copper Based I-III-VI_2 Chalcopyrite Thin Film Photovoltaic Devices

Final Subcontract Report
27 April 2004 – 15 September 2007

J.D. Cohen
University of Oregon
Eugene, Oregon

NREL is operated by Midwest Research Institute • Battelle   Contract No. DE-AC36-99-GO10337

Identifying the Electronic Properties Relevant to Improving the Performance of High Band-Gap Copper Based I-III-VI_2 Chalcopyrite Thin Film Photovoltaic Devices

Subcontract Report
NREL/SR-520-43909
August 2008

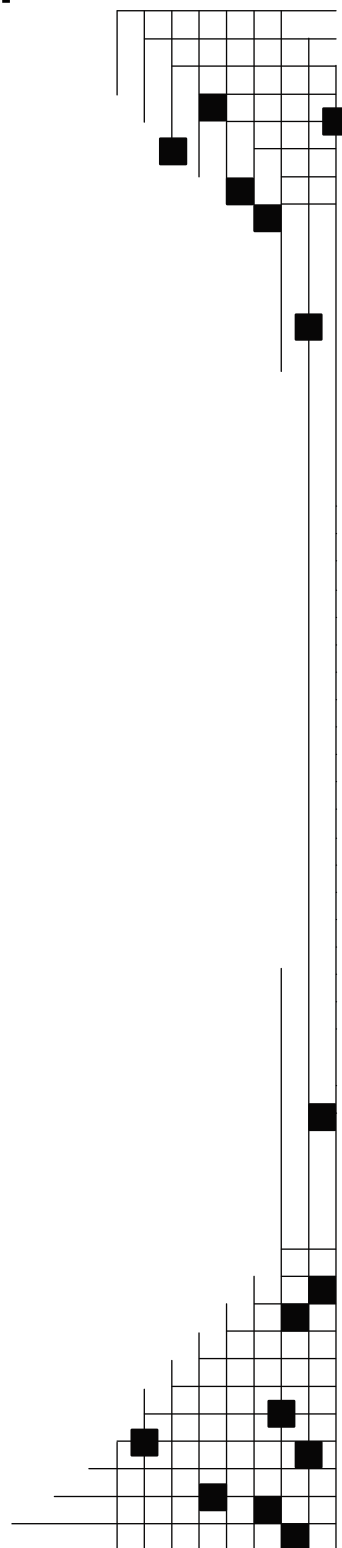

Final Subcontract Report
27 April 2004 – 15 September 2007

J.D. Cohen
University of Oregon
Eugene, Oregon

NREL Technical Monitor: Fannie Posey Eddy

Prepared under Subcontract No. XAT-4-33624-08

National Renewable Energy Laboratory
1617 Cole Boulevard, Golden, Colorado 80401-3393
303-275-3000 • www.nrel.gov

Operated for the U.S. Department of Energy
Office of Energy Efficiency and Renewable Energy
by Midwest Research Institute • Battelle

Contract No. DE-AC36-99-GO10337

This publication was reproduced from the best available copy submitted by the subcontractor and received no editorial review at NREL

NOTICE

This report was prepared as an account of work sponsored by an agency of the United States government. Neither the United States government nor any agency thereof, nor any of their employees, makes any warranty, express or implied, or assumes any legal liability or responsibility for the accuracy, completeness, or usefulness of any information, apparatus, product, or process disclosed, or represents that its use would not infringe privately owned rights. Reference herein to any specific commercial product, process, or service by trade name, trademark, manufacturer, or otherwise does not necessarily constitute or imply its endorsement, recommendation, or favoring by the United States government or any agency thereof. The views and opinions of authors expressed herein do not necessarily state or reflect those of the United States government or any agency thereof.

Available electronically at http://www.osti.gov/bridge

Available for a processing fee to U.S. Department of Energy and its contractors, in paper, from:
U.S. Department of Energy
Office of Scientific and Technical Information
P.O. Box 62
Oak Ridge, TN 37831-0062
phone: 865.576.8401
fax: 865.576.5728
email: mailto:reports@adonis.osti.gov

Available for sale to the public, in paper, from:
U.S. Department of Commerce
National Technical Information Service
5285 Port Royal Road
Springfield, VA 22161
phone: 800.553.6847
fax: 703.605.6900
email: orders@ntis.fedworld.gov
online ordering: http://www.ntis.gov/ordering.htm

Printed on paper containing at least 50% wastepaper, including 20% postconsumer waste

PREFACE

This Final Subcontract Report covers the work performed at the University of Oregon for the period 27 May 2004 to 15 September 2007 under NREL Subcontract Number XAT-4-33624-08. The following personnel participated in this research program:

NAME	TITLE	WORK PERFORMED
J. David Cohen	Professor, Principal Investigator	Program Manager
Jennifer T. Heath	Assistant Professor, Linfield College. 2nd-Tier Subcontractor	Metastable effects in CIGS due to forward bias current injection and light exposure. Studies of CGS sample devices.
Adam Halverson	Research Assistant	Studies of the electronic properties of the sulfur containing (CISS and CIGSS) chalcopyrite materials.
JinWoo Lee	Research Assistant	Employing light-induced metastable effects in CIGS to deduce the effects of deep defects on device performance.
David Berney Needleman	Undergraduate Researcher	Studies of bifacial CIGS solar cells (with JinWoo Lee)

TABLE OF CONTENTS

Page

LIST OF ILLUSTRATIONS vi

LIST OF TABLES ix

EXECUTIVE SUMMARY x

1.0 INTRODUCTION 1

2.0 SAMPLES 2

2.1 INSTITUTE OF ENERGY CONVERSION SAMPLES 2

2.2 NREL COPPER GALLIUM DISELENIDE DEVICES 4

3.0 EXPERIMENTAL CHARACTERIZATION METHODS 5

3.1 ADMITTANCE SPECTROSCOPY 5

3.2 DRIVE LEVEL CAPACITANCE PROFILING (DLCP) 6

3.3 TRANSIENT PHOTOCAPACITANCE AND PHOTOCURRENT SPECTROSCOPY 7

4.0 RESULTS FOR THE SULFUR CONTAINING ALLOY SAMPLES 8

4.1 THE QUATERNARY COPPER INDIUM SELENIUM SULFUR (CISS) ALLOYS 8

4.2 PROPERTIES OF THE COPPER INDIUM DISULFIDE ENDPOINT 11

4.3 PROPERTIES OF COPPER INDIUM GALLIUM DISELENIDE-SULFIDE (CIGSS) PENTENARY SAMPLES WITH BANDGAPS NEAR 1.5 eV 14

4.3.1 General Electronic Properties 14

4.3.2 Temperature Dependence of Sub-Band-Gap Spectra 16

4.4 CIGSS PENTENARY SAMPLES WITH A CONSTANT S:Se = 1:3 RATIO 20

4.5 CIGSS ALLOYS: ELECTRONIC PROPERTIES vs. CELL PERFORMANCE 22

5.0 RESULTS FOR THE $CuGaSe_2$ DEVICES 26

5.1 COMPOSITION UNIFORMITY ISSUES 27

5.2 CURRENT-VOLTAGE CHARACTERISTICS 28

5.3 CAPACITANCE PROFILING MEASUREMENTS 29

6.0 NUMERICAL MODELING OF DLCP AND CV-PROFILING DATA 31

6.1 MOTIVATION 31

6.2 MODELING DETAILS WITH EXAMPLES 32

7.0 METASTABILITY STUDIES TO INVESTIGATE THE ROLE OF DEEP ACCEPTOR STATES IN LIMITING CIGS DEVICE PERFORMANCE 37

7.1 GENERAL ASPECTS OF METASTABLE CHANGES IN CIGS 37

7.1.1 Experimental Procedures 37

7.1.2 Experimental Results 38

7.1.3 Analysis 39

7.2 THE EFFECTS OF METASTABLE CHANGES ON THE CELL PERFORMANCE 41

7.3 ANALYSIS AND MODELING 43

7.4 BIFACIAL CELL RESULTS AND MODELING 46

8.0 MEASURING HOLE MOBILITIES IN WORKING CIGS SOLAR CELLS 48

8.1 CIGS CONDUCTIVITIES FROM HIGH FREQUENCY ADMITTANCE MEASUREMENTS 49

8.2 DETERMINATING THE HOLE CARRIER MOBILITIES 52

8.3 HOLE MOBILITIES VERSUS METASTABILITY IN CIGS 54

8.4 DISCUSSION REGARDING HOLE MOBILITY MEASUREMENTS 55

9.0 CONCLUSIONS AND FUTURE DIRECTIONS 56

10.0 SUBCONTRACT SUPPORTED PUBLICATIONS 59

11.0 REFERENCES 60

LIST OF ILLUSTRATIONS

Page

FIG. 1. Diagram indicating the compositions of the $Cu(InGa)Se_2$, $CuIn(SeS)_2$, and $Cu(InGa)(SeS)_2$ sample devices provided by IEC 4

FIG. 2 Types of sub-bandgap optical transitions observed in semiconductors 8

FIG. 3. TPC spectra for four $CuIn(SeS)_2$ samples 9

FIG. 4. Capacitance vs. frequency admittance spectra at zero bias over a range of temperatures for the 33at.% and 54at.% sulfur $CuIn(SeS)_2$ samples 9

FIG. 5. Series of DLCP curves for the two mixed Se,S alloy samples 10

FIG. 6. Photocapacitance spectra of the $CuInS_2$ sample at different temperatures 11

FIG. 7. Schematic to explain the temperature dependence of the defect band for the $CuInS_2$ sample 12

FIG. 8. Comparison of a 160K TPC spectrum of the $CuInS_2$ sample with a 150K $CuIn_{0.2}Ga_{0.8}Se_2$ alloy TPC spectrum 12

FIG. 9. Matched photocapacitance and photocurrent spectra on the $CuInS_2$ sample at 280K 13

FIG. 10. Admittance spectra for the five $Cu(InGa)(SeS)_2$ devices of 1.52eV bandgap 14

FIG. 11. DLCP profiles at 170K for the $Cu(InGa)(SeS)_2$ sample with 12at.% Sulfur 15

FIG. 12. Photocapacitance spectra collected near 180K for the four *Cu-poor* $Cu(InGa)(SeS)_2$ samples 15

FIG. 13. Comparison of TPC and TPI spectra at two measurement temperatures for the 33% Ga, 56% S sample and the 51% Ga, 33% S pentenary sample 17

FIG. 14. Defect model wherein a defect is optically filled from the valence band and is emptied thermally into the conduction band 17

FIG. 15. Detailed temperature dependence of the *ratio* between the TPC signal in the defect band region to its value near the bandgap energy for the three pentenary samples.. 18

FIG. 16. Band alignment of the three $Cu(InGa)(SeS)_2$ samples based upon theoretical studies 19

FIG. 17. Detailed temperature dependence of the *ratio* between the TPC signal in the defect band region to its value near the bandgap energy for the 33at.% sulfur pentenary and quaternary samples 20

FIG. 18. C-f-T spectra for all five $Cu(InGa)(SeS)_2$ devices with S:Se ratios near 1:3........ 21

FIG. 19. DLC and CV profiles for IEC CGSSe device 24295 (Ga/III=1, S/VI=0.26) at 30kHz 22

FIG. 20. DLC and CV profiles for IEC CIGSSe device 24440 (Ga/III=0.38, S/VI=0.23) taken at 3.3kHz........ 22

FIG. 21. TPC spectra at 180K for the five constant chalcogen ratio pentenary devices........ 23

FIG. 22 **(a)**Cell efficiencies for a wide range of $Cu(InGa)Se_2$, $CuIn(SeS)_2$ and $Cu(InGa)(SeS)_2$ sample devices fabricated at IEC **(b)** Urbach energies determined from TPC measurements for this same set of samples 24

FIG. 23 The voltage deficit vs. bandgap energy for a range of $Cu(InGa)Se_2$ and $Cu(InGa)(SeS)_2$ sample devices fabricated at IEC........ 24

FIG. 24 **(a)**The voltage deficit vs. Urbach energy for a wide range of $Cu(InGa)Se_2$, $CuIn(SeS)_2$ and $Cu(InGa)(SeS)_2$ sample devices fabricated at IEC **(b)** The voltage deficit modified to reflect differences in hole carrier densities........ 25

FIG. 25. TOF-SIMS image of the integrated Na signal across $CuGaSe_2$ samples indicating lateral variations in sample composition........ 27

FIG. 26 **(a)** Linear relationship between open circuit voltage and temperature, **(b)** Relationship between activation energy and open circuit voltage 28

FIG. 27. Drive level capacitance profiling and CV profiles at two temperatures for $CuGaSe_2$ sample s A2 and B3 30

FIG. 28. DLCP curves obtained for a 30% Ga CIGS sample device 33927 at 170K for a range of frequencies........ 32

FIG. 29. Copy of a screen plot from the modeling program showing an example of the types of spatial distribution of shallow and deep acceptors that can be selected...... 34

FIG. 30. Examples of calculated DLCP and CV profiles for the model electronic properties shown in Fig. 29 34

FIG. 31. Comparisons of simulated DLC profiles to actual experimental data of Fig. 28 for the measurement frequencies of 33kHz and 3.3kHz 35

FIG. 32. Experimental 33kHz CV profiles at 170K compared with two model calculations. 36

FIG. 33. Set of 1 MHz DLCP profiles and corresponding set of C-V profiles at 125K for one CIGS sample for increasing illumination times 38

FIG. 34. A 1:1 ratio is observed between increases in the deep trap densities and those of the hole free carrier densities in the bulk CIGS 39

FIG. 35. Comparisons of log(ΔN_{DL}) vs log(time) for different 780nm laser intensities 40

FIG. 36. The dependence of the metastable effect as a function of the 780nm intensity, after various exposure periods 40

FIG. 37. **(a)** Experimental I-V curves at 300K, taken under 780 nm illumination at 50mW/cm^2 after increasing periods of light soaking
(b) SCAPS simulation with deep acceptors as the dominant recombination centers
(c) SCAPS simulation of the compensated donor-acceptor conversion model 42

FIG. 38. Measured values of $J_{SC\text{-}IR}$ at 300K vs. the light soaking time compared to several fits assuming different values of the electron diffusion lengths 44

FIG. 39. Effects of changing absorber electronic properties on the cell fill-factor and open circuit voltage calculated using SCAPS 45

FIG. 40. Temperature-dependence of V_{OC} at 300 K under 980 nm for bifacial CIGS solar cell under both front-side illumination and back-side illumination 47

FIG. 41. Experimental I-V curves after 8 hours of light soaking, measured under 980nm monochromatic illumination from the front-side and the backside 48

FIG. 42. SCAPS simulations for front-side illumination at 980nm and SCAPS simulation using the same device parameters with backside illumination 48

FIG. 43. Capacitance vs. frequency (100Hz to 100MHz) of a CIGS solar cell obtained under 0V applied bias at 120K 49

FIG. 44. Equivalent circuit employed to deduce the dielectric relaxation time, and hence the resistivity, of the CIGS absorber within a solar cell device...................... 50

FIG. 45. High frequency capacitance and conductance data on CIGS sample 33456 at a temperature of 125K and two different values of applied bias 50

FIG. 46. Capacitance and conductance vs. frequency spectra at high frequencies for one CIGS sample at –1V bias fitted using the SCAPS modeling program 51

FIG. 47. **(a)**. High frequency admittance vs. frequency for the 27at.% Ga CIGS sample 33456 under 0V applied bias at several measurement temperatures
(b) 1MHz DLCP profiles vs. <*x*> for a similar range of temperatures. 53

FIG. 48. **(a)**. Set of 125K admittance data at 0V applied bias for a sequence of metastable states of a 32at.% Ga CIGS sample
(b) 1 MHz DLCP data for the same metastable states 54

FIG. 49. Hole mobilities for the sequence of metastable states as derived from the data in Fig. 47 55

LIST OF TABLES

TABLE I. Baseline CIGS devices obtained from the Institute of Energy Conversion....... 2

TABLE II. Sample devices with sulfur alloy absorbers provided by the Institute of Energy Conversion with their performance parameters 3

TABLE III. $CuGaSe_2$ sample devices provided by NREL with their performance parameters 5

TABLE IV. Electronic properties deduced for the two sulfur containing CISS sample devices 10

TABLE V. Summary of electronic properties for the 1.5eV bandgap CIGSS sample devices determined from DLCP and TPC measurements................................. 16

TABLE VI. Comparison of device parameters for a CIGSS pentenary sample device and a CISS sample device, both with the same S/Se ratios 19

TABLE VII. Summary of electronic properties for the CIGSS sample devices with sulfur fractions near 0.25 23

TABLE VIII. CGS based devices from both IEC and NREL 26

TABLE IX. Activation energy results from the IV analysis of the CGS devices................. 29

TABLE X. Baseline SCAPS parameters employed to model the JV_{IR} characteristics of the annealed state of our CIGS sample device 46

TABLE XI. SCAPS parameters for compensated donor-acceptor conversion model 46

TABLE XII. SCAPS Model Parameters used to obtain fits to high frequency admittance spectra.. 51

TABLE XIII. Summary of samples and the hole mobilities determined by high frequency admittance measurements 53

EXECUTIVE SUMMARY

Our research for the High Performance Program under NREL Subcontract No. XAT-4-33624-08 has focused on four major activities. The first has been to assist in the development of higher bandgap absorbers in the CIS alloy system that might lead to higher efficiency multijunction devices. Specifically, in collaboration with Bill Shafarman at the IEC, we have explored the suitability of absorbers with significant sulfur alloying as a possible route to wider gap, higher performance devices. Beginning with CISS quaternary samples without Ga, and then to the characterization of a set of CIGSS pentenary alloy devices with bandgaps slightly in excess of 1.5eV, it appeared that those with S/(Se+S) fractions near 30at.% gave the best performance. For example, a $Cu(In_{0.49}Ga_{0.51})(Se_{0.67}S_{0.33})_2$ sample exhibited an open circuit voltage in excess of 820mV and a 10.5% efficiency. Our characterization of the electronic properties generally indicated that the Urbach energies for the highest efficiency devices were generally significantly smaller than for the others. We also examined a set of CIGSS samples with roughly 25at.% S/(Se+S) ratios and varying Ga fractions and identified a sample with a bandgap of 1.37 eV that exhibited a V_{OC} of 776meV and a 14.6% efficiency, as well as a sample with a bandgap of 1.44eV, with a V_{OC} = 819mV and an efficiency of 13.0%. For the former case the absorber exhibited an Urbach energy of only 22meV, the lowest of any sulfur containing alloy.

Our photocapacitance spectra indicated that the dominant deep defect band of transitions was much broader in these CIGSS absorbers than in the CIGS absorbers and also lay closer to the conduction band compared to the higher bandgap CIGS devices. We found that electrons excited into this dominant deep defect band in the sulfur containing alloys would readily thermalize into the conduction band in contrast to the alloys containing no sulfur where we could not observe this. Thus the dominant defect band in the sulfur containing alloys was much less likely to behave as an efficient recombination center.

Regarding the higher bandgap alloys we also examined several CGS based devices from NREL, as well as a couple from IEC. Using our in-house TOF-SIMS facility and found a much greater non-uniformity in the Na spatial distributions in the IEC deposited CGS layers. This may partially account for the somewhat poorer performance of these samples compared to those fabricated at NREL and which, from our DLCP studies, exhibited much higher and more non-uniform densities of deep defects. In general the performance of all the 1.7eV bandgap CGS devices we examined were poorer than the best 1.52eV CIGSS devices primarily because of their smaller values of J_{SC} without the expected significantly better values of V_{OC}.

In the second area of focus, we made major progress in our ability to numerical simulate the results of admittance, DLCP, and CV profiling measurements on thin film chalcopyrite devices. These programs are specifically designed to incorporate much large spatial variations in the electronic properties across the absorber than have previously been examined. In particular, by examining DLCP and CV profiling data in which the bias voltage is varied well into forward bias, our simulations appear to able to extract significant information about defect states quite close to the barrier interface. Indeed, our preliminary evidence suggests that the deep defects very close to the barrier interface may be the most important for predicting device performance.

Third, we have advanced our understanding of light-induced metastable changes in CIGS and then used this to learn about how the deep acceptor defect band affects the performance of actual devices. Initially we examined the kinetics of these metastable changes in some detail and found that changes occurred under light exposure over very long periods of time with a sub-linear power law, and also a sub-linear power law intensity dependence. These results suggested a defect creation mechanism in which the initiating event involved the capture of two electrons into some initial precursor state (possibly the $(V_{Se}\text{-}V_{Cu})^+$ complex that has been proposed by Lany and Zunger). Because such metastable treatments could be used to modify the carrier density and deep acceptor density within a single device, we then examined the details of how CIGS cell performance was impacted by changing the density of the deep acceptors. Examining the corresponding changes in the IV curves, we always found a significant decrease in J_{SC} and

fill-factor, but with almost no accompanying change in V_{OC}. SCAPS modeling indicated that such a result could *not* come about if the deep acceptor was acting as the only major recombination center in this device. Instead, we could reproduce our observations quite well via a mechanism in which deep midgap (positive) donors were converted, via light soaking, into deep (neutral) acceptors (plus hole carriers). In such a scenario the observed changes in J_{SC} and fill-factor occurred simply because the depletion width became smaller as the deep acceptor and hole carrier densities were increased. These studies also allowed us to estimate the minority carrier diffusion length in a very direct manner.

The final (fourth) major accomplishment during our NREL Subcontract has been our development of high frequency admittance measurements to enable the determination of hole mobilities directly on working devices. This development required a lot of effort in the design of a new sample probe with an integrated current preamplifier and calibration capacitor so that we could be certain that we were measuring admittance accurately (up to nearly 100MHz). Our efforts proved successful, and we demonstrated that we could easily determine hole mobilities in the range 1 to 30 cm^2 V^{-1} s^{-1} in CIGS samples.

1.0 INTRODUCTION

This Report summarizes the completed activities carried out under NREL High Performance Subcontract XAT-4-33624-08. The main emphasis of our work has been to aid in the development and evaluation of higher bandgap absorbers in the CIS alloy system. The majority of that effort has been focused on exploring the suitability of absorbers with significant sulfur alloying in collaboration with Bill Shafarman's group at the Institute of Energy Conversion in Delaware. Three series of samples were examined; first, a series of quaternary $CuIn(SeS)_2$ based devices without Ga; second, a series of devices with pentenary $Cu(InGa)(SeS)_2$ absorbers in which the Se-to-S and In-to-Ga ratios were chosen to keep the bandgap nearly constant, near 1.52eV. Third, based upon the most promising samples in those 2 series, we examined a series of devices with pentenary $Cu(InGa)(SeS)_2$ absorbers with roughly 25at.% S/(Se+S) ratios and varying Ga fractions. In addition we also characterized the electronic properties of several wide bandgap $CuGaSe_2$ devices obtained both from IEC and NREL. The electronic properties of all thesse absorbers were examined using admittance spectroscopy, drive-level capacitance profiling (DLCP), transient photocapacitance, and transient photocurrent optical spectroscopies. The sample devices whose absorbers had Ga fraction below 40at.% and S fractions above 20at.% but below 40% were found to exhibit the best electronic properties, as well as the best device performance. The results on the sulfur alloys are presented in Section 4, and those on the $CuGaSe_2$ materials in Section 5.

In addition to our work directly examining the higher bandgap chalcopyrite alloys, we greatly expanded our numerical modeling capabilities to more fully extract information obtained by DLCP and related admittance based measurements. In Section 6 we apply this analysis to detailed DLCP and CV profiling data for one CIGS sample. We examine the profiles obtained using an extended range of DC biases so that we could address the influence of defects close to the barrier interface. We were thus able to extract detailed spatial profiles of both the shallow and deep acceptors, and also to infer the existence of a band of much deeper defects in the region closest to the barrier interface in this sample device.

In Section 7, we utilize light-induced metastable changes to try to understand the role of the deep acceptor defects on a CIGS sample device. Such light exposure can be used to increase the deep acceptor density (and also the hole carrier density) by more than a factor of 4. We correlated changes in the admittance data with the IV characteristics, and employed SCAPS modeling to simulate the experimental data. Our results indicate that, although the IV curves exhibit both a reduction in short-circuit current and fill-factor with light-soaking, the recombination rate within the depletion region actually remains nearly constant in spite of the significant increases in the deep acceptor density. A model was identified that appears to quite successfully account for these results. It involves the conversion, via light-soaking, of deep midgap donors into deep neutral acceptors (plus an equal number of hole carriers).

Finally, in Section 8, we describe the development of high frequency admittance measurements to enable the determination of hole mobilities directly within working devices. This ability, plus our numerical modeling activities mentioned above, have significantly added to our tool set for connecting the electronic properties, obtained through our junction capacitance based measurements, to the ultimate performance parameters of these CIS-based solar cells.

2.0 SAMPLES

2.1 INSTITUTE OF ENERGY CONVERSION SAMPLES

Most of the sample devices examined in this Subcontract were obtained from Bill Shafarman's group at the University of Delaware, Institute of Energy Conversion (IEC). Initially these included a set of $CuIn_{1-x}Ga_xSe_2$ (CIGS) baseline samples and a couple $CuInSe_{1-y}S_y$ (CISS) samples. During Phase II (late 2005) we received four $CuIn_{1-x}Ga_xSe_{1-y}S_y$ (CIGSS) pentenary samples from IEC, all with bandgaps close to 1.52 eV. In Phase III (2007) we received an additional set of five CIGSS pentenary samples, all with S:Se ratios near 1:3. A couple $CuGaSe_2$ (CGS) sample devices were obtained from IEC in 2006.

All of the IEC samples were in the form of finished solar cells. The absorbers for all of the above devices were about 2 μm thick and were deposited using three, four or five-source elemental evaporation [1,2,3]. They were deposited on soda-lime glass which had been coated with a 1 μm Mo layer. In one case, however, a companion CIGS sample was deposited onto a bare glass substrate to allow us to compare a conventional 4-probe resistivity measurement with our high frequency method that was carried out directly on a photovoltaic device (see Section 8 below). All of the absorber compositions, determined by energy dispersive x-ray spectroscopy, were slightly Cu poor (80% to 90% of stochiometric) except for the endpoint $CuInS_2$ devices,

TABLE I. Baseline CIGS devices obtained from IEC, in order from lowest to highest Ga content, together with their properties. These include the substrate temperature during growth (T_{SS}), the Ga content, and the optical gap (E_g). Also listed are the device performance characteristics: the efficiency, open circuit voltage (V_{oc}), short circuit current (J_{sc}) and the fill factor (FF). The two more recently IEC deposited CGS endpoint samples are also included.

Sample #	T_{ss} (ºC)	Ga/(In+Ga)	E_g (eV)	V_{oc} (V)	J_{sc} (mA/cm^2)	FF (%)	Eff (%)
33456	550	0.27	1.16	0.55	32.4	65.0	11.6
33934	550	0.30	1.18	0.63	31.5	76.7	15.2
33400	550	0.32	1.20	0.65	33.0	74.8	16.1
33233	480	0.32	1.19	0.61	32.3	72.2	14.3
33264	400	0.32	1.20	0.60	29.5	65.7	11.8
33927	550	0.32	1.20	0.63	31.3	75.4	15.1
33444	550	0.34	1.22	0.61	29.1	69.1	12.3
32988	550	0.46	1.29	0.72	29.1	72.5	15.2
33915	550	0.65	1.42	0.78	23.6	65.5	12.2
33875	550	0.80	1.53	0.74	20.4	63.9	9.6
33912	550	0.80	1.53	0.82	16.3	65.9	8.8
33999 (A1)	550	1.00	1.7	0.81	10.0	68.	5.6
34000 (A2)	550	1.00	1.7	0.84	10.2	60.3	5.1

which were copper rich. To form devices, a chemical bath deposition was used to deposit 30-40 nm of CdS, then sputtered ZnO/ZnO:Al or ZnO/ITO window layers were added to form the top contact, with evaporated Ni/Al grids. In the case of the $CuInS_2$ device, the CuS surface layer was etched off before finishing the device as above.

We continued to utilize many of the $CuIn_{1-x}Ga_xSe_2$ (CIGS) baseline samples we received during the previous five years. The first two entries in Table I list performance parameters for the CIGS samples employed for our DLCP modeling studies (Section 6) and most of the light-induced metastability studies (Section 7), respectively. The performance parameters of the two 1.7eV bandgap $CuGaSe_2$ (CGS) samples that were obtained from IEC in the Spring, 2006, are also included in this Table. These were employed for study at Linfield College and their properties were compared with NREL deposited CGS devices. The results for the electronic properties of the CGS samples will be given in Section 5.

The properties of the sulfur containing sample devices are listed in Table II. These fall into 3 groups: A set of quaternary CISS devices, a set of pentenary CIGSS devices in which the gallium and sulfur ratios were adjusted to keep the bandgap nearly constant near 1.5eV, and a set of CIGSS devices in which the sulfur/selenium ratio was kept nearly constant at roughly 1-to-3.

Table II. Sample devices with sulfur alloy absorbers provided by the Institute of Energy Conversion with their performance parameters. A couple of non-sulfur containing samples indicated by * are included in this Table for comparison purposes. Note that the second group comprises five pentenary CIGSS samples that all contain absorbers with very nearly the same 1.52 eV bandgaps.

Sample Series	Ga / (In+Ga)	S / (S+Se)	E_g (eV)	J_{SC} (mA/cm^2)	V_{OC} (V)	FF (%)	Eff (%)
*33469	0	0	1.0	34.2	0.42	67.5	9.62
24160	0	0.33	1.15	29.3	0.48	67.6	9.46
24208	0	0.54	1.3	25.8	0.51	54.9	7.27
24138	0	1.0	1.53	19.2	0.64	65.2	7.9
24147	0	1.0	1.53	21.2	0.65	59.9	8.28
*33912	0.8	0	1.53	16.3	0.82	65.9	8.8
24262	0.68	0.12	1.51	16.4	0.81	69.4	9.2
24188	0.51	0.33	1.52	18.5	0.83	68.1	10.5
24268	0.33	0.56	1.52	11.9	0.675	62.4	5.0
24442	0.29	0.24	1.32	79.3	0.73	24.9	15.0
24440	0.38	0.23	1.37	76.7	0.776	24.3	14.6
24439	0.48	0.23	1.44	71.9	0.819	21.6	13.0
24438	0.62	0.24	1.55	63.1	0.865	17.1	9.6
24295	1.0	0.26	1.88	53.6	0.994	6.1	3.3

FIG. 1. Diagram indicating the compositions of the $Cu(InGa)Se_2$, $CuIn(SeS)_2$, and $Cu(InGa)(SeS)_2$ sample devices provided by IEC. Note that, for the CIGSS samples, one set of alloys was chosen to keep the bandgap nearly constant (near 1.5eV), and another was chosen to have a nearly constant S/(S+Se) ratio (near 0.25).

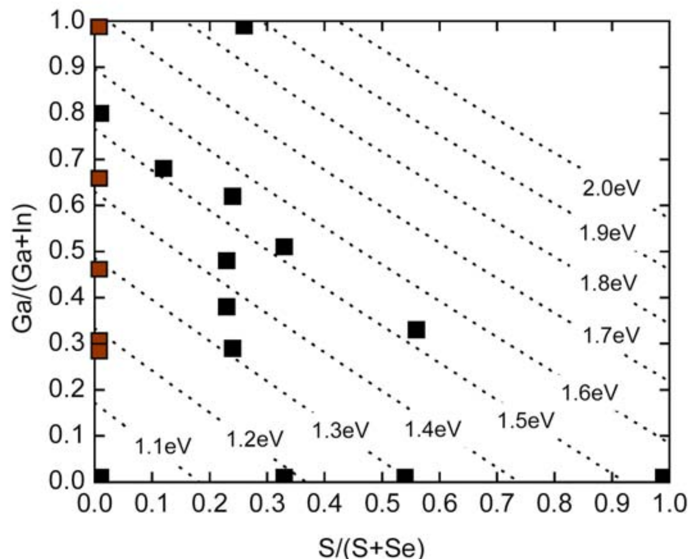

This final set was deposited because it appeared that sulfur fractions in this vicinity tended to yield higher efficiency CIGSS devices.

In addition to the above samples, a bifacial CIGS solar cell was successfully fabricated at IEC to enable a wider range of measurements to be employed in our investigation of the metastable changes in photovoltaic CIGS devices (Section 7). This samples employed a thin semi-transparent 40 nm thick layer of Mo (having a sheet resistance of 5 Ω/cm^2) on soda lime glass as their back contact. The absorber was a 2 μm thick CIGS layer with Ga a fraction near 30at.%, and the device was completed using chemical bath deposition of a CdS layer, a sputtered ZnO/ITO window and Ni/Al grids. The device performance of bifacial CIGS solar cells was almost the same as that of a co-deposited conventional thick Mo counterpart device, although the thin Mo versions showed a slightly larger series resistance and lower fill factor. The particular sample studied had a fairly good efficiency of 12.8% whereas the corresponding standard 700 nm thick Mo device had efficiency around 17%. Transmission vs. wavelength through the 40 nm Mo layer was measured for wavelengths between 780 nm and 980 nm and was determined to be about 4 %.

A diagram that nicely summarizes the compositions of all the IEC absorbers examined during the 3 years of this Subcontract is presented in Fig. 1.

2.2 NREL COPPER GALLIUM DISELENIDE DEVICES

Three additional CGS were obtained through David Young at NREL for study at Linfield College. These were deposited using their 3-stage growth process on Mo coated soda lime glass.[4] Following the deposition of the CGS absorber, devices were finished with a 50-60nm thick CdS deposited by chemical bath, and then an undoped ZnO layer and a doped ZnO:Al layer

Table III. $CuGaSe_2$ sample devices provided by NREL with their performance parameters.

Sample	J_{SC} (mA/cm^2)	V_{OC} (V)	FF (%)	Eff (%)
S2419 "B1"	8.7	0.697	57.0	3.5
S2258 "B2"	14.5	0.752	63.7	6.95
S2258 "B3"	13.85	0.734	61.1	6.2
S2258 "B4"	13.5	0.813	62.4	6.8
S2206 "B5"	14.97	0.795	65.9	7.83

were sputter-deposited. The performance parameters of the NREL CGS sample devices are listed in Table III.

3.0 EXPERIMENTAL CHARACTERIZATION METHODS

The measurements employed in our studies rely on a set of experimental techniques which have all been described previously in some detail. They consist of (1) admittance spectroscopy as a function of temperature and frequency, (2) drive-level capacitance profiling, and (3) transient photocapacitance taken together with transient junction photocurrent spectroscopy. Since we provided a description of each of these methods in our last Annual Report, we will only review each method very briefly and review what kind of information is obtained from each type of measurement.

3.1 ADMITTANCE SPECTROSCOPY

The most common method that has been employed to characterize the electronic properties of the absorber in CIS and related alloy devices is the measurement of junction capacitance as a function of frequency and temperature, known as admittance spectroscopy [5,6]. In an AC junction capacitance measurement on a diode sample, a small modulated voltage of frequency ω is applied to the reversed biased barrier, producing an AC distribution of thermally activated responding charge. Then, if ε and A are the dielectric constant and barrier cross-sectional area, respectively, the measured capacitance is

$$C = \frac{\varepsilon A}{\langle x \rangle} \qquad (1)$$

where $\langle x \rangle$ is the first moment of the responding AC charge distribution. The above relation is valid in general, even in cases where defect densities exceed shallow dopant densities, or when the distribution of states within the gap is quasi-continuous rather than consisting of a series of discrete levels.

It is most common to determine the junction capacitance as a function of frequency and temperature. This is known as admittance spectroscopy [7]. This technique can yield the activation energy of conduction, as well as the activation energy of any defect states having energetic positions that cross the quasi-Fermi energy within the band bending region. Between 1992 and 2000 this had been the primary method employed to disclose and characterize the deep defect states in CIS and the CIGS alloys. [8]

Generally, admittance spectroscopy measurements are sensitive to states with energies between that of the quasi-Fermi energy at the interface, and the activation energy of conduction. While the results from admittance spectroscopy can be distorted by spatially non-uniform densities of defects, measurements at a number of different dc biases can test whether such spatial non-uniformity is a concern. In addition, since response from interface states only occurs when their energetic position intersects that of the quasi-Fermi level near the interface, measurements at more than one dc bias can often distinguish whether a particular response arises from interface or bulk states. [9]

While admittance spectroscopy readily indicates the activation energy of the defect response, it is more difficult to obtain the absolute density of such states from this measurement since such estimates sometimes require prior knowledge of other material characteristics. This can particularly be a problem in cases where the defect density becomes comparable to the carrier density, due to the dependence of these estimates upon knowledge of the carrier density. This itself can be difficult to accurately determine in such cases. For this reason, we usually rely on the method of drive-level capacitance profiling (DLCP) which is described below.

3.2 DRIVE LEVEL CAPACITANCE PROFILING (DLCP)

In the drive-level capacitance profiling (DLCP) method [10,11], one makes use of the fact that the measured depletion capacitance depends on the amplitude of the applied bias' AC modulation δV (the "drive level"). Expanding capacitance in a power series of δV

$$C = C_o + C_1 \left(\delta V\right) + C_2 \left(\delta V\right)^2 + \ldots \tag{2}$$

one obtains the "drive level charge density" N_{DL}

$$N_{DL} = -\frac{{C_0}^3}{2q\varepsilon A^2 C_1} = p + \int_{E_{F0}}^{E_V + E_e} g(E,x)dE \tag{3}$$

In the integral E_{F0} is the Fermi energy position and p is the free carrier density in the undepleted film. The cutoff energy, E_e , depends on the frequency and temperature of measurement:

$$E_e(\omega,T) \quad = \quad k_B T \log(\nu/\omega) \tag{4}$$

That is, N_{DL} as determined by C_0 and C_1 is directly related to an integral over the density of states, $g(E,x)$. By altering the measurement temperature (or frequency) we obtain information about the energy distribution of the defects and, by altering the applied DC bias, we can vary the spatial region at which we detect the defects in the sample. That is, we can spatially profile the defects as a function of the position from the barrier interface.

In contrast to standard CV profiling, the DLCP profiles are generally insensitive to the response from states at or near the interface, except for specific values of dc bias which allow the interface states to dynamically respond to the alternating voltage. This last attribute can be particularly useful in distinguishing the interface from bulk response of defects. Thus, a detailed comparison between the standard C-V and DLCP profiles can often distinguish interface states from bulk defects in the semiconductor film.

3.3 TRANSIENT PHOTOCAPACITANCE AND PHOTOCURRENT SPECTROSCOPY

The transient photocapacitance and transient junction photocurrent spectroscopies are methods that yield optical spectra closely resembling sub-bandgap absorption spectra. They were developed for the study of amorphous silicon but have been shown to be very successful in recent years in the study of electronic properties of CIS and related materials. They have been described in detail elsewhere [12,13]. The principle and implementation of the photocapacitance method is similar to the more familiar DLTS technique. Briefly, the semiconductor junction held under reverse bias is subjected periodically to a voltage "filling pulse" which allows majority carriers to move into the previously depleted region and be captured. Following these pulses a capacitance transient can be observed as holes are thermally emitted out of the majority carrier traps and leave the depletion region. In the transient photocapacitance (TPC) measurement, however, one introduces sub-band-gap monochromatic light to induce optical transitions in addition to any thermal ones. Actually, light is applied after *every other* filling pulse so that the capacitance transients with and without light present can be subtracted. The difference, integrated over a time window and normalized to the photon flux, yields the photocapacitance signal at each photon energy selected by the monochromator. Repeating this over the full range of sub-band-gap photon energies available yields the *photocapacitance spectrum*.

The related method, transient photocurrent (TPI) spectroscopy, is identical except that one records the integrated current signal, with and without light present, instead of the capacitance signal. Whereas a TPC signal results from a change in depletion charge, and may thus be positive or negative depending upon whether there is a predominance of majority or minority carrier emission, respectively, the current signal will always have the same sign irrespective of which type of carrier is emitted.

A schematic illustrating the types of sub-bandgap optical transitions that might be observed is shown in Figure 2. A TPC signal might result from the different types of transitions shown. For example, a transition of type (a) in which an electron is excited into an empty gap state and

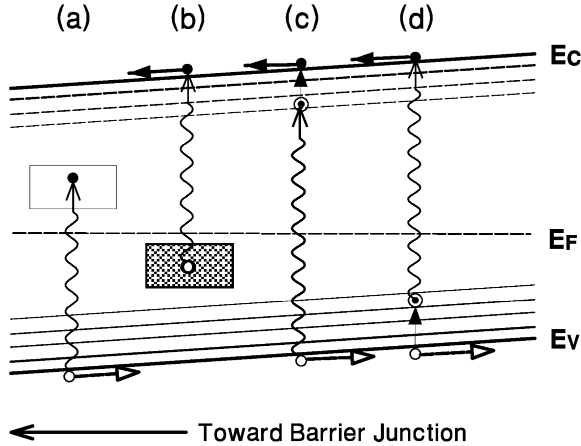

FIG. 2. Types of sub-bandgap optical transitions observed in semiconductors. Type (a) shows optical excitation between the valence band and an unoccupied gap state. Type (b) shows a transition in which an electron is removed from an occupied gap state to the conduction band. Type (c) shows a transition between the valence band and the unoccupied conduction bandtail, whereas type (d) shows transitions between the occupied valence bandtail and the conduction band.

the hole escapes increases the negative charge density of the depletion region and thus increases the junction capacitance. This results in a positive TPC signal. On the other hand, a transition of type (b) has the opposite effect, in that the electron is able to escape and the hole remains trapped, resulting in a negative TPC signal. Transitions of types (c) and (d) result in both carriers escaping from the depletion region, suggesting that there is no net charge change, and hence no TPC signal. However, if there is an asymmetry in the escape fraction of the two carrier types, a non-zero TPC signal is the result. In addition, transitions of types (c) and (d) will induce relatively large photocurrent signals due to the total charge motion. In general, if the sub-bandgap optical excitations result in p holes and n electrons, the TPC signal is proportional to $(p - n)$ whereas the TPI signal is proportional to $(p + n)$. Therefore by measuring both quantities we can obtain the rates of the holes and electrons excited out of the depletion region by the light. This ability to distinguish the type of carrier emission process taking place is unique among all the types of sub-band-gap spectroscopies used to study semiconducting materials.

4.0 RESULTS FOR THE SULFUR CONTAINING ALLOY SAMPLES

4.1 THE QUATERNARY COPPER INDIUM SELENIUM SULFUR (CISS) ALLOYS

The sub-band-gap spectra for the full series of four CISS alloys from IEC that we have examined (including x=1.0 and x=0.0 endpoint samples reported on last year [14]) are displayed in Fig. 3. We clearly see the increase of bandgap with increasing sulfur content. We can also see that the sharpness of the bandtail (characterized by the Urbach energy) is similar for all four samples.

Admittance spectra are displayed for the two mixed composition CISS samples in Fig. 4; specifically covering frequencies between a few hundred Hz to 100KHz and temperatures between 160K and 300K. For the 33at.% sulfur sample there is a small capacitance step with an activation energy of 0.31eV, probably reflecting a deep acceptor defect band. For the 54at.% sulfur sample a much larger capacitance step is exhibited. However, this corresponds to an

FIG. 3. TPC spectra for four CuIn(SeS)$_2$ samples. The variation of bandgap with sulfur content is clearly evident. Note the similar bandtail slopes (Urbach energies) for all 4 samples. The two mixed Se,S samples to be focused on in this Section are shown by the black and blue data symbols, with Urbach energies of 29meV and 25meV for the 33at.% and 54at.% sulfur fractions, respectively. These two samples also appear to have very low defect levels as indicated by the magnitude of the shoulders that appear below 1 eV.

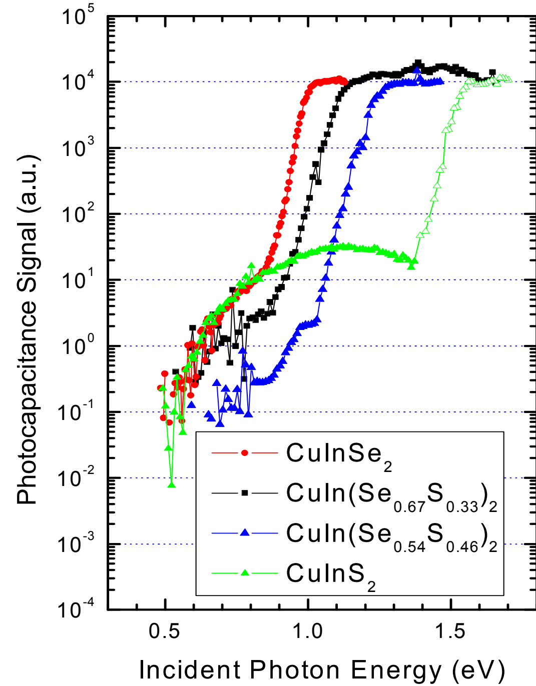

activation energy of roughly half the bandgap and so may merely indicate the threshold for thermal carrier generation across the gap, rather than the existence of a defect band within the gap.

Drive-level capacitance profiling (DLCP) was also carried out on these samples and the results are shown in Fig. 5. This measurement provides an estimate of both the free hole carrier density and the deep acceptor density. The profiles for the $CuIn(S_{0.33}Se_{0.67})_2$ sample obtained at

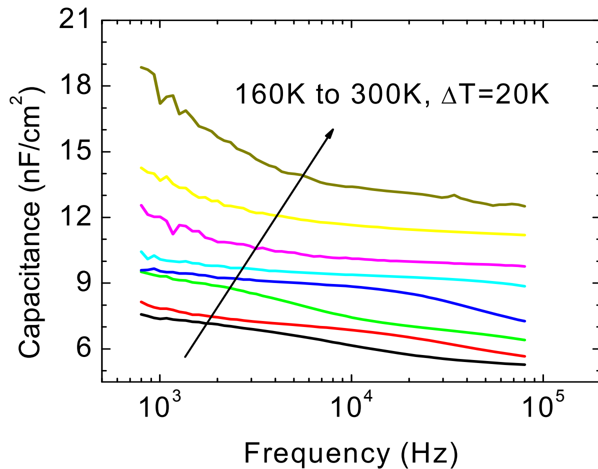

FIG. 4(a). Capacitance vs. frequency admittance spectra at zero bias over a range of temperatures for the 33at.% sulfur sample. The small capacitance step appearing in the lower temperature curves has an activation energy of 0.31eV, and probably corresponds to that of a deep acceptor band.

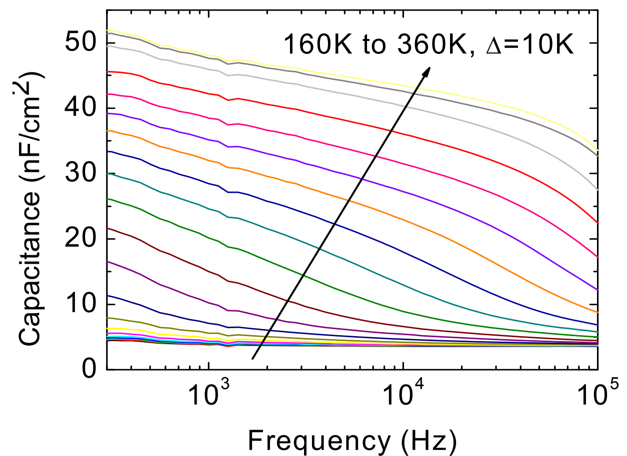

FIG. 4(b). Capacitance vs. frequency admittance spectra at zero bias over a range of temperatures for the 54at.% sulfur sample. The large capacitance step in this case has an activation energy of 0.63eV, roughly half the bandgap. This probably simply reflects thermal carrier generation across the gap.

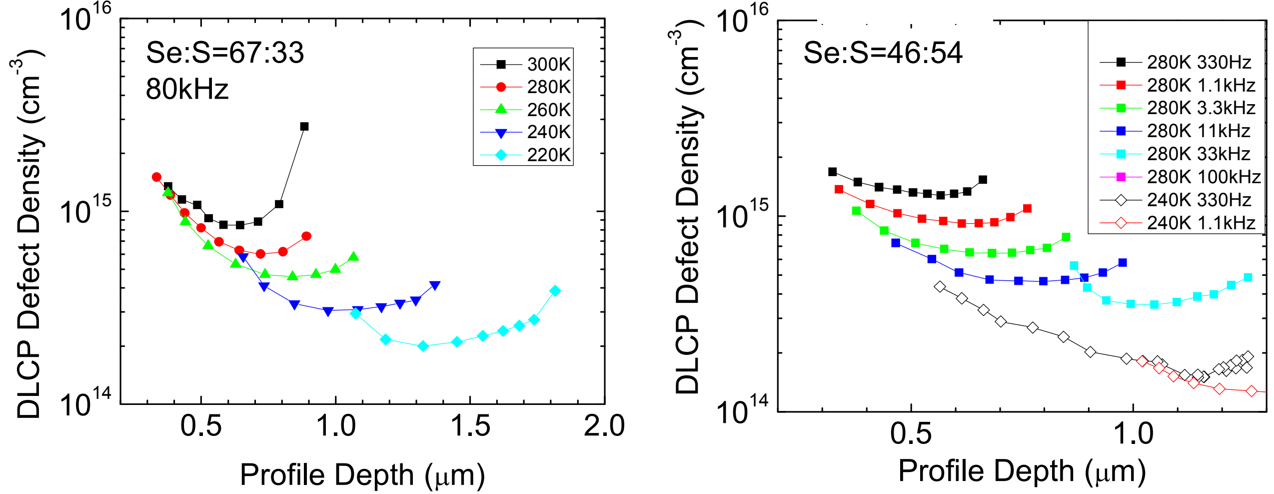

FIG. 5. Series of DLCP curves for the two mixed Se,S alloy samples. In both cases the free carrier densities, disclosed from the lowest temperature, highest frequency profile, are quite low: roughly 2 x 10^{14} cm^{-3} for each sample. The density in the deep acceptor defect band (given from the difference between the highest and lowest curves) is roughly 10^{15} cm^{-3} for both cases.

the lowest measurement temperature indicate a very low free hole density, about 2 x 10^{14}cm^{-3}. At the highest measurement temperature the profile indicates a nearly 10^{15} cm^{-3} value, indicating a deep acceptor density which is the difference, or roughly 8 x 10^{14} cm^{-3}. The results for the $CuIn(S_{0.54}Se_{0.46})_2$ sample are quite similar except that the free hole density exhibits a larger spatial variation, ranging from perhaps 5 x 10^{14} cm^{-3} close to the barrier junction to 2 x 10^{14} cm^{-3} at distances of 1 micron. The deep acceptor density in the 54at.% S sample appears quite similar to that of the 33at.% S sample.

The results obtained from these measurements for the two CISS quaternary samples are summarized in Table IV. The low carrier densities indicated in the DLCP measurements for these two samples contrasts with the values in excess of 10^{15} cm^{-3} found using DLCP on $Cu(In,Ga)Se_2$ samples fabricated at IEC of similar bandgap. For those samples the values of carrier and deep acceptor densities were nearly equal in most cases.[15] The lower carrier densities in these CISS devices are also undoubtedly partly responsible for the poorer performance compared to $Cu(In,Ga)Se_2$ devices of similar bandgap.

Table IV. Electronic properties deduced for the two sulfur containing CISS sample devices; specifically, the Urbach energy, E_U, determined from the TPC spectra, the activation energy of the capacitance step, E_σ, determined from the admittance spectra, and the hole carrier density, p, determined from the lowest temperature DLCP data. The deep acceptor density for both samples was slightly below 1 x 10^{15} cm^{-3} The device performance parameters are included for reference.

Sample Absorber	E_g (eV)	J_{SC} (mA/cm^2)	V_{OC} (V)	FF (%)	Eff (%)	E_U (meV)	E_σ (meV)	p (cm^{-3})
$CuIn(S_{0.33}Se_{0.67})_2$	1.15	29.3	0.48	67.6	9.46	29	310	2 x 10^{14}
$CuIn(S_{0.54}Se_{0.46})_2$	1.3	25.8	0.51	54.9	7.27	25	630	<5 x 10^{14}

4.2 PROPERTIES OF THE COPPER INDIUM DISULFIDE ENDPOINT

A very striking major difference among the TPC spectra displayed in Fig. 3 is the fact that the TPC signal in the bandtail regime of the $CuInS_2$ sample is *negative in sign*. This is indicated by the open symbols in that figure. All other TPC signals were positive in sign. The negative TPC bandtail signal implies that the minority photoexcited electron carriers actually escape more easily than the majority holes. In Figure 6 we display TPC spectra for the $CuInS_2$ sample at several temperatures. These data indicate that, while the negative bandtail signal appears at temperatures below about 250K, it becomes *positive* for temperatures of 280K and above. This implies that, at room temperature, the photoexcited holes will be more easily collected than the electrons. Moreover, the magnitude of the TPC signal in the bandtail region, while positive at 280K, is relatively small. This implies nearly equal collection efficiency for the electrons and holes, with the latter favored only slightly.

The TPC spectra in Fig. 6 also display a broad deep band centered at roughly 1.0eV that exhibits a significant temperature dependence. This, we believe, reflects the variation of the thermal emission rate of trapped holes from this broad defect band as a function of temperature. That is, while the filling pulse ensures that the majority of gap states are occupied with holes initially, our TPC spectrometer records the optical excitation of holes out of these states in a time window roughly 200ms later. During this time, τ, holes will have been thermally emitted to the valence band up to an energy $E_e = k_B T \log(\nu\tau)$ above the valence band edge, E_V, where ν is the exponential prefactor for thermal emission. Hence the TPC signal from these states will be absent. As the temperature increases so will E_e, implying that the low energy threshold for optical excitation will increase to higher optical energies. This is illustrated schematically in

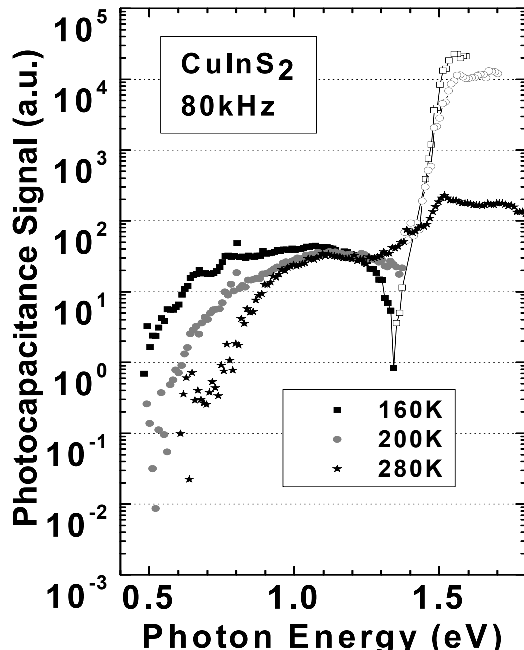

FIG. 6. Photocapacitance spectra of the $CuInS_2$ sample at different temperatures, aligned at 1.2eV. The open symbols denote a *negative* TPC signal. The broad extent of the defect band can be seen in the low temperature regime where thermal emission of the holes cannot take place within the time-window of the experiment. The 280K TPC signal in the high optical energy regime is positive, but significantly attenuated from a cancellation of the residual net charge due to nearly equal collection fractions of electrons and holes. The large but negative bandtail signals at lower temperatures indicates that most of the electrons can escape the depletion region within the time window of the experiment while many of the holes are being re-trapped.

FIG. 7. Schematic to explain the temperature dependence of the defect band for the $CuInS_2$ sample as it appears in the photocapacitance spectra of Fig. 6. As the measurement temperature increases, a larger fraction of the trapped holes in the defect band (up to an energy E_e above the top of the valence band) are able to escape during the 200ms delay before the beginning of the experimental time window. This means that the energy threshold for optical excitations between the defect band and the valence band will increase with increasing temperature. This is exactly what is observed in Fig. 6.

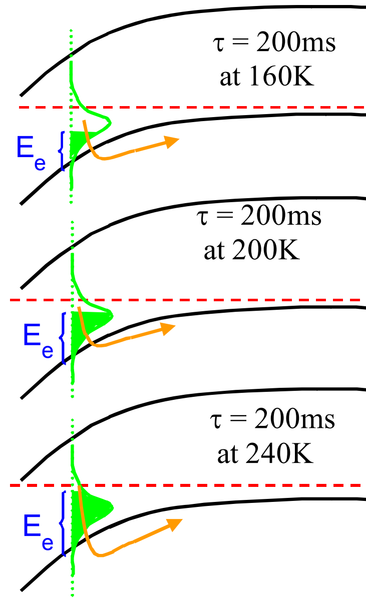

Fig. 7, and it accounts for what is observed in Fig. 6 in the energy regime below about 0.9eV. Ultimately, at high enough temperature, the TPC spectra only reveal the deep defect states that never lose their holes to the valence band via thermal emission. These are the states that lie above the quasi-Fermi level within the deep depletion region in steady-state.

It is important to note that the defect band revealed in the TPC spectra for the previous studied $Cu(InGa)Se_2$ alloys [13,17] did *not* exhibit this type of temperature variation. Rather, there appeared to be a distinct band of defects lying at an optical excitation energy roughly 0.8eV above E_V nearly independent of temperature. In Figure 8 we compare the 160K $CuInS_2$ TPC

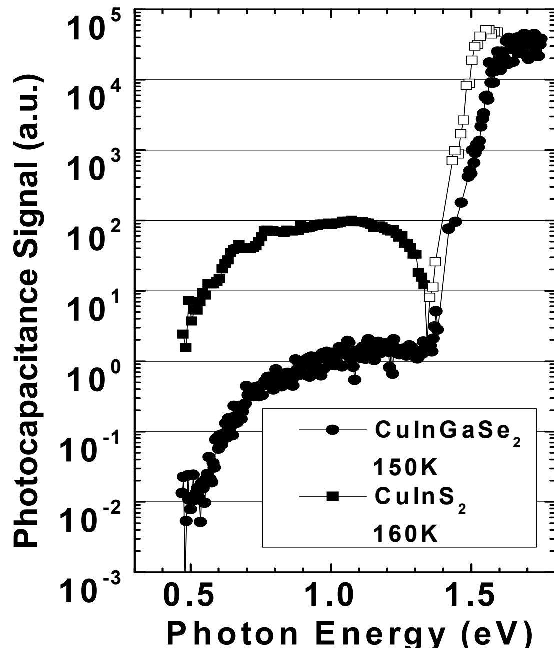

FIG. 8. Comparison of a 160K TPC spectrum of the $CuInS_2$ sample with a 150K $CuIn_{0.2}Ga_{0.8}Se_2$ alloy TPC spectrum obtained previously [13,17]. These two materials have nearly the same bandgap, but differ significantly in other respects: (1) The TPC signal in the bandtail region is negative for the sulfur sample, but positive for the $CuIn_{0.2}Ga_{0.8}Se_2$ alloy; (2) The defect band in the sulfur sample is roughly 100 times larger and exhibits a different energy distribution than that for the $CuIn_{0.2}Ga_{0.8}Se_2$ sample.

spectrum with the 150K TPC spectrum (taken previously [17]) of a $CuIn_{0.2}Ga_{0.8}Se_2$ sample with nearly the same energy gap. This indicates a different energy dependence of the distribution of states in the deep defect band which, for the $CuInS_2$ sample, appears to extend down to 0.6eV. This may indicate that the defect band is much broader in $CuInS_2$ than for the $Cu(InGa)Se_2$ alloys, or that the sulfur sample contains an additional defect band at lower energies in addition to that of the $Cu(InGa)Se_2$ alloys. The large magnitude of the defect band in the sulfide device correlates with its lower V_{OC}, although it is not clear that defect states within the absorber control the recombination as with the $CuInGaSe_2$ devices.

Finally, in Figure 9 we display both the TPC and TPI spectra for the $CuInS_2$ sample at 280K. We have aligned the spectra so that they overlap in the defect region. Because the current from either electrons or holes that escape the depletion region have the same sign, the TPI signal is always positive. Figure 9 indicates that in the bandtail region the TPI signal is approximately 250 times as large as the TPC signal. This implies a nearly equal probability for electrons and holes to escape so that the TPC signal is cancelled to within 1 part in 250 at 280K. In contrast, the magnitude of the negative TPC signal at lower temperatures in the bandtail region (see Fig. 14) is nearly the same as the TPI signal in Fig. 9. This implies that the minority current largely dominates the excitation of photogenerated electron-hole pairs in the lower temperature regime.

We believe that the negative TPC signal at lower temperatures occurs because there is a deep hole trap that significantly impedes the escape of the photogenerated holes from the depletion region at low temperatures, but is not a problem at higher temperatures because they are rapidly re-emitted. This may be related to the very large distribution of deep defect states also observed in this sample. It is presently unclear whether some of the unique properties of the $CuInS_2$ sample arise from the fact that it alone was deposited copper-rich instead of copper-poor.

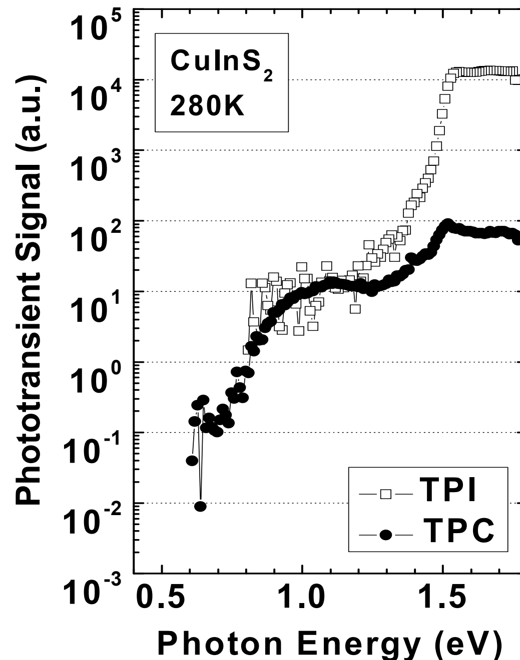

FIG. 9. Matched photocapacitance and photocurrent spectra on the $CuInS_2$ sample at 280K. The current signal is much larger than the capacitance signal due to the large numbers of both electron and hole carriers that are collected. While this cancels the charge change within the depletion region, and hence the TPC signal, it enhances the TPI signal.

Indeed, the electronic properties of the $CuIn(S_{0.33}Se_{0.67})_2$ sample seem much more similar to the previously studied $Cu(InGa)Se_2$ alloys. Further studies over a much wider range of the sulfur containing CIS materials are clearly required to obtain a better understanding of these issues.

4.3 PROPERTIES OF CIGSS PENTENARY SAMPLES WITH BANDGAPS NEAR 1.5 eV

4.3.1 General Electronic Properties

Three CIGSS pentenary sample devices with bandgaps near 1.52eV were received from IEC in December, 2005. Taken together with the endpoint $CuInS_2$ device and also the 80% Ga CIGS device received a few years ago, this provided a set of five samples whose Ga and S fractions were varied in tandem to produce nearly identical bandgaps. This set of devices was initially characterized using admittance spectroscopy. Capacitance and conductance phases of the complex admittance were monitored in the dark as a function of frequency and temperature. The resulting data was normalized to the sample area and are displayed in Fig. 10. The rollover frequencies of the step-like features are plotted in an Ahrennius plot, to obtain the activation energy of that feature. In this manner activation energies of 4 of the 5 samples were determined and are indicated in each figure. The 33% S sample exhibited a double-step, with activation energies of 323meV and 164meV. (We note that the second energy is approximately half the first.) Inspection of the activation energies shows a clear trend with sulfur content for the Cu-poor samples, agreeing with previous results [16] that showed activation energies increased with the bandgap for Cu-poor samples.

Representative DLCP results for the 12% S sample are shown in Figure 11. These data were

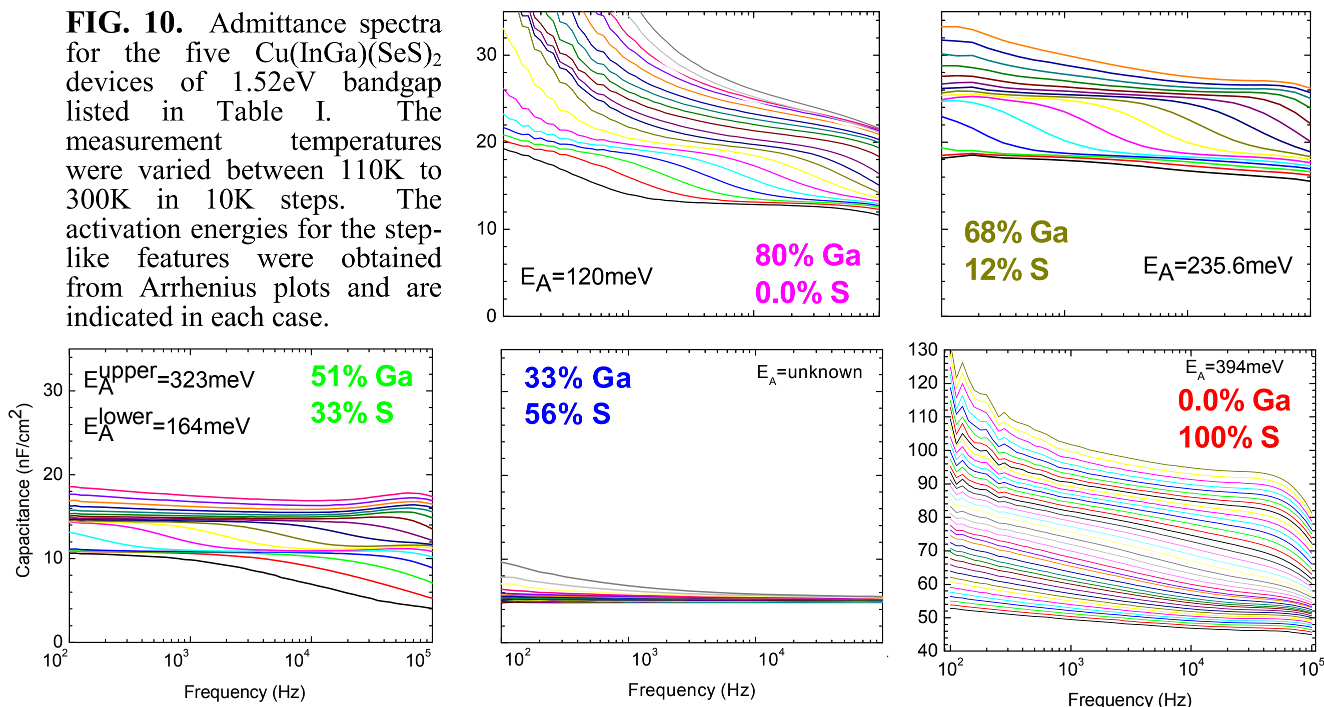

FIG. 10. Admittance spectra for the five $Cu(InGa)(SeS)_2$ devices of 1.52eV bandgap listed in Table I. The measurement temperatures were varied between 110K to 300K in 10K steps. The activation energies for the step-like features were obtained from Arrhenius plots and are indicated in each case.

FIG. 11. DLCP profiles at 170K for the $Cu(InGa)(SeS)_2$ sample with 12at.% S. The profiles are nonuniform throughout the active area of the sample, and reflect the activation of the deep acceptor as the energy scale of the measurement is changed.

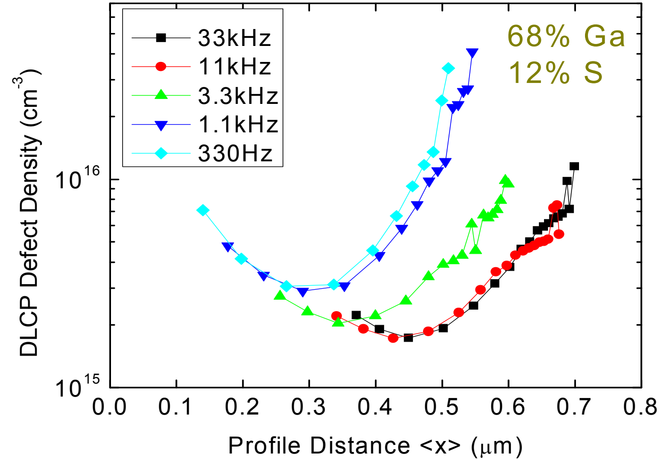

collected at 170K, at a series of frequencies chosen to profile the upper and lower portions of a step measured in admittance. Activation of a defect response can clearly be seen as the measurement frequency moves through the admittance step. Defect densities measured at high frequencies and low temperatures, corresponding to the bottom of the admittance step, are interpreted as free carrier densities. Low frequency and high temperature values correspond to the sum of the defect and free carrier densities. Thus, for the 12% S sample, as shown in Figure 11, we infer a free carrier density of 2×10^{15} cm^{-3} and a defect density of 2×10^{15} cm^{-3}. Similar results were obtained for the other samples, and this information has been included in Table IV.

The two samples with the highest sulfur content displayed unusual behavior. The 56% S sample revealed free carrier densities that were nearly intrinsic, and no observable defect response. On the other hand, the 100% sulfur *Cu-rich* sample showed very large defect densities, $>10^{17}$ cm^{-3}. Optical spectra for this sample, reported in detail in Section 4.2 above also indicated large defect densities [14]. Our data would seem to thus preclude these two alloy materials from consideration for high performance solar cells until their electronic properties can be significantly modified.

FIG. 12. Photocapacitance spectra collected near 180K for the four *Cu-poor* $Cu(InGa)(SeS)_2$ samples. These spectra have been aligned in the reime above 1.6eV. Included are two Gaussian defect bands used to fit the 0% and 51% sulfur samples. These defect bands are centered at 1.1 eV and 0.8 eV respectively. An average bandgap energy of 1.52 eV has been marked with a red vertical line.

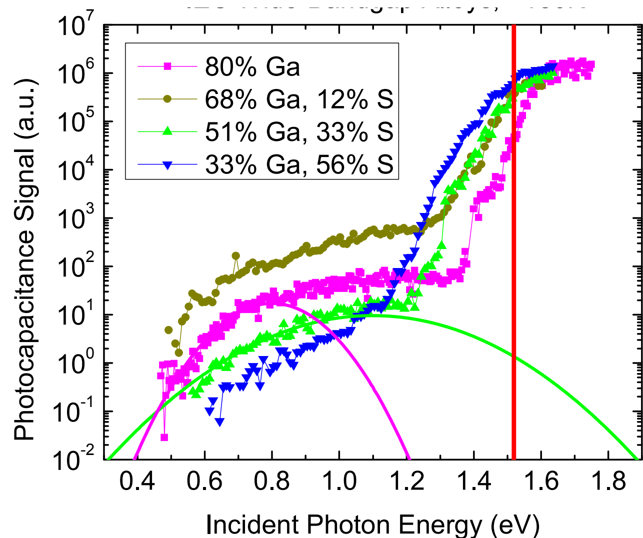

Table V. Summary of electronic properties for the 1.5eV bandgap CIGSS sample devices determined from DLCP and TPC measurements. DLCP was used to estimate densities of the deep acceptor (N_{DA}) and hole carrier densities. The TPC optical spectra yielded the Urbach energies (E_U) the position of the defect band, E_D, relative to the valence band, as well as 2σ, the FWHM of the defect bands. Some of the cell performance parameters are given for reference.

$\frac{Ga}{(In+Ga)}$	$\frac{S}{(Se+S)}$	V_{OC} (mV)	Eff (%)	N_{DA} (cm^{-3})	p (cm^{-3})	E_U (meV)	E_D (eV)	2σ (eV)
0.33	0.56	675	5.0	---	7×10^{13}- 2×10^{14}	35	1.16	0.16
0.51	0.33	829	10.5	7×10^{14}	4×10^{14}	26	1.05	0.15
0.68	0.12	809	9.2	2×10^{15}	1×10^{15}	33	1.0	0.16
0.8	0	820	8.8	1×10^{15}	4×10^{14}	26	0.80	0.08

We measured transient photocapacitance (TPC) spectra for all samples at a variety of temperatures, using ac-frequencies and pulse heights chosen to be in a flat region of the admittance and defect profiles of the samples. Spectra near 180K for the four *Cu-poor* samples are displayed in Figure 12.

Such TPC spectra are typically fit with the integrated sum of a Gaussian defect band and an exponential Urbach tail. Previous TPC measurements on a series of $CuIn_{1-x}Ga_xSe_2$ [17] samples reported a Gaussian defect centered at 0.8 eV, independent of Ga content. Fits to the TPC data collected for our series of pentenary samples also included a Gaussian defect band and exponential bandtail. However, we found that the energy position of the Gaussian defect band moved progressively to higher energies with increasing sulfur content. In addition, the widths of the defect bands were much broader than those found in CIGS. A summary of the parameters used to fit the TPC spectra in Figure 12 is given in Table V.

The 56% S sample exhibited the largest Urbach energy of the group, near 35 meV. This indicates that the minority carrier collection should be relatively poor for this sample compared to the others in the series. In addition, from DLCP and admittance measurements we determined an extremely low hole carrier density for this sample (Table V). It is perhaps then not surprising that this sample also exhibits a relatively poor overall efficiency compared to the others.

4.3.2 Temperature Dependence of Sub-Band-Gap Spectra

Typically we have observed very little temperature dependence for the TPC and TPI spectra of CIGS samples. This may be because the energy depth of the defect is simply too deep for thermal transitions to play much of a role the timescales of our measurements. However, in the all of the CIGSS alloys, as illustrated for two samples in Fig. 13, we do observe a significant change in the defect response at lower temperatures; notably, an *increase* in the TPC signal in the defect region and a dramatic reduction of the TPI signal in this region.

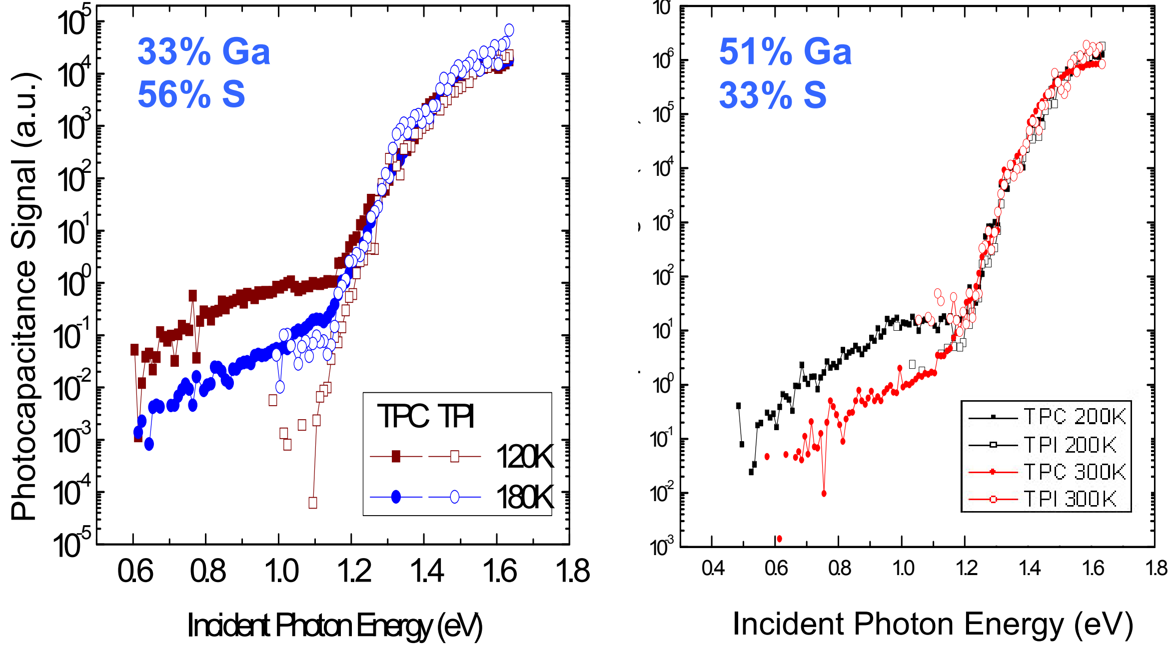

FIG. 13. Comparison of TPC and TPI spectra at two measurement temperatures for (a) the 33% Ga, 56% S sample and (b) the 51% Ga, 33% S pentenary sample. Note that the TPC signal in the defect band region (the shoulder below 1.1eV) is larger at lower temperatures for both samples. This indicates that the electrons optically excited into this defect from the valence band do not escape into the conduction band during the 0.5s timescale of the TPC measurement at lower temperatures, but do mostly escape into the conduction band at higher temperatures.

To account for this unusual behavior we have proposed a simple model for the transitions involving the deep defect seen in these optical spectra for this sample. We consider that the defect can be filled optically from the valence band and emptied thermally into the conduction band. A schematic of this is shown in Figure 14. For competing optical and thermal transitions of this nature, we can then show that the magnitude of the TPC signal in the defect band region will be given by:[18]

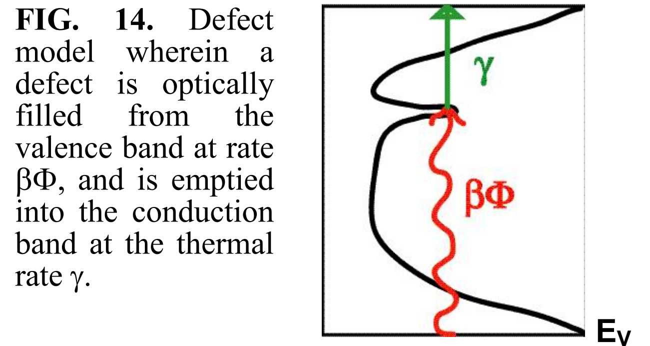

FIG. 14. Defect model wherein a defect is optically filled from the valence band at rate βΦ, and is emptied into the conduction band at the thermal rate γ.

$$S_{TPC} \propto \left(t_e \frac{\beta\gamma}{\beta\Phi + \gamma}(1-\xi_e) + \frac{\beta}{\beta\Phi + \gamma} \right) N_D \tag{5}$$

where β represents the optical cross section for transitions from the valence band, Φ is the optical flux, γ is the thermal emission rate into the conduction band, ξ_e represents the collection fraction of the conduction band electrons compared to valence band holes, N_D is the density of the defect, and t_e is a parameter representing the time scale of the measurement. At high temperatures when

FIG. 15. Detailed temperature dependence of the *ratio* between the TPC signal in the defect band region (below 1.1eV) to its value near the bandgap energy (1.52 eV) for the three pentenary samples. The relative defect signal decreases by more than an order of magnitude as the temperature is raised in all cases. The crossover temperature indicates where the thermal emission time, $(1/\nu)\exp(\Delta E/k_BT)$, of the defect electron into the conduction band is comparable to the measurement timescale (roughly 0.5s).

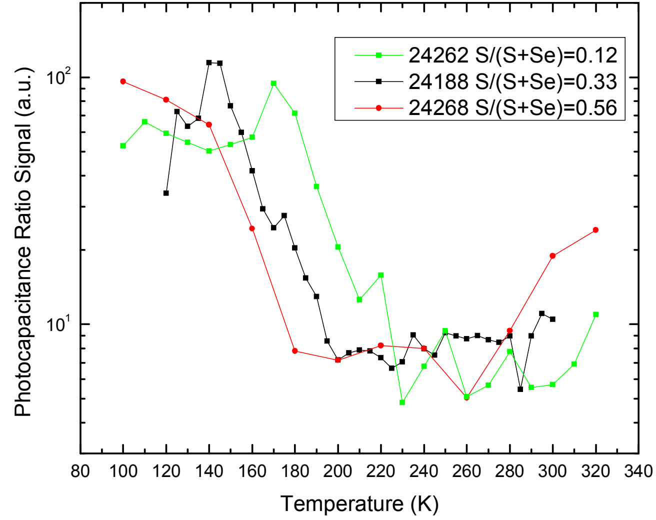

γ is large the first term in the parentheses will dominate, and the TPC defect signal will be relatively small since it will be reduced by relative degree of minority carrier collection, ξ_e . In contrast, at lower temperatures the second term in the paratheses will dominate, and the TPC defect signal will become relatively larger. That is, the TPC signal in the defect band region of the spectrum will be larger if electrons photo-excited into it from the valence band remain there for the timescale of our transient measurement (roughly 0.5s), but smaller if a substantial fraction of the electrons are subsequently excited into the conduction band and so leave the depletion region. This subsequent re-emission will occur on a timescale of $\gamma^{-1} = (1/\nu)\exp(\Delta E/k_BT)$, where ΔE is the thermal energy threshold between the defect level and the conduction band and ν is its thermal emission prefactor.

By changing the measurement temperature we can vary this thermal emission timescale through the 0.5s timescale of our TPC measurement. In Fig. 15 we have plotted the ratio of the TPC signal in the defect region (near 1.0eV) to that close to the bandgap (near 1.5eV) as a function of temperature for all three CIGSS samples. As illustrated in Fig. 16, the crossover temperatures decrease with increasing sulfur content, presumably because the conduction band-edge moves to lower energy relative to the defect band as we increase the sulfur fraction (and decrease the gallium fraction). Moreover, by assuming a quite reasonable thermal prefactor of 10^{12} sec^{-1}, the thermal energies deduced by the step temperature in Fig. 15, plus the optical thresholds of electron excitation into the defect band, sum to the known 1.52eV energy gaps.

If this analysis is correct it implies that the dominant defect band in these CIGSS materials does indeed move closer to the conduction band edge with S alloying, implying that it is less likely to be as effective as a recombination center. This could be an important factor in obtaining higher gap, higher performance chalcopyrite alloys.

Unfortunately, we have also found a counterexample to the simple interpretation illustrated in Fig. 16. Specifically, we compared the temperature dependence of the deep defect band in the TPC spectra for the pentenary CIGSS samples with the quaternary CISS samples of similar S/Se

FIG. 16. Band alignment of the three $Cu(InGa)(SeS)_2$ samples based upon theoretical studies of Wei and Zunger [19]. The positions of the deep defect feature have been inserted by their deduced optical transition energies relative to the valence band (the widths are not shown to scale). If we assume a reasonable value for the thermal emission prefactor, then the thermal energies to the conduction band deduced from Fig. 15, plus the optical transition energies for electron insertion from the valence band, roughly add to give the 1.5eV bandgap. The lower dashed lines indicate the activation energies of the deep acceptor features obtained from admittance measurements.

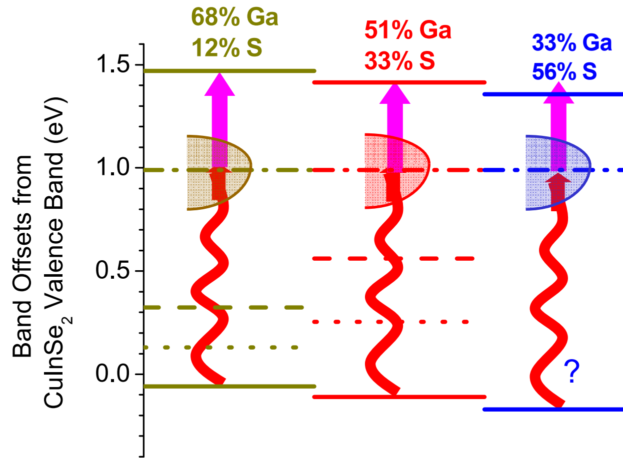

ratios. Because the quaternaries for a given sulfur fraction contain no gallium, they have significantly smaller bandgaps. A comparison of the device performance parameters for the CIGSS and CISS samples having 33at.% sulfur are re-listed in Table VI. It is worth noting that, among the set of three CIGSS and three CISS sample devices provided to us by IEC, the 33at.% sulfur absorber gave the best overall performance in both cases.

The TPC spectra for the CISS quaternary samples were also found to exhibit a marked temperature dependence in the ratio of the defect signal to the band-edge signal. In Fig. 17 we compare the temperature dependence of the defect band to band edge TPC signals for the 33at.% sulfur pentenary and quaternary samples. We see that the crossover temperature appears nearly identical for both. Much the same result was found for a pentenary and quaternary sample having roughly 55at.% sulfur.

This result is quite surprising given the very different bandgaps of the CIGSS and CISS absorbers and the fact that one would also expect a different relative energy position of the conduction band edge to defect bands in the gap. This result may imply that the exchange of electrons between the dominant defect band and the conduction band is actually tied to the S/Se ratio much more directly.

Table VI. Comparison of device parameters for a CIGSS pentenary sample device and a CISS sample device, both with the same S/Se ratios. The Urbach energies obtained from our TPC spectra are also included.

$\frac{Ga}{(In+Ga)}$	$\frac{S}{(Se+S)}$	Bandgap (eV)	E_U (meV)	V_{OC} (mV)	J_{SC} (mA/cm^2)	FF (%)	Eff (%)
0.51	0.33	1.52	26	829	18.5	68.1	10.5
0	0.33	1.15	28	480	29.3	67.6	9.46

FIG. 17. Detailed temperature dependence of the *ratio* between the TPC signal in the defect band region (below 1.1eV) to its value near the bandgap energy for the 33at.% sulfur pentenary and quaternary samples. The relative defect signal decreases by more than an order of magnitude as the temperature is raised in all cases. The crossover temperature indicates where the thermal emission time, $(1/\nu)\exp(\Delta E/k_B T)$, of the defect electron into the conduction band is comparable to the measurement timescale (roughly 0.5s).

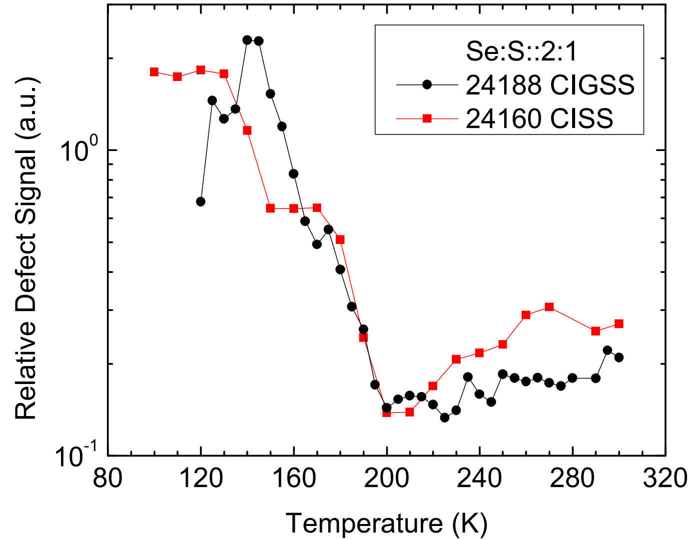

4.4 CIGSS PENTENARY SAMPLES WITH A CONSTANT S:Se = 1:3 RATIO

After examining the previous two series of CISS and CIGSS samples, we noted that the devices in which sulfur was substituted for Se at roughly the 30% level seemed to have the highest efficiencies in each group. We therefore decided to undertake an investigation of a final set of pentenary CIGSSe devices with a constant sulfur ratio near S/VI≈0.25. The list of samples we studied in this group are included in Table II of Section 2. There we can see that the efficiencies of most of these devices are very good: in particular, the devices with Ga/III ratios of 0.48, 0.38, and 0.29 had efficiencies of 13%, 14.6%, and 15%, respectively. While these efficiencies certainly aren't as high as world record CIGS devices, they are quite respectable for wider bandgap devices.

Results from admittance measurements on all five devices are summarized in Figure 18. All five devices showed activated behavior, in some cases more than one capacitance step. Activation energies seemed to come in both shallow and deep regimes, with deep activation energies ranging between 196meV to 328meV, and shallow activation energies from 40meV to 80meV. None of the devices showed evidence of a geometric capacitance limit, indicating that the carrier densities are high enough for the sample to not be fully depleted even at our lowest measurement temperatures.

DLCP and CV profiling measurements for two of these devices are displayed in Figs. 19 and 20. Figure 19 shows the results for the CGSS sample and indicates that the absorber thickness lies near 1.7μm, and that it has a free carrier density near 4×10^{14} cm^{-3}. As the temperature of the measurement is increased, the DLCP densities increases to reach a value near that given by by the CV profiles. We thus infer a deep defect density of 2×10^{15} cm^{-3} for the absorber in this device.

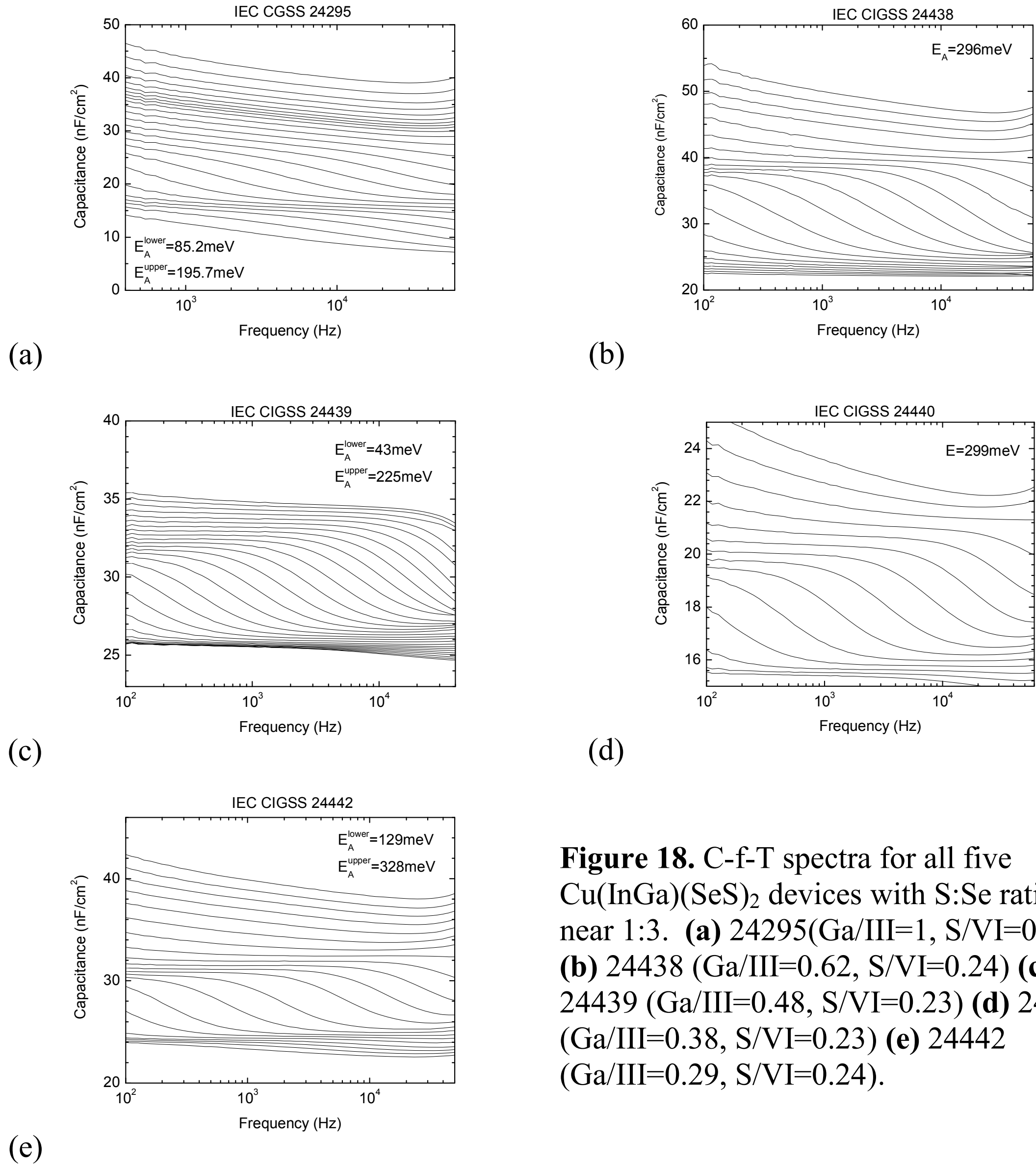

Figure 18. C-f-T spectra for all five $Cu(InGa)(SeS)_2$ devices with S:Se ratios near 1:3. **(a)** 24295(Ga/III=1, S/VI=0.26) **(b)** 24438 (Ga/III=0.62, S/VI=0.24) **(c)** 24439 (Ga/III=0.48, S/VI=0.23) **(d)** 24440 (Ga/III=0.38, S/VI=0.23) **(e)** 24442 (Ga/III=0.29, S/VI=0.24).

Figure 20 shows the DLC and CV profiles for the $Cu(InGa)(SeS)_2$ device with 38at.% Ga 24440. These appear very non-uniform. DLCP densities reach quite values above 10^{16} cm^{-3} for profile depths of 0.6 microns, and the CV densities are quite comparable in this region. For the carrier collection region closer than 0.5 microns we can only estimate a lower limit on the deep acceptor density of perhaps 5×10^{15} cm^{-3}. The results from electrical measurements on all 5 of these devices are summarized in Table VII.

In Fig. 21 the TPC spectra taken at 180K are shown for all five devices. Most notable are the variations in bandgaps with gallium alloying, particularly for high gallium contents, and the striking similarity in the defect structure. This similarity is reminiscent of the defect structure seen in $Cu(In_xGa_{1-x})Se_2$ alloys [3]. However, a Gaussian fit to this defect required an energetic depth of 1.6eV for the defect! This is larger than the bandgap of most of the devices, and so

Figure 19. DLC and CV profiles for IEC CGSSe device 24295 (Ga/III=1, S/VI=0.26) at 30kHz. Voltages ranged from -1.6V to 0.8V in steps of 0.1V. DLCP densities are in solid symbols, and CV densities in open symbols.

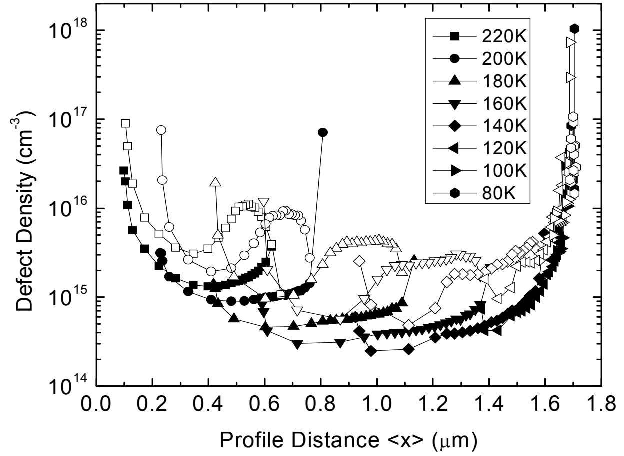

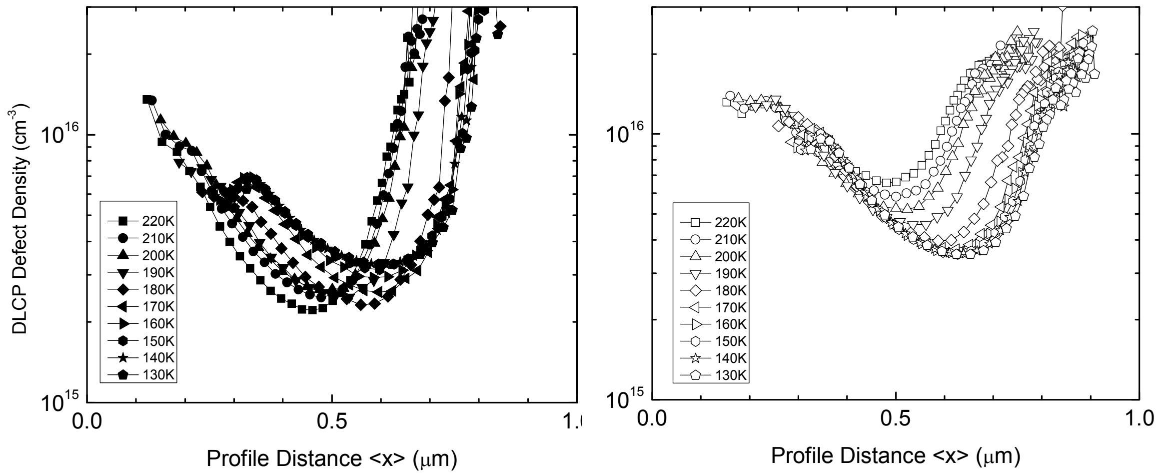

Figure 20. **(a)** DLC profiles for IEC CIGSSe device 24440 (Ga/III=0.38, S/VI=0.23) taken at 3.3kHz over a voltage range from -3.8V to 0.8V in 0.1V steps. **(b)** Simultaneously collected CV profiles.

likely does not provide a good indication of the energy of this defect relative to the valence band. Given that this defect band appears so broad, it is quite likely the signal in this regime is simply reflecting the convolution of the density of states at the edge of the valence band with a distribution of gap states that varies weakly with energy.

Also of note in Fig. 21 is the "lean over" of the bandtails in the two devices with the least gallium content. The TPI spectra did not show this type of behavior; instead, the bandtail continued to rise exponentially up to the bandgap. This suggests that there may be some additional cancellation due to a higher fraction of electrons being collected in this energy regime to thus further diminish the TPC signal.

4.5 CIGSS ALLOYS: ELECTRONIC PROPERTIES vs. CELL PERFORMANCE

A wealth of experimental data has been presented in Sections 4.1-4.4 to try to elucidate the electronic properties of the CISS and CIGSS alloys. However, the apparent lack of simple trends

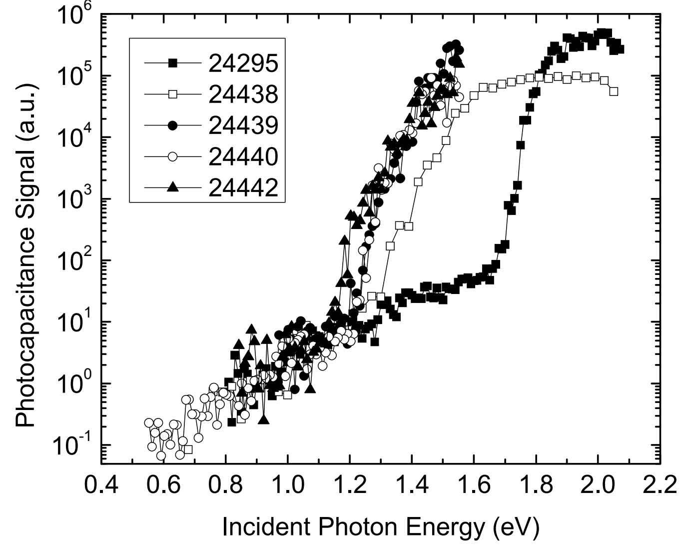

Figure 21. TPC spectra at 180K for the five constant chalcogen ratio pentenary devices.

in these data make it difficult to assess the potential success of utilizing sulfur alloying to obtain better high-gap materials and devices. We were able to deduce that S/(Se+S) ratios near 0.3 seemed to yield the best performance for materials with bandgaps above 1.4eV. A possible reason for this was also suggested; namely that, in contrast to samples without S, electrons were much more likely to be re-emitted once they became deep trapped into the dominant defect band. This meant that the deep defect was less likely to be involved in carrier recombination.

Figure 22(a) summarizes the performance for the range of device samples studied in perhaps the simplest way. That is, we can simply plot the efficiency vs. composition using axes that reflect both the gallium and sulfur fractions. Here it is clear to see that the poorest devices are those with either too much gallium or with too much sulfur. In Fig. 22(b) we display the same type of plot for one of the key electronic properties determined by our measurements; namely,

Table VII. Summary of electronic properties for the CIGSS sample devices with sulfur fractions near 0.25 as determined from Admittance, DLCP, and TPC measurements. DLCP was used to estimate densities of the deep acceptor (N_{DA}) and hole carrier densities, p. The activation energies of features deduced from admittance, EA, are listed along with the order of magnitude, x, of the corresponding thermal emission prefactor. The TPC optical spectra yielded the Urbach energies (E_U). A couple cell performance parameters are given for reference.

$\frac{Ga}{(In+Ga)}$	$\frac{S}{(Se+S)}$	E_g (eV)	V_{OC} (mV)	Eff (%)	N_{DA} (cm^{-3})	p (cm^{-3})	E_A (meV)	Prefactor exponent (s^{-1})	E_U (meV)
0.29	0.24	1.32	730	15.0	2 x 10^{15}	8 x 10^{15}	82.5 195.7	10^{10} 10^{9}	26
0.38	0.23	1.37	776	14.6	>5 x 10^{15}	2 x 10^{15}	296	10^{11}	22
0.48	0.23	1.44	819	13.0	1 x 10^{16}	8 x 10^{15}	43 225	10^{7} 10^{11}	30
0.62	0.24	1.55	865	9.6	1 x 10^{16}	6 x 10^{15}	299	10^{12}	38
1.0	0.26	1.88	994	3.3	2 x 10^{15}	4 x 10^{14}	129 328	10^{9} 10^{13}	18

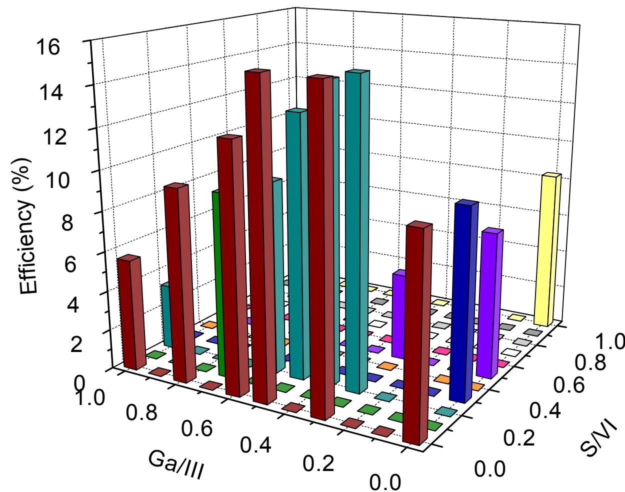

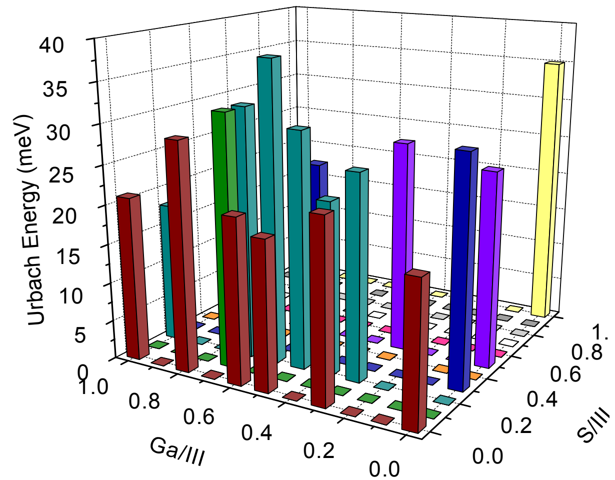

FIG. 22(a). Cell efficiencies for a wide range of $Cu(InGa)Se_2$, $CuIn(SeS)_2$ and $Cu(InGa)(SeS)_2$ sample devices fabricated at IEC. The samples moderate Ga factions with no sulfur, or with sulfur fractions near 0.3, seem to exhibit the best performance.

FIG. 22(b). Urbach energies determined from TPC measurements for this same set of samples. For the sulfur containing alloys, lower Urbach energies tend to be correlated with higher device performance.

the width of the bandtail, or Urbach energy. In some cases it would appear that the samples with the lowest Urbach energies lead to the best performance, but there seem to be exceptions to this.

In Fig. 23 we have plotted the "voltage deficit" vs. bandgap for the gallium containing alloys. The voltage deficit is defined simply as the difference between the bandgap energy (expressed in volts) and V_{OC}. Here we see some evidence that the samples with moderate sulfur ratios may actually lead to higher realized values of the cell voltage. To try gain some added understanding of this improvement we plotted in in Fig. 24(a) the voltage deficit vs. E_U. Here we see that many of devices with the lowest voltage deficits lie between the two solid lines.

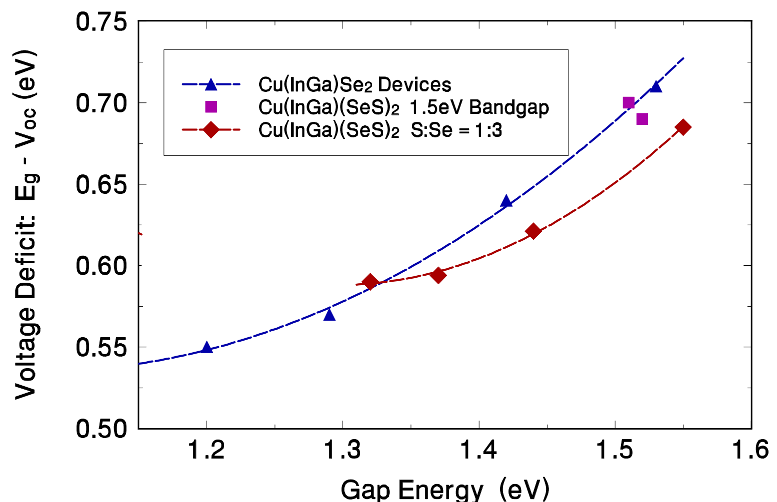

FIG. 23. The voltage deficit vs. bandgap energy for a range of $Cu(InGa)Se_2$ and $Cu(InGa)(SeS)_2$ sample devices fabricated at IEC. Note that the sample devices with S/(Se+S) ratios near 25% seem to indicate improved values of V_{OC} at higher bandgaps.

FIG. 24(a). The voltage deficit vs. Urbach energy for a wide range of $Cu(InGa)Se_2$, $CuIn(SeS)_2$ and $Cu(InGa)(SeS)_2$ sample devices fabricated at IEC. Note that a majority of the devices with the smallest voltage deficits lie roughly in the range indicated by the two parallel solid lines.

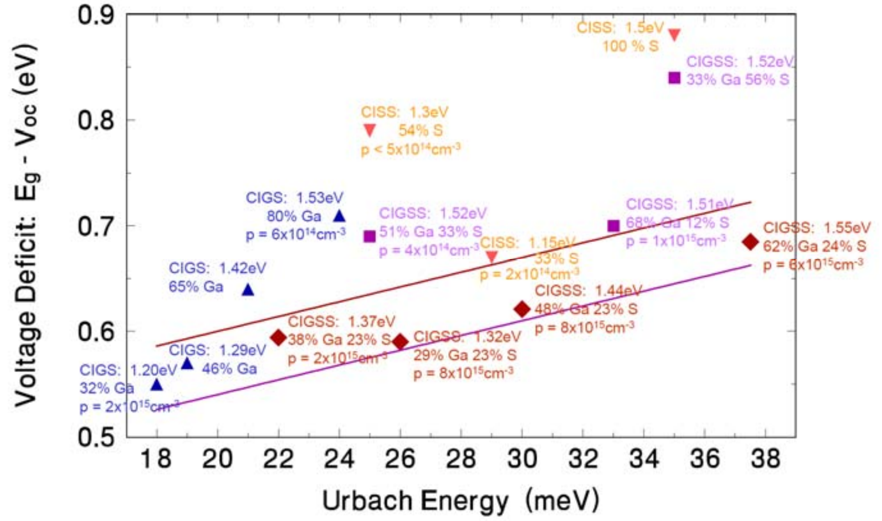

FIG. 24(b). The voltage deficit modified to reflect differences in hole carrier densities. This assumes that the hole quasi-Fermi level will be roughly the same as the dark Fermi level. The reference density (for which a zero correction was used) was taken to be 10^{16} cm^{-3}. Sample points for which no reliable hole carrier density could be determined have been omitted.

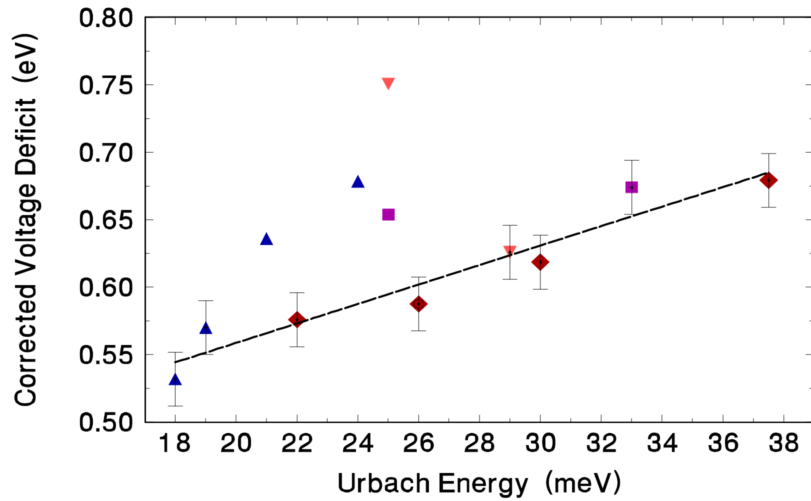

In the simplest analysis, V_{OC} should reflect the difference between the energies of the electron and hole quasi-Fermi levels under illumination and thus could approach but never exceed E_g/q. The hole quasi-Fermi levels for moderately p-type films are likely to lie close to the dark Fermi-levels near the back contact. Thus, a better comparison for devices with different hole carrier densities should be obtained if we subtract $k_BT\log(N_V/p)$ from the voltage deficit. This version is displayed in Fig. 24(b) and, indeed, indicates a large subset of these devices exhibit a simple linear dependence between their "corrected voltage deficit" and E_U.

To try to account for this linear relation (as well as the slope of fitted line) we propose the following argument: If the number of deep recombination centers is low, and if the electron quasi-Fermi level , E_F^n, does not become pinned at the barrier interface, then it will be limited by the conduction band-tail width. Such a direct role of the band-tail widths in setting a maximum allowed value of V_{OC} has been discussed in detail for the case of amorphous silicon based devices [20,21]. In these materials it is reasonable to assume that the broader band-tail (as revealed by our TPC spectra) lies near the conduction band edge. In that case, the electron

quasi-Fermi level will, as the light intensity is increased, ultimately begin to move into the lower portion of that bandtail. As this occurs, more and more of these bandtail states will begin to contribute to recombination [20]. In fact, it is quite reasonable to estimate that once the portion of the band-tail below E_F^n accounts for roughly 10^{16} cm^{-3} states, the electron-Fermi level will become pinned. Since the total density of bandtail states (for a 25meV Urbach energy) lies close to 10^{19} cm^{-3}, this implies that: $E_C - E_F^n \approx E_U \log[(10^{19}\ cm^{-3})/(10^{16}\ cm^{-3})] \approx 7E_U$. This is identical to the slope of the line displayed in Fig. 23(b).

This implies that V_{OC} will be limited in a manner that can be quite easily predicted for sample devices containing CIS alloys that are substantially disordered (large values of E_U). On the other hand, other recombination centers, such as deep defects near midgap, are dominant in limiting the value of V_{OC} for alloys such as $Cu(InGa)Se_2$ since the Urbach energy remains narrow as E_g increases. We can therefore predict that V_{OC} would be increased in the $Cu(InGa)(SeS)_2$ alloys if one could fabricate materials that are more highly ordered. However, if that could be achieved then other recombination pathways (such as the deeper defects) will become dominant. Thus, although we believe it should be possible to significantly increase V_{OC} by decreasing the alloy disorder in these CIGSS samples, there is no way to predict in advance how much of an increase one might expect to obtain in this manner.

5.0 RESULTS FOR THE $CuGaSe_2$ DEVICES

During the final year of our Subcontract we also spent some time examining and comparing the electronic properties of two series of $CuGaSe_2$ (CGS) wide-bandgap solar cells. As described in Section 2, the CGS sample devices for these studies were obtained from NREL and from IEC, and the characterization of the electronic properties of these devices was carried out by Dr. Heath and her students at Linfield College. The two series of samples were produced by slightly different techniques, namely a uniform single-step process at IEC and the three-step process at NREL. In this section we will denote these two sets of samples as series "A" and "B", respectively. The cell performance parameters of the seven samples studied are listed in Table VIII below.

Table VIII. CGS based devices from both IEC and NREL examined in the current study More details about these samples are given in Sections 2.1 and 2.2.

Sample	Source	Efficiency (%)	V_{oc} (V)	J_{sc} (mA/cm^2)	FF (%)
A1	IEC	5.6	0.81	10.0	68
A2	IEC	5.1	0.84	10.2	60
B1	NREL	3.5	0.70	8.7	57
B2	NREL	6.95	0.75	14.5	64
B3	NREL	6.2	0.73	13.9	61
B4	NREL	6.8	0.81	13.5	62
B5	NREL	7.83	0.80	15	66

FIG 25 (a) 75 µm x 75 µm TOF-SIMS image of the integrated Na signal across $CuGaSe_2$ sample A-1, indicating lateral variations in sample composition. Cross sectional images in the xz & yz planes are in next 2 panels, indicating that the CGS films are uniform in the z-direction. **(b)** Similar TOF-SIMS maps for sample B-1 indicating good lateral uniformity. Instead one sees increased z-direction variation due to the nature of the 3-stage process.

In all panels: **Na is shown in red**, **Cu in green**, and **Mo in blue**.

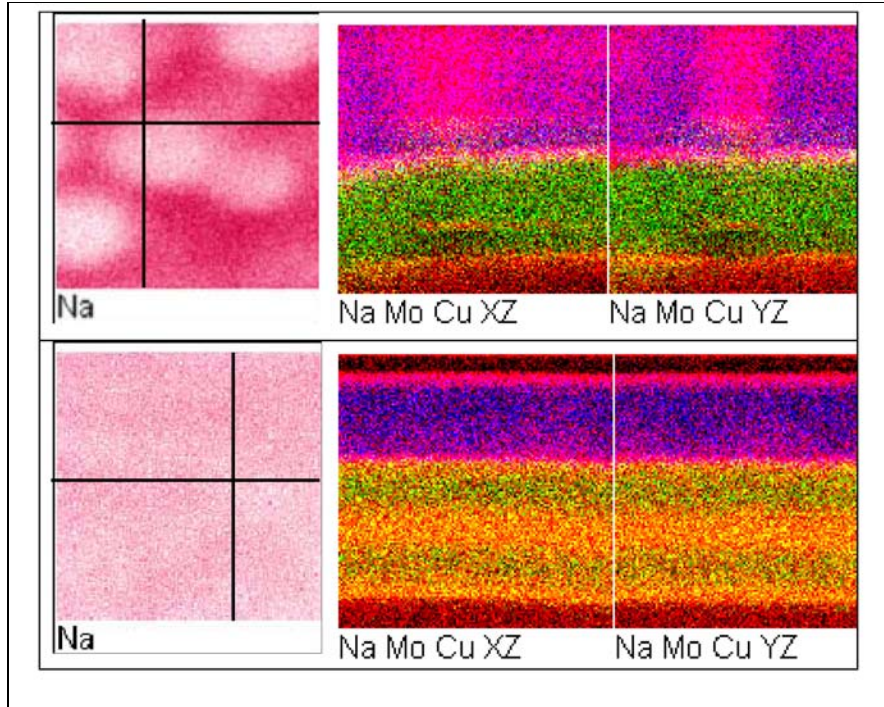

5.1 COMPOSITION UNIFORMITY ISSUES

In initial deposition runs, a distinct segregation of phases was observed in SEM and EDX images of the CGS layer, as has also been observed by others.[22] Following reports in the literature, the Se flux was increased until the phase segregation disappeared.[23] Device composition was further investigated with the University of Oregon's ION-TOF time-of-flight secondary ion mass spectrometer (TOF-SIMS). In this measurement, the sample was alternately exposed to a 98 nA Bi beam for measurement, and sputtered with a 740 nA O_2 beam. To verify that elements from the surface layers were not driven into the CGS film by the ion beam, half of the samples were etched with a 10% HCl solution at room temperature for one minute. Depth profiles verified that this effectively removed the surface layers while leaving the CGS film intact. In direct comparisons of etched and unetched films the CGS layers looked identical.

The TOF-SIMS results are displayed in Fig. 25. These data reinforce the premise that the different sets of samples are distinctly different. Film series A appeared to be less uniform spatially, both in composition and in thickness. The Na content and spatial distribution also differs distinctively between the two sample sets. While the high Se flux did eliminate strong regions of secondary phase from series A, these films still display a spatial variation in Na content, with distinct regions having Na contents 3-5 times greater than the matrix, as illustrated. These regions are on the order of 10 µm in size, and also have Cu/Ga ratios which are reduced about 25-35% from those in the matrix. Determination of whether these regions have inclusions of other compounds like $CuGa_3Se_5$ or $CuNaGa_2Se_4$ will require further study, but it is likely that such non-uniformities create fluctuations in the built-in voltage, and are detrimental to device performance. Depth profiles of films in series A also indicated that in regions of high Na

content, the CGS films are significantly thinner, as is also evident in Fig. 25(a). This is likely a true variation in thickness, as opposed to indicating a variation in sputtering rate, because we do not see strong variations in the Cu and Ga signals. Despite the lateral variations in elemental composition, depth profiles of the films indicated uniform Cu, Ga, and Se composition in the *z*-direction.

The CGS compositional maps for sample series B had uniform thickness and composition laterally and through their depth, to the limits of our resolution, which was on the order of a micron. The depth profiles indicated significant spikes in Na content near the top and back interfaces. This is also consistent with other results on films grown under high Se flux. [23]

5.2 CURRENT-VOLTAGE CHARACTERISTICS

The *J-V-T* dependence of these devices was investigated to learn more about mechanisms limiting the device performance. The illuminated *J-V-T* data are typically described using the ideal diode equation and assuming the saturation current density, J_0, is thermally activated. [24,25]

$$J \approx J_0\left[\exp\left(\frac{q(V-JR_s)}{nk_BT}\right)-1\right]-J_L \approx J_{00}\exp\left(\frac{-E_a}{k_BT}\right)\exp\left(\frac{q(V-JR_s)}{nk_BT}\right)-J_L\,. \qquad (6)$$

Here, n is the ideality factor and J_L is the light-induced current. The value of J_L equals the short circuit current, J_{sc}, for ideal samples. If n and J_{00} are independent of temperature and voltage, a plot of open circuit voltage, V_{oc}, versus T gives the activation energy E_a:

$$V_{oc} \approx \frac{E_a}{q} - \frac{nk_BT}{q}\ln\left(\frac{J_{oo}}{J_{sc}}\right). \qquad (7)$$

A typical plot of V_{oc} vs. T is illustrated in Figure 26(a), yielding E_a. For recombination currents dominated by Schockley-Read-Hall recombination in the bulk CGS film, $E_a = E_g$, while if

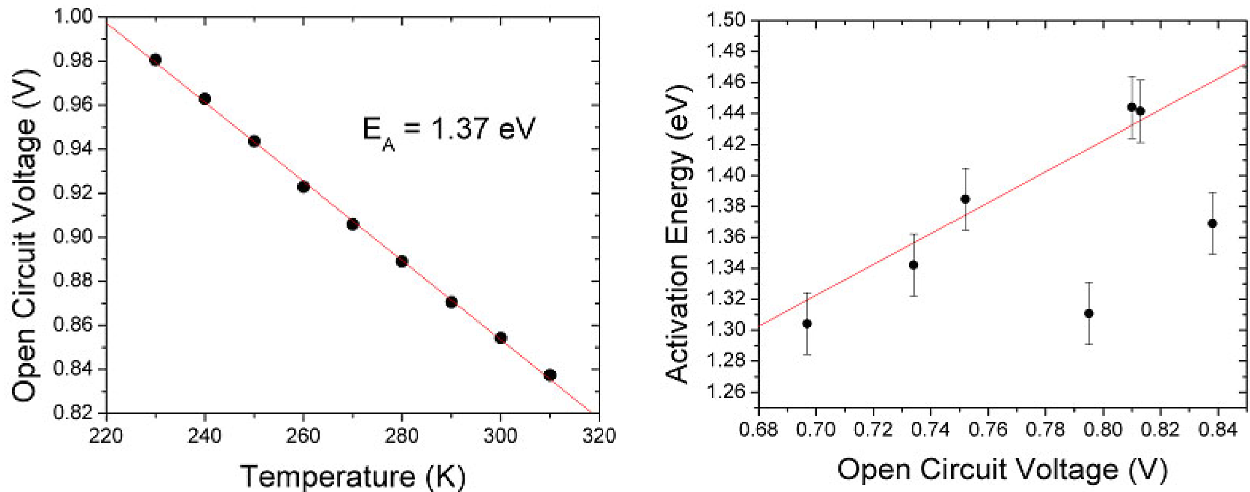

FIG 26. **(a)** Linear relationship between open circuit voltage and temperature, yielding E_a=1.37eV for sample A2, using Equation 7. **(b)** Relationship between activation energy and open circuit voltage. A line with unity slope is drawn for reference.

Table IX. Activation energy (E_a) results from the IV analysis of the CGS devices. Densities listed are the sum of the hole carrier and deep trap densities deduced from DLCP measurements.

Sample	Source	Efficiency (%)	V_{oc} (V)	E_a (eV)	DLCP densities ($\times 10^{16}$ cm^{-3})
A1	IEC	5.6	0.81	1.44	2.0-3.0
A2	IEC	5.1	0.84	1.37	1.0-2.0
B1	NREL	3.5	0.70	1.30	10-30
B2	NREL	6.95	0.75	1.38	0.10-0.30
B3	NREL	6.2	0.73	1.34	0.15-0.30
B4	NREL	6.8	0.81	1.44	1.0-1.5
B5	NREL	7.83	0.80	1.31	2.5-5.0

recombination at the interface dominates, we expect E_a to be less than E_g and related to the position of the Fermi energy at the interface. [26] Other mechanisms can also affect the value of E_a, such as tunneling-enhanced recombination. [25] This analysis becomes non-trivial when n and/or J_{00} are strongly temperature or voltage dependent, as can occur in a variety of situations. In addition, n and J_{00} values likely vary between films measured in the dark and those under illumination.

In these devices, n was difficult to determine using typical analysis techniques[24], suggesting that the current collection is voltage dependent; its temperature dependence is hence difficult to gauge. We were able to obtain values of n using the V_{oc}-J_{sc} relationship for devices measured under a series of different light intensities. [27] Although this technique may also be limited by the problem of voltage-dependent current collection, it does give us another tool to approach the problem. For example, the values of V_{oc} and ln(J_{sc}) are linearly related for sample A2 at higher light intensities and yield values of n= 1.8±0.1 at room temperature. Temperature measurements indicated that n, as determined in this fashion, is not strongly temperature dependent. These results are consistent with the linearity of the V_{oc} vs. T data, shown in Fig. 26(a), from which we were able to obtain values of E_a . These values are indicated in Fig. 26(b) and listed in Table IX.

5.3 CAPACITANCE PROFILING MEASUREMENTS

These samples were also examined using drive-level capacitance profiling (DLCP). The deduced DLCP densities, N_{DL}, include the free carriers that respond at the depletion region edge, as well as dynamically responding deep traps. When the sample temperature is lowered (or the measurement frequency increased), deep traps no longer contribute to N_{DL}, and so the free carrier density can be obtained. These samples generally did show contributions from deep traps, as is common for CIGS devices.

Values of N_{DL} measured at 40 kHz frequency and 290K are included in Table IX, and are the sum of free carrier and trap densities in the bulk CGS film. The trap response freezes out below

about 250 K, though in measurements down to 80 K, conduction was not frozen out. Typical DLCP data are illustrated in Figure 27, which includes only two temperatures, 290K and 230K, and one frequency, 40 kHz, for clarity. Most samples have some spatial variation in response as can be seen in Figure 27, and this range is indicated in the Table. Defect and doping densities do not strongly correlate with device performance, unless they are over $2x10^{16}$ cm^{-3}. Note that these samples generally have lower trap densities than in those where trap-induced tunneling was found to be a significant factor. [28]

Because the CV profiles are influenced by any charge density which can change in tandem with the relatively slowly changing dc voltage, they typically show larger densities than DLCP, and they can show the influence of states near the interface as well. Sample series A exhibits a strongly voltage dependent CV density, as shown in Figure 27(a), which is highly suggestive of interface states. Essentially, we believe such voltage dependence occurs due to changes in occupation of the interface states with reverse bias. Sample series B does not show this effect.

In summary, these data indicate very different structural properties but, in spite of this, the device performance parameters are remarkably similar. We believe that sample differences originate not from slight differences in growth (uniform co-evaporation versus 3-stage methods), but rather from the presence of a high-enough Se flux to eliminate regions of off-phase material. This is despite the fact that both sets of samples were intentionally prepared under a very high Se flux. Moreover, the presence of off-phase regions in the CGS film does not seem to be as detrimental to the electronic properties as one might expect. Both sets of films have similar doping and bulk defect densities, shown by CV and DLCP results. The devices with off-phase regions did show significant densities of interface states, which could limit their performance through increased interface recombination currents.

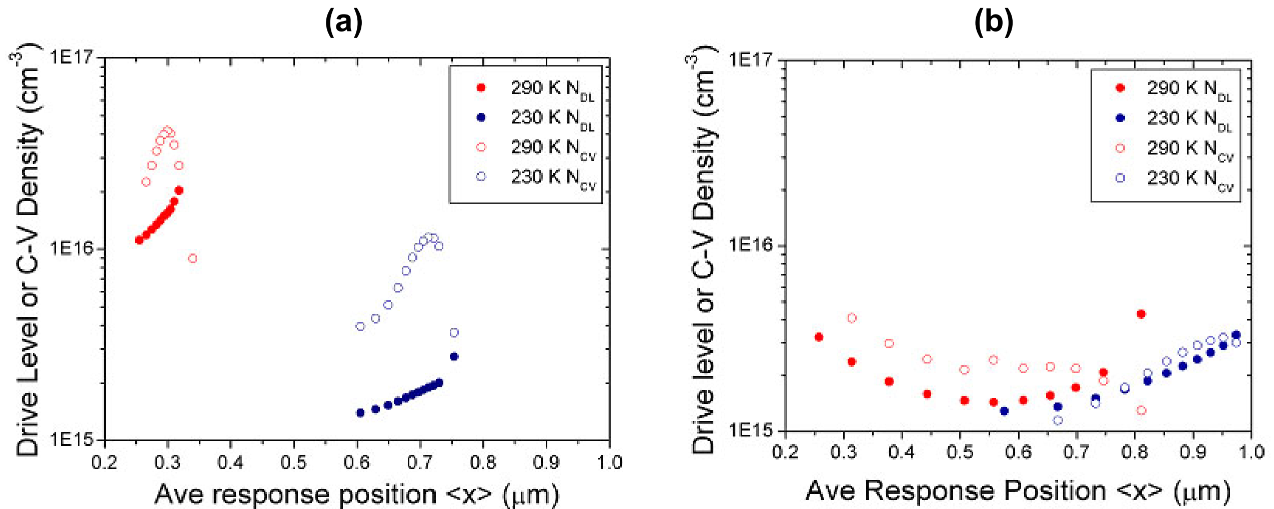

FIG. 27. Drive level capacitance profiling (DLCP) (solid symbols) and CV (open symbols) profiles at two temperatures for $CuGaSe_2$ sample **(a)** A2, and **(b)** B3. These figures illustrate the large discrepancy between DLCP and CV densities for samples in series A, likely related to near-interface states, not present in series B.

Given reasonable quality CGS films, the properties of the bulk film do not appear to limit the device performance. Instead, we agree with other authors that the interface with CdS could be problematic. Also, while interface recombination is expected to mainly impact V_{oc} [29], we note that the three samples with poor current collection all have either significant densities of interface states (A1, A2) or show a large number of traps overall (B1).

6.0 NUMERICAL MODELING OF DLCP AND CV-PROFILING DATA

6.1 MOTIVATION

In Fig. 28 we compare two sets of DLCP profiles obtained on one IEC CIGS device. Figure 28(a) shows profiles typical of those obtained by us for CIGS devices in the past. We believe we can interpret these profiles using via Eqs. (2) and (3), relating the DLCP density, N_{DL}, to an integral over the states in the gap between the neutral bulk Fermi energy, E_F^0, and the emission energy cutoff, E_e, for the states that can respond at (angular) frequency ω at temperature T (see Section 3.2). Thus, because for frequencies of 33kHz and higher the profiles reach a limiting value between 1.25 and 1.75 x 10^{15} cm^{-3}, we assume that these values correspond to the free hole carrier density in the absorber region of the device. In contrast, at lower frequencies (3.3kHz and smaller) a higher limiting value is reached, generally above 2 x $10^{15}cm^{-3}$. The difference between the low frequency and high frequency profiles is a bit more than 1 x $10^{15}cm^{-3}$, and we associate this with the deep defect (or “deep acceptor”) density given by the integral contribution in Eq.(3) when the emission energy cutoff, E_e, becomes large enough to encompass the defect’s entire energy distribution. The relatively small frequency range over which the upper and lower limits of these DLCP curves are reached indicates a deep acceptor band that is quite narrow, with a FWHM of less than 30meV. We note that there is a small spatial variation in these profiles, and we believe this reflects the true spatial variation of the free carrier and deep acceptor distributions within this CIGS absorber.

For the DLCP profiles obtained in Fig. 28(a) the range of applied biases varied between -1 volt to 0 volts. More recently we began examining the profiles obtained when we extended the range of DC voltages significantly into forward bias. Figure 28(b) shows such a set of profiles for the same CIGS device where now the range of applied bias was varied from -1.0 volts to +0.7 volts. In contrast to the profiles in Fig. 28(a), we now observe quite a substantial spatial variation in these profiles. In such cases, the assumptions allowing a straightforward interpretation of such DLCP curves using Eq. (3) becomes questionable, and therefore a more detailed analysis is required to uncover the actual spatial variation in the sample’s electronic properties. Moreover, the behavior of these profiles at the larger values of forward bias contains information about the defect distribution in the vicinity of the barrier junction itself. Such defects are likely to have a significant impact on the overall device performance. It is would thus be very interesting to obtain a more complete and reliable analysis of such experimental data.

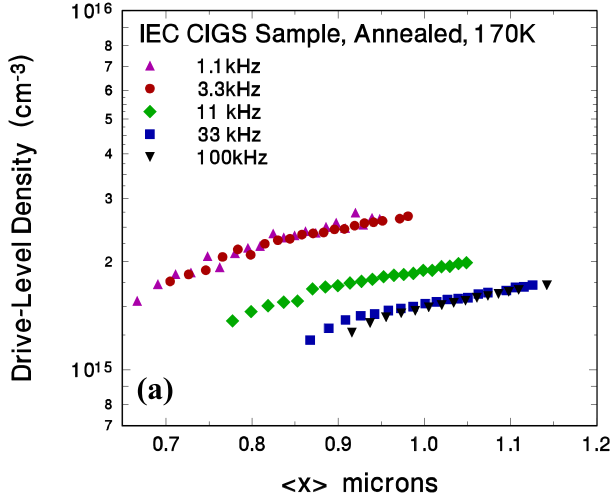

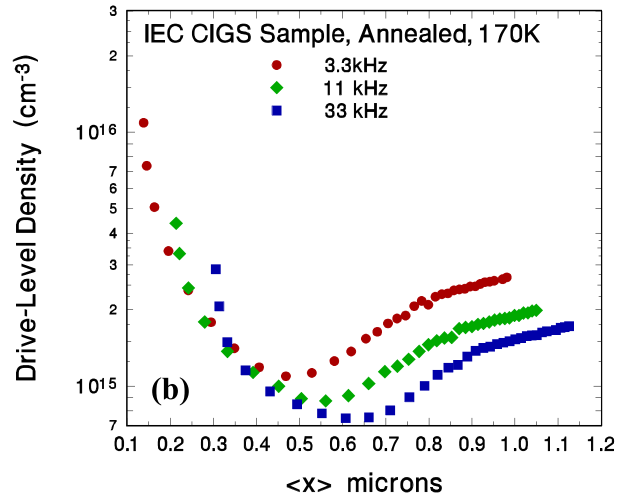

FIG. 28(a). DLCP curves obtained for a 30% Ga CIGS sample device 33927 at 170K for a range of frequencies. The applied DC bias was varied from –1V to 0V in 50mV steps. These data were obtained for the "annealed" state of this sample device, as described later.

FIG. 28(b). DLCP curves obtained for the same sample device. Here the applied DC bias was varied from –1V to +0.7V in 50mV steps. Note the change in vertical and horizontal scales compared to Fig. 28(a), and the large spatial variation of these profiles.

6.2 MODELING DETAILS WITH EXAMPLES

We had developed numerical algorithms and programs for carrying out such an analysis in our previous studies of a-Si:H devices.[30] We applied some of these old numerical analysis programs to CIGS devices a couple years ago to illustrate the advantages of drive-level capacitance profiling over standard CV profiling [31]. The algorithms used in these programs are different from those used in SCAPS modeling and so, unlike that program, our simulator readily allows an arbitrary spatial variation of the electronic properties to be examined. However, our approach cannot address effects on the admittance due to poor carrier mobilities. Fortunately, such effects are generally small until one begins to approach the temperature and frequency regime of dielectric "freeze-out".[32]

In these numerical simulations we solve the Poisson equation first at the nominal dc bias, and then increment this by several values of δV. Each value of δV results in a change of total depletion charge, δQ, which is found by numerically integrating over the entire depletion region. The temperature and frequency response is incorporated by imposing an emission time limit for the gap state response. Capacitance (C_0) is then determined by computing $\delta Q/\delta V$ for a very small value of δV (typically 10 mV), while the variation of capacitance with ac voltage amplitude (C_1) is found by repeating the calculation for larger values of δV. Thus, the numerical calculation requires none of the formalism leading to Eq. (3); it simply relies on Poisson's equation and the validity of $\delta Q/\delta V$ with an emission time limit to deduce the junction capacitance.

During Phase II of our NREL Subcontract we rewrote our DLCP modeling program to enable it to more specifically address CIGS devices and the types of profiles exhibited in Fig. 28(b). The modified program currently divides the CIGS absorber into three spatial regions uses the following input parameters to specify its electronic properties:

(1) The bandgap and temperature

(2) The shallow acceptor density in each of the 3 regions.

(3) The energy position, width and magnitude of a Gaussian-shaped deep defect band (the dominant majority carrier trap or "deep acceptor") for each of the 3 regions

(4) The thermal emission cutoff energy, E_e, determining what fraction of the deep defect band can respond at a given measurement frequency and temperature.

(5) The positions of the two boundaries separating the three spatial regions

(6) The degree of mixing across the two boundaries of the three spatial regions

The parameters describing this last attribute are extremely important for obtaining acceptable fits to the experimental data. At present, we use the same function parameters to control the spatial variation of both the shallow acceptor density and the deep defect density. The functional form that we have found to be reasonably successful is:

$$\rho(E,x) = [1-0.5\exp(-|x-x_{12}|/w_{12})\rho_1(E,x) + 0.5\exp(-|x-x_{12}|/w_{12})\rho_2(E,x) \quad (8)$$

where x_{12} is the position of the interface between regions 1 and 2, ρ_1 and ρ_2 are the charge densities characteristic of regions 1 and 2, respectively, far from that interface, and w_{12} is the length scale of the mixing between the regions near the interface x_{12}. Equation (8) specifically applies to the situation where we are in region 1 and near the interface between regions 1 and 2. A different mixing length scale can be chosen for each of the two interfaces. The appearance of the argument E in the charge densities indicates that the charge density at position x within the depletion region also depends on the electronic occupation of the defect band, which is governed by an energy demarcation depth, E. Figure 29 shows a screen plot from the actual program that exhibits the spatial variation of the shallow acceptors and deep defects for a particular choice of the above program parameters.

Figure 30 shows the results of a simulation of both drive-level and CV profiles that result from the input parameters of Fig. 29. The deep acceptor was chosen to lie 0.4eV above the valence band with a FWHM near 20meV. It was taken to have exactly the same energy distribution for all 3 spatial regions. Fig. 30(a) indicates that, at higher frequencies where the deep acceptors do not respond dynamically, the simulated DLCP (red) curve matches the ideal Eq. (3) result (green curve) fairly well. The CV profile is considerably higher because it also contains a contribution from the deep acceptor whose occupation will respond to changes in the

FIG. 29. Copy of a screen plot from the modeling program showing an example of the types of spatial distribution of shallow and deep acceptors that can be selected. In this case, the shallow acceptor density was chosen to be 5, 2, and 3 x 10^{15}cm^{-3} for the interiors of the 3 regions, respectively, (moving away from the barrier) and the deep acceptor density was chosen to be 3, 1, and 2 x 10^{15}cm^{-3} for the same 3 regions. The length scales that mix the properties at the two interfaces were 0.05 microns for the interface near 0.25 microns, and 0.2 microns for the interface near 1.0 microns.

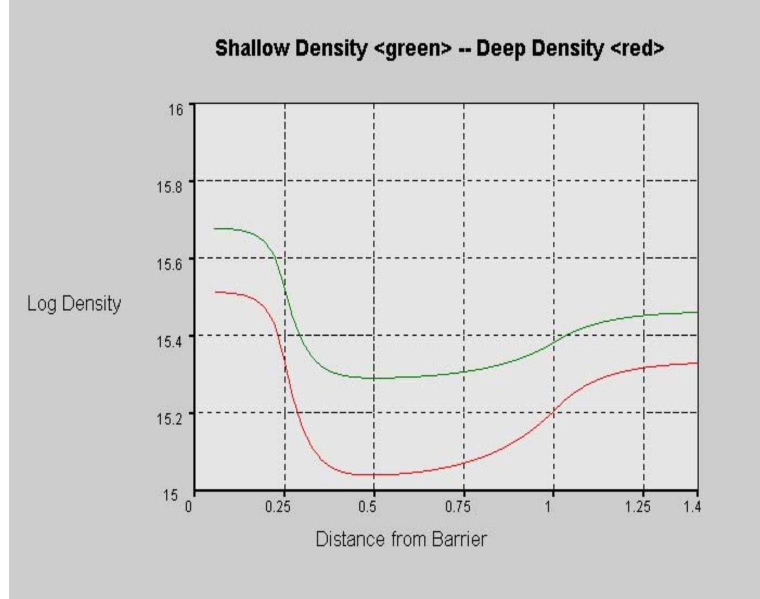

DC bias even though it cannot respond dynamically at the applied frequency. In Fig. 30(b) we show the simulated response at lower frequencies where the deep acceptor can respond fully. In this case both the DLCP and CV profiles appear nearly identical. However, neither provides an accurate picture of the true spatial variation of the states within the absorber. Actually, the measurement profiles do a pretty good job reproducing the true variation in the vicinity of the farther interface where the spatial dependence is relatively small, but they differ dramatically from the true spatial variation near the interface where the electronic properties are changing rapidly. This example clearly demonstrates the need for detailed numerical modeling when such more rapid variations in the spatial properties are present, such as those observed close to the

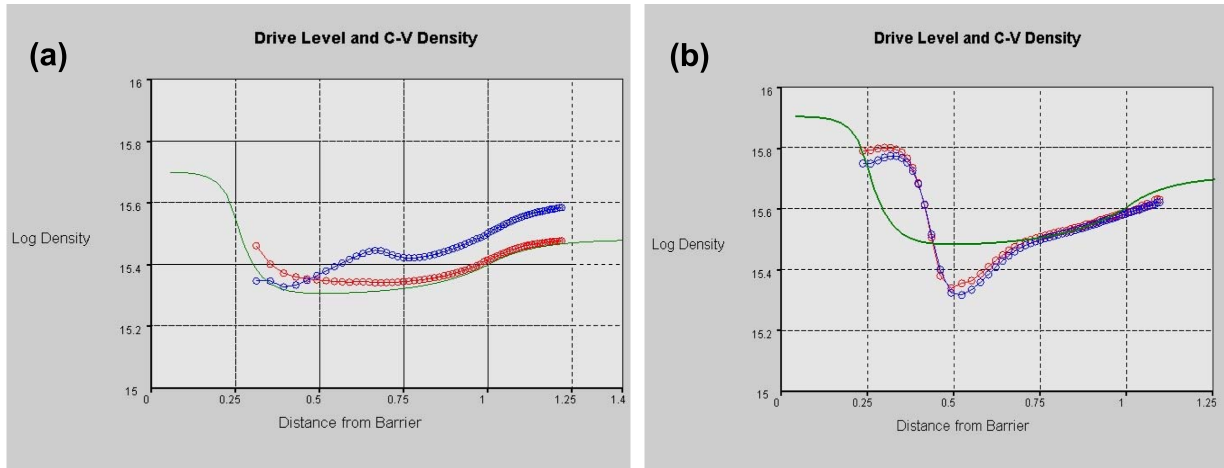

FIG. 30. Examples of calculated DLCP (red) and CV profiles (blue) for the model electronic properties shown in Fig. 29. Here **(a)** corresponds to a higher frequency measurement where the thermal response energy is 0.35eV, while **(b)** corresponds to a lower frequency measurement where the response energy is 0.45eV. The green curve shows the actual spatial variation of the charge density that will respond at 0.35eV and 0.45eV, respectively, from the assumed deep and shallow acceptor distributions.

barrier interface in the actual experimental data of Fig. 28(b).

Figure 31 shows the quality of fits to experimental DLCP we have been able to achieve thus far with our simulation program. The data employed are the actual 3.3kHz and 33kHz DLCP curves in Fig. 28(b). The following comments can be made concerning the quality of these fits and the information about the electronic properties of the CIGS absorber that can be inferred:

(1) The shallow and deep acceptor densities assumed in the region far from the barrier interface were taken to be equal, each at 1.8 x 10^{15} cm^{-3}. The values in the intermediated region were also taken to be equal and each reach a minimum at about 6.5 x 10^{14} cm^{-3} at a distance about 0.6 microns from the barrier interface.

(2) At the barrier interface the shallow acceptor density reaches a value of 6.2 x 10^{15} cm^{-3}, and falls off exponentially with a characteristic length of 0.25 microns [see Eq. (8)]. The deep state density able to respond dynamically (at lower frequencies) was much lower; about 1.1 x 10^{15} cm^{-3}. However, the CV profiles indicate that additional deep defects roughly equal to those of the shallow acceptor also lie in the near barrier region but are not able to respond dynamically even at the lowest measurement frequencies. (See Fig. 32 below.)

(3) The deep acceptor was assumed to lie 0.43 eV above the value band, with a narrow energy width (FWHM of 30meV). This may seem a surprising choice given that the activation energy obtained from admittance spectroscopy for the deep acceptor in this sample was close to 0.1eV. However, an acceptor level this shallow cannot account for the observed change in capacitance with frequency as exhibited in Fig. 28. The allowable limits for the energy position of the deep acceptor band have not yet been strictly determined; however, we believe we can definitely rule out values closer than about 0.3eV from the valence band.

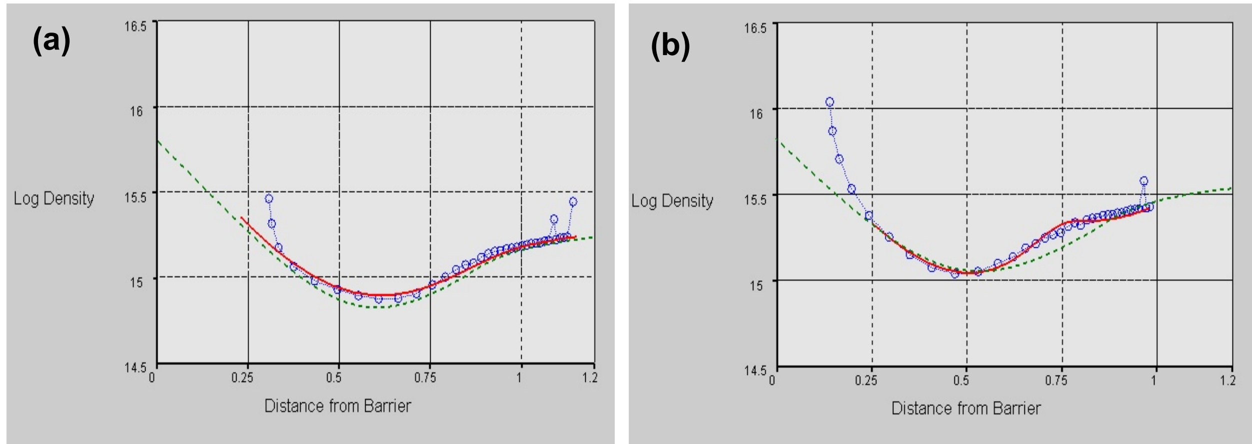

FIG. 31. Comparisons of simulated DLC profiles (red lines) to actual experimental data of Fig. 28 (blue circles) for the measurement frequencies: **(a)** 33kHz and **(b)** 3.3kHz. The green curves show the underlying spatial variations in the absorber that respond dynamically at 0.39eV and 0.46eV in the model density of states, respectively. The calculation assumed a built-in potential of 1.0 volts, and employed a range of DC biases from –1.3volts to +0.6 volts. The range of applied DC bias for the experimental curves was –1.0 volts to +0.7 volts.

(4) The agreement between the theoretical and experimental range of DC biases is actually surprisingly good, given that there are likely additional defects near the barrier region not discernable in the experimental profiles that also affect the extent of the depletion region at a given DC bias.

(5) The slightly different shape of the model profile compared to the experimental profile near 0.75microns in Fig. 31(b) actually reflects the spatial variation of the deep acceptor density near the barrier interface. Our calculation assumed that the spatial variation for the deep and shallow acceptor densities were identical. If we put in a slightly slower variation in the deep acceptor roll-off, we believe that this small discrepancy could be eliminated.

(6) The sharp upturn in the experimental profiles closest to the barrier actually reflect the electronic properties at the barrier interface itself. Indeed, the calculation indicates that the electronic properties at the barrier interface can influence these profiles at "distances" even as far away as 0.6 microns. Additional model parameters that address the electronic properties at the barrier interface need to be included before we will be able to extract more of the information contained within this portion of the experimental profiles.

To illustrate the effect of deep defects in the vicinity of the barrier interface we compare in Fig. 32 two simulations of the CV profiles with the 33kHz, 170K experimental CV profiles of this same sample. The only difference in the parameters between the two calculated curves was the inclusion (or not) of a deep band of defects near midgap of density 8.5 x 10^{15} cm^{-3} in a region located within a few tenths of microns from the barrier interface. Its occupation was allowed to vary with changes in the DC bias, but it was not allowed to respond dynamically at either 33kHz or 3.3kHz. The presence or absence of this deeper defect band had a negligible affect on the calculated DLCP curves shown in Fig. 31. However, as shown in Fig. 32, its affect on the CV profiles is quite significant. Even by including this deeper defect band the agreement with the experimental curve is not very good at profiles distances less than 0.6 microns. This indicates that the influence of deep defects near the barrier interface has still not been completely accounted for by the current parameters in our model calculation.

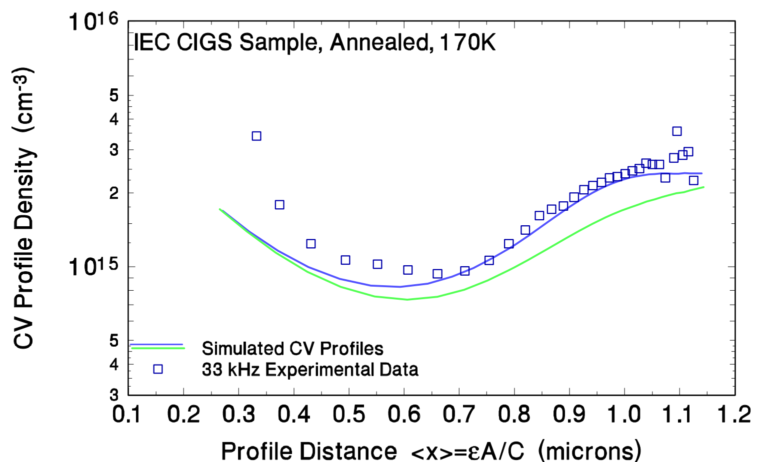

FIG. 32. Experimental 33kHz CV profiles at 170K compared with two model calculations, one with a deep defect band near midgap of density 8.5 x 10^{15} cm^{-3} (blue curve) and the other (green) without this defect band. This defect band was allowed to respond to changes in DC bias, but not allowed to respond dynamically at 33kHz. The assumed spatial variation of this defect was the same as the other defects in the near barrier region.

7.0 METASTABILITY STUDIES TO INVESTIGATE THE ROLE OF DEEP ACCEPTOR STATES IN LIMITING CIGS DEVICE PERFORMANCE

We have carried out detailed studies in which we utilized light-soaking treatments of CIGS sample devices to modify the electronic properties of the absorber in a metastable fashion. For example, by soaking with 780nm monochromatic light at an intensity of 50 mW/cm^2 for 100 hours we could typically increase the hole carrier density in the CIGS absorber, as well as the density of the commonly observed 0.3 eV bulk deep acceptor, by roughly a factor of 5. Furthermore, at each stage we observed that these increased in a 1-to-1 ratio. Initially we focused upon the creation kinetics of this process, and upon relating the observed changes to a defect creation model proposed by Lany and Zunger [33]. More recently, however, we have focused upon how the deep acceptors created in this process impact the performance parameters of the solar cell. We believe that such a study has enormous value because the link between the densities of specific defect states, or other electronic properties of the film, and the device performance has been very difficult to make [34]. Reasons for this may include: (1) The chemical variability of the material that makes it difficult to deposit a repeatable series of samples, such that the density of a specific defect density in the CIGS film itself is varied, but all other aspects of the device (e.g., interface properties and grain boundaries) remain the same [35]; (2) The influence of the contact layers on the absorber composition itself requires that CIGS film properties must be studied within the completed device, and bulk film properties must be distinguished from those of the interface. Investigating the effects of metastable changes in the absorber properties on the cell performance, on the other hand, potentially affords us the opportunity to focus in on effects of a few specific changes in the CIGS absorber while keeping most of these other cell characteristics constant.

7.1 GENERAL ASPECTS OF METASTABLE CHANGES IN CIGS

7.1.1 Experimental Procedures

To explore the general behavior of metastable changes in the Cu(InGa)Se_2 absorbers we applied the treatments on the CIGS photovoltaic devices (light exposure or forward bias current injection) at 250K to minimize any thermal annealing of the metastable effects. Indeed, we were able to fully reverse any induced metastable changes by annealing for 10 minutes at 340K. We chose 250K because we had established that significant annealing of the light-induced metastable defects occurs only at temperatures above 260 K. For the majority of our optical treatment we employed a 780 nm laser diode source that could provide intensities up to 1000 mW/cm^2. To investigate the wavelength dependence, a second laser diode source at 980 nm was employed. Metastable changes were also induced in the dark using forward bias current injection up to values of the short circuit current under AM1.5. Thus we could compare the effects of optical carrier generation with the effects of current injection. After each treatment, the sample was rapidly cooled to 125 K before characterization using the junction capacitance methods.

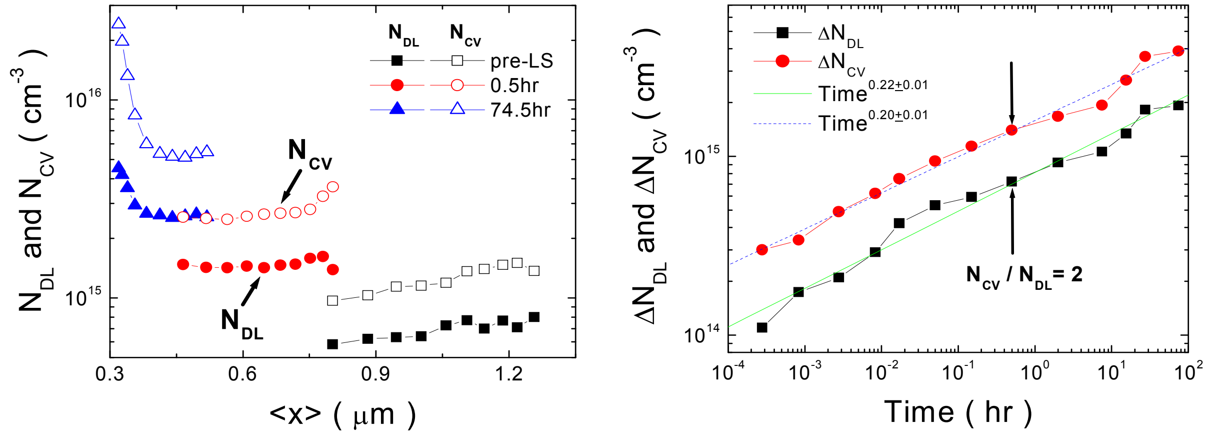

Figure 33. (a) Set of 1 MHz DLCP profiles and corresponding set of C-V profiles at 125K for one CIGS sample for increasing illumination times. These metastable states were created by a 780nm monochromatic light exposure at 250K. (b) Compared with DLCP profiles, C-V profiles are roughly a factor of two larger than corresponding DLCP profiles throughout exposure time

Two techniques were used to distinguish changes in the carrier density, p, from changes in the metastable defect density, N_T, with equivalent results. Both are based on the idea that the deeper traps are not able to respond to very fast changes in the applied voltage, but will respond to slower changes in bias. In the first method, employed previously [11], DLCP measurements at high and low frequencies (40 kHz and 1 kHz) were used to yield p, and the sum p + N_T, respectively. In the second method, 1MHz DLCP measurements and standard C-V profiles were compared at 125 K, again to yield p and p + N_T, respectively.

7.1.2 Experimental Results

A set of DLCP and CV profiles for a series of metastable states following different periods of light soaking at 780 nm are shown in Fig. 33. Here it is already apparent that the N_{CV} values are roughly a factor of two larger than N_{DL} for each of these states, implying that changes in p and N_T are approximately equal. Figure 33 also illustrates that while light-induced changes continue up to nearly 100 hours of exposure, significant effects occur in less than one minute of light soaking. We also note that, after about 20 hour exposure, both profiles start to bend upward near the interface, perhaps suggesting larger metastable changes near the barrier junction.

The 1:1 relationship between p and N_T is quite clearly displayed in Fig. 34. Here we have included metastable changes following a variety of exposure times over a wide range of intensities (factor of 30), different wavelengths, and also those induced by forward bias current injection in the dark. Thus, the 1:1 relationship between changes of N_T and p is independent of the method used to create the metastable changes. Not only do the values of N_T and p change in the same manner either with optical exposure or forward current injection, but when a similar

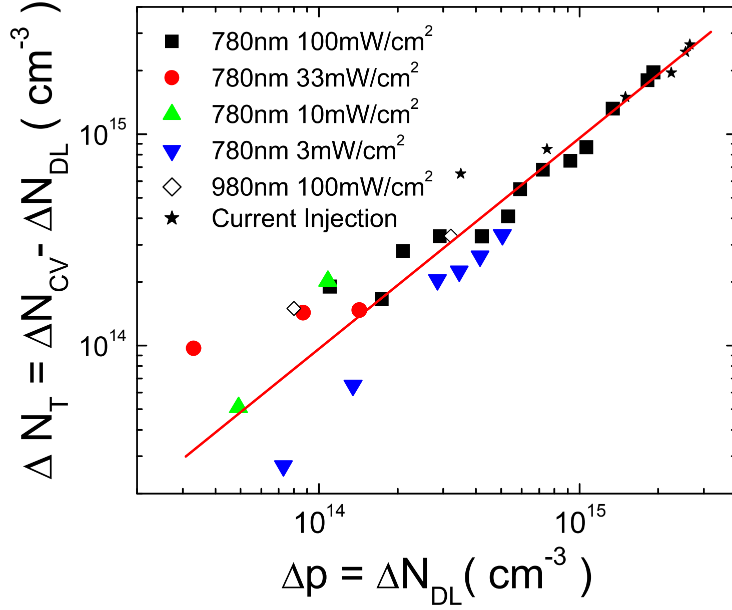

Figure 34. A 1:1 ratio is observed between increases in the deep trap densities and those of the hole free carrier densities in the bulk CIGS after different intensity light exposure. The line indicates a strict 1:1 ratio.

current density of 32.4 mA/cm^2 is employed they also appear to increase at a similar rate, by about a factor of 2 in 10 minutes.

The kinetics of the metastable state creation is remarkably independent of light intensity, as illustrated in Figs. 35 and 36. Changes in metastable defect densities were found by subtracting the initial state DLCP density from those at later times. The data appear to follow a strongly sub-linear time dependence ($t^{0.22\pm0.03}$) while the intensity dependence at fixed time was moderately sub-linear ($I^{0.53\pm0.06}$). However, the rate appears to become intensity independent above intensities of about 100 mW/cm^2.

7.1.3 Analysis

We believe that the independence of the metastable effect to either light excitation or forward bias current injection indicates that the capture of minority electron carriers into a particular type of gap state is the initiating event for the observed creation of the excess hole carriers and deep acceptors, N_T. The sub-linear time dependence shown in Fig. 35 provides further direct evidence as to the type of process that might be responsible. We first consider the simplest rate equation that might describe the creation of the N_T defects as a result of electron carrier capture:

$$\frac{dN_T}{dt} = C_1 n\left(N_P - N_T\right) \tag{9}$$

where n is the electron density in the conduction band, C_1 is a coefficient setting the overall rate, and N_P denotes the number of precursor sites that can be converted into N_T metastable states.

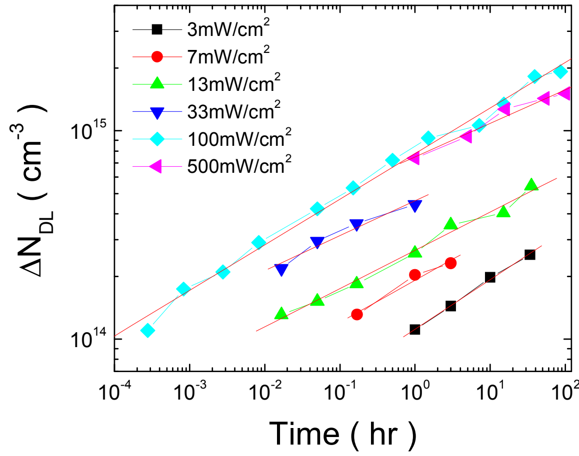

Figure 35. Comparisons of log(ΔN_{DL}) vs log(time) for different 780nm laser intensities. A similar power law time dependence is observed at all intensities with an exponent 0.22±0.03.

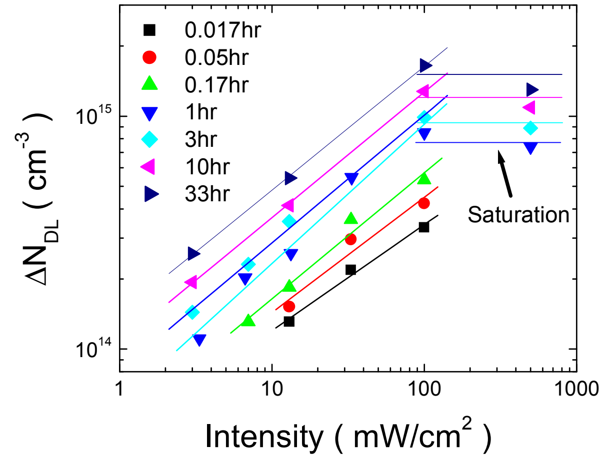

Figure 36. The dependence of the metastable effect as a function of the 780nm intensity, after various exposure periods, taken from Fig. 3. A power law dependence with exponent 0.53±0.06 is indicated except at intensities higher than 100 mW/cm^2 where saturation appears to occur.

The electron density in quasi-steady state is determined by the condition that the generation rate, G, (proportional to the intensity) be equal to the recombination rate, R:

$$G = R \propto N_R np \quad \text{or} \quad n \propto \frac{G}{pN_R} \tag{10}$$

Here we have assumed a bimolecular recombination process through recombination sites of density N_R [36]. Because these CIGS samples are p-type, the free hole density in the undepleted part of the absorber is not affected much by the light. However, as we discussed above, the hole density will increase slowly over time in direct proportion to N_T. Moreover, if we assume that the dominant recombination centers are the metastable N_T centers then we have $n \propto G/N_T^2$ and, inserting this into Eq. (9), we obtain

$$\frac{dN_T}{dt} = C'G\left[\frac{N_P}{N_T^2} - \frac{1}{N_T}\right] \tag{11}$$

If the density of precursor sites, N_P, is always much larger than N_T, then integrating Eq. (11) leads to the prediction that N_T (and hence also p) should increase as $t^{1/3}$. This is a somewhat faster rate than that observed in Fig. 35. However, if the number of precursor sites is limited then the growth of N_T will reach the asymptotic limit of N_P and the time dependence will appear to be slower than $t^{1/3}$. In that case it is possible to obtain a reasonable fit to the experimentally observed time dependence by a judicious choice of precursor density (i.e., a value close to 2×10^{15} cm^{-3}).

On the other hand, the $I^{0.53\pm0.06}$ dependence on intensity shown in Fig. 30 does not readily follow from Eq. (11) since this would predict an $I^{1/3}$ power law. Indeed, independent of the details of the quantity in brackets, Eq. (11) predicts that N_T should scale with time and intensity in the same manner, contrary to observation. This suggests we consider a different initial equation in place of Eq. (9), namely:

$$\frac{dN_T}{dt} = C_2 n^2 \left(N_P - N_T\right) \tag{12}$$

That is, we consider that the metastable conversion might be initiated by the capture of *two electrons* into the precursor site. We believe that such a mechanism would be consistent with the Lany-Zunger model as we discuss below. Moreover, this would help account for the very slow rates we observe for the defect creation mechanism. Now, if we combine Eq. (12) with Eq. (10) and assume the density of precursor states is very large we obtain:

$$N_T \propto \left(G^2 t\right)^{\alpha} \tag{13}$$

where α will lie in the range $0.2 \leq \alpha \leq 0.33$ depending on how much the metastable centers contribute to the recombination in Eq. (10). That is, if the N_T centers are the dominant recombination center then α should lie close to 0.2, while if other processes dominate recombination we expect α to lie closer to 0.33. Reasonable agreement to the data in both Figs. 29 and 30 is obtained for α lying near 0.25.

These results seem to us to be consistent with the microscopic model proposed by Lany and Zunger [33]. Indeed, their model involves the capture of two electrons into an initial configuration of a $(V_{Se}\text{-}V_{Cu})^+$ complex containing a doubly positive Se vacancy to drive it into a metastable $(V_{Se}\text{-}V_{Cu})^-$ complex, containing a metastable configuration of a neutral Se vacancy plus a filled copper vacancy plus 2 free holes. Then, for sufficiently p-type samples, this Cu vacancy will immediately capture one of these free holes to provide the 1:1 correspondence between the metastable changes in the free hole carriers and unoccupied deep acceptors that is observed.

7.2 THE EFFECTS OF METASTABLE CHANGES ON THE CELL PERFORMANCE

Both the electronic properties of the absorber layer and the JV characteristics of the device were measured in the annealed state (holding the sample for at least 10 minutes in the dark at 340K) and after 780nm light exposure times ranging from one minute to 75 hours. Because AM1.5 illumination that is normally employed to characterize device performance would rapidly change the metastable state of the sample, we documented the J-V characteristics using the 780 nm infrared light source at an intensity of 50 mW/cm^2. This also weighted the factors determining device performance more heavily toward the absorber region at some distance from the barrier interface. This is desirable because we wanted to focus on the effects of the bulk

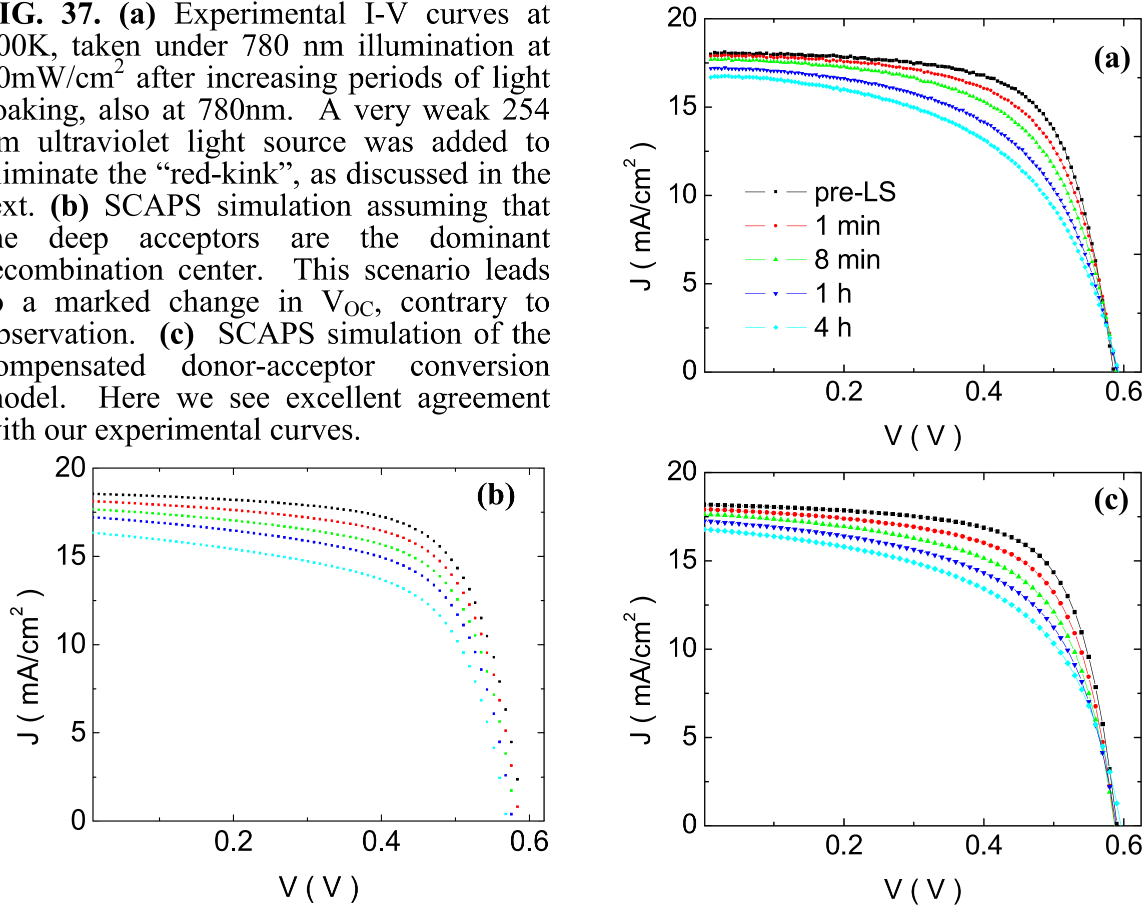

FIG. 37. (a) Experimental I-V curves at 300K, taken under 780 nm illumination at 50mW/cm^2 after increasing periods of light soaking, also at 780nm. A very weak 254 nm ultraviolet light source was added to eliminate the "red-kink", as discussed in the text. **(b)** SCAPS simulation assuming that the deep acceptors are the dominant recombination center. This scenario leads to a marked change in V_{OC}, contrary to observation. **(c)** SCAPS simulation of the compensated donor-acceptor conversion model. Here we see excellent agreement with our experimental curves.

absorber properties on the device performance. However, using purely 780nm light resulted in the so-called "red-kink" to appear in the JV curves [37]. To eliminate this, the infrared excitation was augmented by weak 254 nm ultraviolet light to enhance the conductivity of the CdS buffer and window layers. We found that this ultraviolet excitation improved the fill factor without affecting short circuit current or open circuit voltage. We will refer to these JV measurements using 780 nm light as JV_{IR} to avoid confusion with the more typically reported JV results measured under AM1.5 illumination. The experimental JV_{IR} curves are displayed in Fig. 36(a).

The initial device efficiency and fill factor, as measured under standard AM1.5 excitation, were 15.1 % and 0.77 respectively, with $J_{SC} = 31$ mA/cm^2 and $V_{OC} = 0.63$ V. In the JV_{IR} measurement, the annealed device had a short circuit current $J_{SC\text{-}IR} = 17$ mA/cm^2 and an open circuit voltage of $V_{OC\text{-}IR} = 0.6$ V. With infrared exposure, $J_{SC\text{-}IR}$ and FF_{IR} were observed to decrease, while $V_{OC\text{-}IR}$ remained constant, as displayed in Fig. 37(a). Under the same 4-hour treatment the hole carrier density was observed to increase from 5×10^{14} cm^{-3} in the annealed state to 1.3×10^{15} cm^{-3}, while the deep acceptor density was observed to increase from 1.5×10^{15} cm^{-3} to 2.3×10^{15} cm^{-3}. Note that in both cases the change was the same (8×10^{14} cm^{-3}).

7.3 ANALYSIS AND MODELING

From our high frequency admittance measurements described in Section 8 below, we determined a hole mobility of 2.7 cm^2/Vs for this sample in its annealed state with a free hole carrier density of $p = 8.2 \pm 0.5 \times 10^{14}$ cm^{-3} [38]. The dominant bulk defect response revealed by AS and DLCP was found to lie approximately 0.3 eV above the valence band edge, with a density of roughly $N_{DA} = 2 \times 10^{15}$ cm^{-3}. As noted above, the infrared exposure led to observed increases in both the hole carrier density and bulk defect response, with the changes in these quantities maintaining a 1:1 ratio, as previously reported [39]. Each of these increased by about a factor of 4 after four hours of infrared exposure, and continued to increase with extended light soaking.

The JV_{IR} data were first analyzed using the ideal diode equation, to check whether variations in the series and shunt resistance were occurring with the infrared exposure. Excellent fits were obtained, with no dependence of the curves on the shunt or series resistance. The diode ideality factor and open circuit voltage also remained the same regardless of the infrared exposure time of the device. Only $J_{SC\text{-}IR}$ and FF_{IR} appeared to be affected. This suggests that the observed changes in the device performance are likely related to the collection of photogenerated carriers in the absorber. The experimental results were also analyzed using SCAPS modeling. These calculations were constrained as tightly as possible by using experimentally determined parameters.

We first focused on the possible role of the 0.3 eV deep acceptor as the dominant recombination center in this CIGS device. In order to fit the experimental JV_{IR} curves and measured defect densities, the minority carrier (electron) capture cross-section μ_e had to be very large, on the order of 10^{-12} cm^2. This is consistent with previous modeling that employs the deep acceptor as the dominant recombination channel [40,41]. Since the density of this defect increases with the infrared exposure, this means that the recombination rate through this defect site should also increase. We were able to obtain reasonable fits in this manner to the JV_{IR} curves that agreed with the observed decreases in $J_{SC\text{-}IR}$ and Fill-factor, as shown in Fig. 37(b). However, we found that an increase in deep acceptor density would also caused a significant decrease in V_{OC}, contrary to the data of Fig. 31(a). This indicated that the 0.3 eV deep acceptor defect was actually *not* the only dominant recombination center in the absorber; rather, this recombination must instead (or also) be occurring through other sites such that the total recombination traffic remained constant independent of the metastable state.

The experimentally observed decrease in $J_{SC\text{-}IR}$, correctly simulated in the SCAPS modeling, actually has a straightforward interpretation. It simply reflects the fact that minority carriers must be photogenerated within the depletion region, or within approximately one diffusion length, L, of the edge of the depletion region, to be collected [42]. Because both the deep and shallow acceptors increase with exposure time, the depletion width becomes significantly narrower, and so the carrier collection will also decrease with infrared exposure. Such decreases

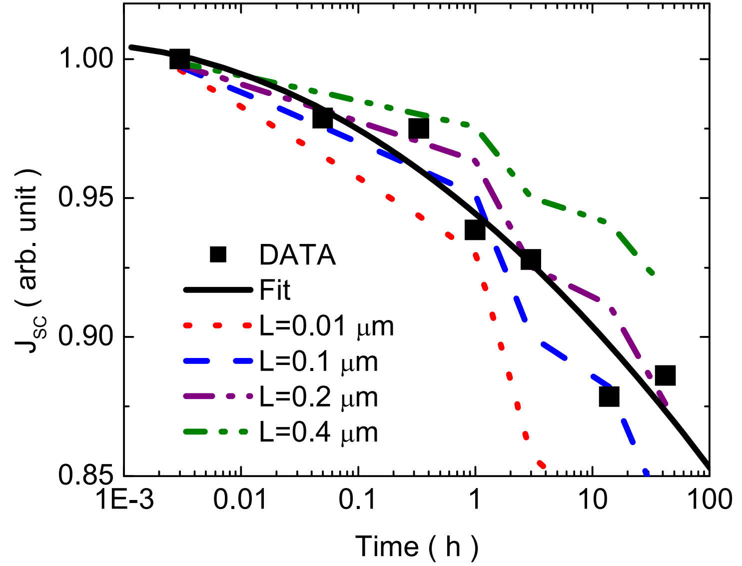

FIG. 38. Measured values of J_{SC-IR} at 300K vs. the light soaking time compared to several fits to Eq. (14) assuming different values of the electron diffusion lengths, L. The data are denoted by the black squares with the overall trend shown by the solid line. Dashed lines denote the photogenerated current collection based upon the measured depletion widths at each stage of light soaking assuming three different values forL. A good agreement to the data is achieved for L lying between 0.1 and 0.2 μm.

in carrier collection would also reduce the fill factor of the device, but would only affect the open circuit voltage by a very small amount.

The variation of the measured value of J_{SC-IR} and depletion width, W, (from the high frequency capacitance) with optical exposure actually allows us to estimate the minority carrier diffusion length, L, in this device. The relative magnitude of carriers collected for a depletion width W and minority carrier diffusion length L will be given by [43]

$$I_{L+W} \propto 1 - \frac{\exp[-\alpha W]}{\alpha L + 1} \tag{14}$$

where α is the optical absorption coefficient. Absorption coefficient of slightly smaller than $6x10^4$ cm^{-1} was used for simulation, based upon a spectroscopic ellipsometry study [44]. Comparing the variation of J_{SC-IR} with exposure time to that of I_{L+W} determined from the measured depletion width (obtained from the high frequency depletion capacitance values) suggests L lies between 0.1 to 0.2 μm (see Fig. 38).

Thus, the SCAPS modeling, together with the successful modeling of the variation of J_{SC--IR} with metastable state via Eq. (14), indicates that the recombination rate within the depletion region has to be kept nearly constant to reproduce the experimental results. That is, although the modeling indicates that there is significant recombination in the bulk absorber region of these devices, the recombination rate does not track with the density of the deep acceptor defect.

We next made an extensive study, using SCAPS, how a variety of other model parameters would affect the cell performance parameters. That is, we considered a wider range of hypotheses for how the metastable changes in the CIGS absorbers might actually be taking place. Figure 39 shows some examples of how SCAPS modeling predicts the assumed absorber properties will affect both the fill factors and V_{OC}'s of the cells. The model parameters examined in this figure include the bandgap, the deep acceptor density, the deep acceptor electron capture

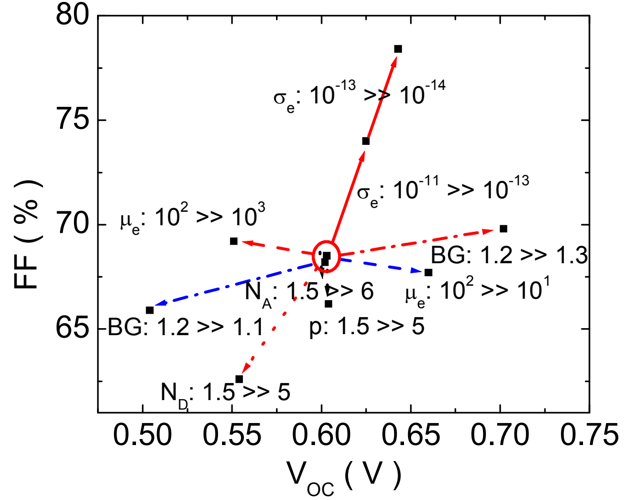

FIG. 39. Effects of changing absorber electronic properties on the cell fill-factor and open circuit voltage calculated using SCAPS. Parameters varied to produce this diagram included: the bandgap (BG) over a range 1.1 to 1.3eV, the deep acceptor density (N_A) from 1.5 x 10^{15} to 6 x 10^{15} cm^{-3}, the deep acceptor electron capture cross section (σ_e) from 10^{-11} to 10^{-14} cm^2, the hole carrier density (p) from 1.5 x 10^{15} to 6 x 10^{15} cm^{-3}, the density of a second deep, donor defect (N_D) from 1.5 x 10^{15} to 5 x 10^{15} cm^{-3}, and the minority carrier mobility (μ_e) from 10 to 1000 $cm^2V^{-1}s^{-1}$.

cross section, the hole carrier density, the density of a second deep (donor-like) defect, and the minority carrier mobility (variations in majority carrier mobility have nearly no effect). Thus, for example, one can see that variation in the deep acceptor density alone has only a very small effect, while an increase in an assumed deep donor defect decreases both the fill-factor and V_{OC}.

We have now examined 4 or 5 possible microscopic scenarios to try to account for the measured changes in the JV_{IR} cell performance together with the observed metastable increases in deep acceptor and hole carrier density. Motivated by the recent Lany-Zunger model for metastability in CIGS [33], we illustrate one particular fairly successful scenario in some detail. Here we have considered the conversion of (positively charged) deep donors to (neutral) deep acceptors with the accompanying increase of hole carriers to maintain charge neutrality. Table X lists the parameters used for the SCAPS modeling in the annealed (i.e., initial) state of the device. For the series of metastable states induced by light-soaking to obtain the JV_{IR} data in Fig. 37(a), we then increased the deep acceptor density in the manner determined from our DLCP measurements, while decreasing the magnitude of a mid-gap donor level (located at E_V+0.6 eV or above) by the same amount. The parameters used for this series of metastable states are listed in Table XI. The resultant calculated JV_{IR} curves are displayed in Fig. 37(c). The agreement with the experimental data in Fig. 37(a) is now quite good. In particular, this model naturally accounts for the fact that J_{SC} drops while V_{OC} remains nearly constant.

However, there is one complication in this otherwise successful analysis: to accurately account for the observed changes in fill-factor in the assumed defect conversion scenario, the charge density in the CdS layer had to be adjusted slightly (from 9.5 x 10^{17} to 8.7 x 10^{17} cm^{-3}). This may indicate actual metastable changes in the junction region (such as the fact that our DLCP profiles indicate an increased metastable deep acceptor level increase in the CIGS region near the junction). We are hoping that we can account for this inferred change in the CdS charge density by a more direct measurement in the future.

TABLE X. Baseline SCAPS parameters employed to model the JV_{IR} characteristics of the annealed state of our CIGS sample device.

Layer properties	CIGS	CdS	ZnO
Width (μm)	2	0.05	0.2
E_g (eV)	1.2	2.4	3.3
Dielectric Constant	13.6	10	10
N_{CB} (cm^{-3})	2×10^{18}	2.2×10^{18}	2.2×10^{18}
N_{VB} (cm^{-3})	2.2×10^{18}	1.8×10^{19}	1.8×10^{19}
μ_e (cm^2/Vs)	100	100	100
μ_h (cm^2/Vs)	5	25	25
p (cm^{-3})	3×10^{15}	9×10^{17}	9×10^{17}

Deep Defect Levels in CIGS Layer	Donor	Acceptor
Energies	E_V + 0.6eV	E_V + 0.3eV
Densities (cm^{-3})	2.5×10^{15}	1.5×10^{15}
σ_e (cm^2)	5×10^{-13}	5×10^{-13}
σ_h (cm^2)	10^{-15}	10^{-15}

Table XI. SCAPS parameters for compensated donor-acceptor conversion model. The values listed agree with the DLCP *experimentally determined* net free carrier densities ($N_A^{shallow} - N_D$) and deep acceptor densities (N_A^{deep}) which change with light soaking in a 1:1 ratio (see Fig. 34)

Metastable State	$N_A^{shallow}$ (cm^{-3})	N_D (cm^{-3})	p (cm^{-3})	N_A^{deep} (cm^{-3})	n_{CdS} (cm^{-3})
Pre-LS	3×10^{15}	2.5×10^{15}	0.5×10^{15}	1.5×10^{15}	9.5×10^{17}
1 min	3×10^{15}	2.3×10^{15}	0.7×10^{15}	1.7×10^{15}	9.1×10^{17}
8 min	3×10^{15}	2.1×10^{15}	0.9×10^{15}	1.9×10^{15}	8.9×10^{17}
1 h	3×10^{15}	1.9×10^{15}	1.1×10^{15}	2.1×10^{15}	8.8×10^{17}
4 h	3×10^{15}	1.7×10^{15}	1.3×10^{15}	2.3×10^{15}	8.7×10^{17}

7.4 BIFACIAL CELL RESULTS AND MODELING

We finally turn to some results we obtained studying metastable behavior on a bifacial cell. This bifacial CIGS solar cell was successfully fabricated at IEC to enable cross checks be employed in our investigation of the metastable changes in photovoltaic CIGS devices by comparing the solar cell performance obtained employing illumination either from the front or backsides of the samples. (However, light-soaking to produced metastable changes was always applied via the front-side.) Such samples employ a thin semi-transparent 40 nm thick layer of Mo (having a sheet resistance of 5 Ω/cm^2) on soda lime glass as their back contact. More details concerning how this CIGS sample (having a 30at.% Ga fraction) was fabricated are given in Section 2.1. The particular sample studied had a fairly good efficiency of 12.8% whereas the corresponding standard 700 nm thick Mo device had efficiency around 17%. Transmission vs.

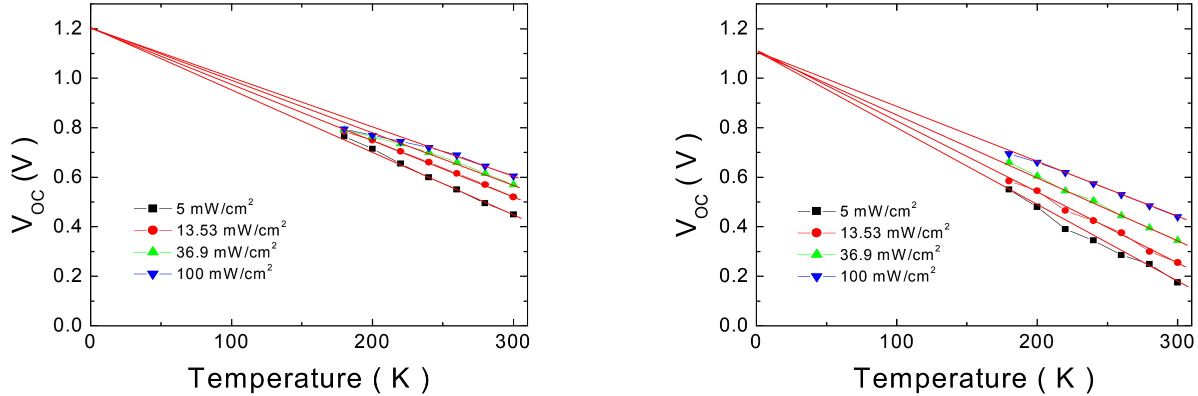

FIG. 40. Temperature-dependence of V_{OC} at 300 K under 980 nm for bifacial CIGS solar cell. **(a)** Front-side illumination **(b)** Back-side illumination.

wavelength through the 40 nm Mo layer was measured for wavelengths between 780 nm and 980 nm and was determined to be about 4 %.

First of all, we display the variation of V_{OC} with temperature for several different light intensities in Fig. 40 for both front and back side illumination. As was demonstrated in Fig. 37, V_{OC} does not vary appreciably with the light-soaking time. This was again found to be true regardless of whether we employed front or back side illumination for the I-V measurements. In Fig. 40 we observe that the front-side V_{OC} values extrapolated to 0 K indicate an intercept close to E_g/q for the annealed as well as the light-soaked states. This seems to confirm that the dominant recombination occurs within the bulk CIGS absorber itself [13]. The saturation of V_{OC} under front side illumination for temperatures below 200 K can be attributed to pinning of the quasi-Fermi level at the interface or bandtail recombination.

Under back-side illumination, the barrier height was found to slightly smaller, roughly 0.1eV lower than E_g. There are a couple possible explanations for this small difference; for example, we note that electrons generated by back side illumination have to diffuse back to be collected by the field gradient in the depletion region. The relatively short absorption length of 980 nm light creates an electron density gradient which leads to transport of the electrons toward the depletion region. Under open circuit conditions, a compensating hole current may be needed to cancel part of this, and thus lead to a small electric field outside the depletion region to move holes toward the front contact. Given the vastly greater hole density, this field would lead to a significant hole current without having much effect on the electron current. This electric field would then reduce the potential across the device.

Figure 41 shows the experimental IV_{IR} curves under front and back side illumination after an 8 hour light-soaking treatment. One sees that there is very little decrease in the photocurrent under reverse bias for the front side I-V curve but a considerable variation for the back-side I-V curve. This is reproduced quite accurately in the SCAPS simulation shown in Figure 42. This variation under backside illumination with increasing reverse bias reflects the increasing

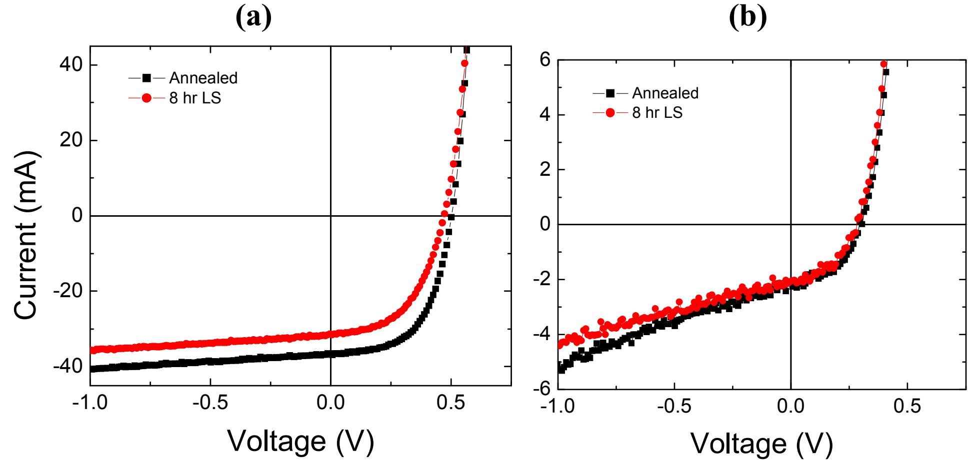

Fig. 41. Experimental I-V curves after 8 hours of light soaking, measured under 980nm monochromatic illumination from: **(a)** the front-side and **(b)** backside

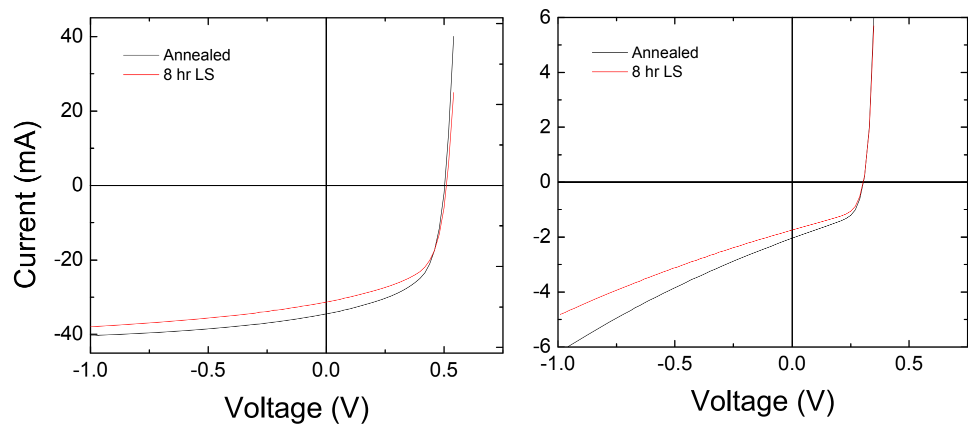

Fig. 42(a) SCAPS simulations for front-side illumination at 980nm. **(b)** SCAPS simulation using the same device parameters with backside illumination.

depletion width, enabling more minority carriers generated at the back of the device to diffuse into the edge of the high field and be collected.

We stress that exactly the same compensated donor-acceptor conversion model parameters were able to reproduce both the front and back-side IV_{IR} curves via these SCAPS simulations. This provides strong additional support for this model, and it indicates how changes in the mid-gap donor states occur to keep the open circuit voltage constant.

8.0 MEASURING HOLE MOBILITIES IN WORKING CIGS SOLAR CELLS

Hole mobilities in both epitaxial and polycrystalline CIGS materials have previously been determined in the traditional manner, using the Hall effect in conjunction with resistivity measurements.[45,46,47,48] Such measurements require insulating substrates with coplanar contacts and thus cannot be performed on working solar cell devices. Moreover, such devices employ CIGS layers that are comparable in thickness to the typical 1μm crystallite size. Thus, it is not clear how relevant such Hall mobility measurements may be for understanding the cell carrier collection. Therefore, as part the work performed under this Subcontract we developed and successfully demonstrated a method that reveals the majority carrier mobilities within working solar cell devices. This approach utilizes high frequency admittance measurements to deduce the resisitivity of the absorber layer, and then high frequency drive-level capacitance

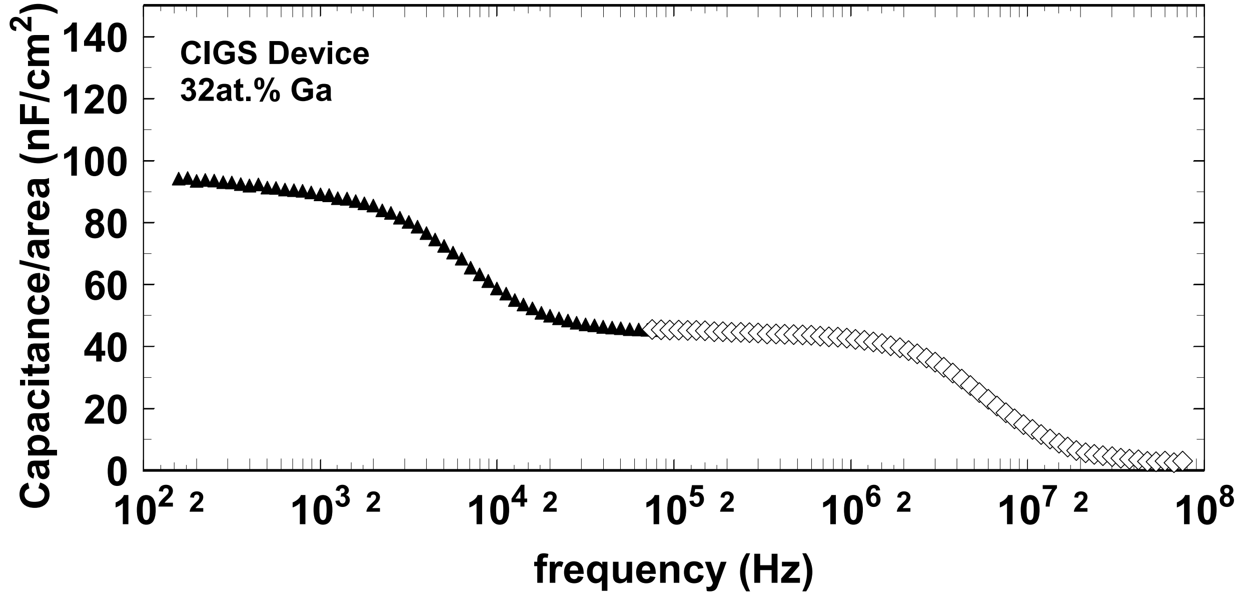

FIG. 43. Capacitance vs. frequency of CIGS solar cell obtained under 0V applied bias at 120K. The filled symbols were obtained using our standard low frequency capacitance bridge, and the open symbols were obtained using our newly implemented high frequency capacitance bridge and sample probe. Note the sharp decrease in capacitance above 3MHz corresponding to dielectric freeze out of the CIGS layer.

profiling (DLCP) to find the hole carrier densities. Thus, we then immediately obtain the hole mobilities. The polycrystalline CIGS devices for these measurements were fabricated at the Institute of Energy Conversion, and are described in Section 2.1 above.

8.1 CIGS CONDUCTIVITIES FROM HIGH FREQUENCY ADMITTANCE MEASUREMENTS

In Fig. 43 we display the results of applying both our standard capacitance measurements together with our newly implemented high frequency capacitance measurements on one such CIGS sample device. One clearly sees three regimes: (1) Frequencies, f, between about 10^4 and 10^6 Hz exhibit a nearly constant capacitance. This corresponds to the depletion capacitance of the CIGS sample junction, $C_d = \varepsilon A/W$, where W is the depletion width. (2) At frequencies below 10 kHz the capacitance increases and then reaches another higher plateau. This indicates the well-known additional response of deep defects within the depletion region. (3) Above 2MHz the capacitance decreases and reaches a much lower value. This is due to the dielectric carrier freeze out; i.e., where $1/f$ becomes shorter than the dielectric relaxation time $\rho\varepsilon$. This capacitance step can be clearly distinguished from other capacitance steps because, on the high frequency side of the step, the capacitance is *independent of applied bias* and approaches the geometric capacitance, $C_g \equiv \varepsilon A/t$, where A is the area and t is thickness of the film. In this high frequency regime the CIGS absorber essentially behaves as an *insulator* with dielectric constant $\varepsilon \approx 12\varepsilon_0$. Because the dielectric constant, ε, of CIGS is fairly well known, the identification of the dielectric relaxation time allows one to determine the resistivity of the undepleted portion of

FIG. 44. Equivalent circuit employed to deduce the dielectric relaxation time, and hence the resistivity, of the CIGS absorber within a solar cell device. This circuit consists of the depletion capacitance, C_d, in series with an infinite series of *rc* parallel circuits, each corresponding to an infinitesimal width, δx, of the undepleted portion of the CIGS layer. The value of *rc* of each such element is then equal to $\rho\varepsilon$, the dielectric relaxation time.

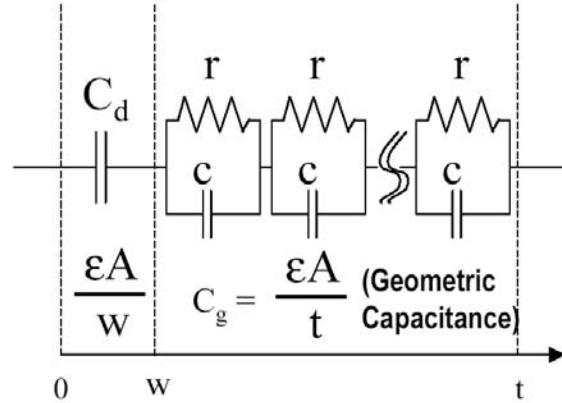

the CIGS film within the working device.

At frequencies higher than about 100kHz, the response of deeper states within the depletion region can be ignored. Thus, we been able to model the device simply as a depletion capacitance, $C_d = \varepsilon A/W$ in series with the undepleted bulk region of the CIGS absorber. The latter may be treated as a series of slices of infinitesimal width, δx [such that $\Sigma\delta x = (t\text{-}W)$], each having a capacitance $c = \varepsilon A/\delta x$, in parallel with a resistance $r = \rho\,\delta x/A$. The equivalent circuit for this analysis is shown in Fig. 44. Using this analysis we readily obtain expressions for the capacitance and conductive phases of the admittance response (here $\omega = 2\pi f$):

$$C = C_d \frac{1+(C_d/C_g)(\rho\varepsilon\,\omega)^2}{1+(C_d/C_g)^2(\rho\varepsilon\,\omega)^2} \qquad G/\omega = C_d \frac{[(C_d/C_g)-1](\rho\varepsilon\,\omega)}{1+(C_d/C_g)^2(\rho\varepsilon\,\omega)^2} \tag{15}$$

An example of using these to fit actual high frequency admittance data for one CIGS sample device is shown in Fig. 45. In fitting the data at –1V applied bias we found, as expected, that only the depletion capacitance C_d needed to be changed substantially, while the fitted value of $\rho\varepsilon$ remained the same (roughly 1.15 ns) within the statistical error. Assuming a dielectric constant of 11.7, this implies a resistivity of 1120 Ω-cm.

FIG. 45. High frequency capacitance (solid symbols) and conductance data (open symbols) on CIGS sample 33456 at a temperature of 125K and two different values of applied bias. The lines through the data points indicate fits obtained using Eq. (15). Essentially identical values of ρε were obtained for the two different DC biases.

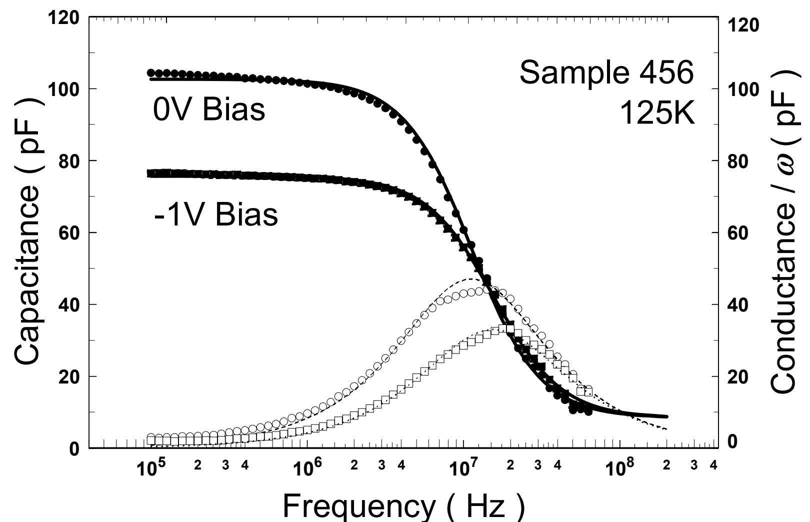

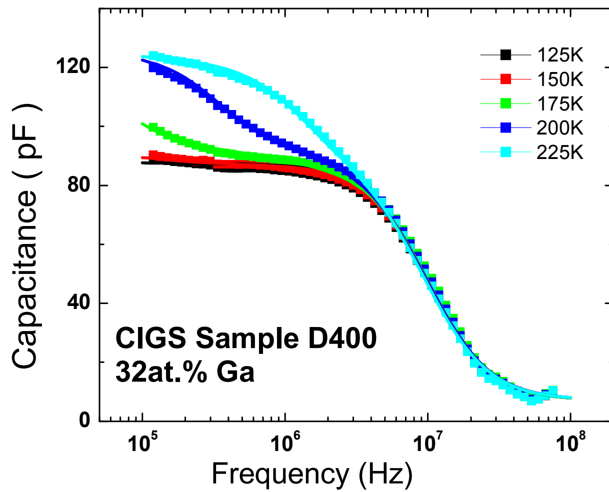

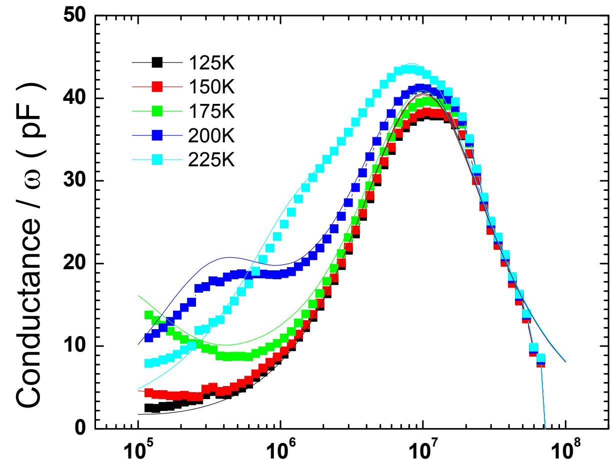

FIG. 46(a). Capacitance vs. frequency spectra at high frequencies for one CIGS sample at –1V bias. The data at each temperature have been fitted using the SCAPS modeling program with the parameters given in Table XII. Because the fits are so good, these lines mostly obscured.

FIG. 46(b). Conductance/w vs. frequency spectra at high frequencies that represents the real part of the admittance data shown in Fig. 7(a). The thin solid lines from the SCAPS model fit are also shown.

TABLE XII. SCAPS Model Parameters used to obtain fits to high frequency admittance spectra displayed in Figure 45.

Hole Mobility μ_h cm^2/Vs	Hole Carrier Density (cm^{-3})	Defect Density (cm^{-3})	Defect Energy eV above E_V	Emission Prefactor, ν (sec^{-1})
7.0	6×10^{14}	2.4×10^{15}	0.185	5.5×10^{10}

At higher temperatures the simple network analysis described above is insufficient because the deep acceptors can also respond in the same high frequency regime that is undergoing the dielectric freeze-out. This leads to more complex admittance behavior involving both the carrier dynamics and the deep state response. Although my laboratory has developed a fairly extensive admittance numerical modeling capability, our analysis does not take into account effects that arise when carrier transport is slow compared to the characteristic times of the applied frequencies. However, the SCAPS program developed by Marc Burgelman's group at the University of Gent includes this in their ac response analysis.[49] Thus, we also decided to try this analysis to find out if we could account for some of the more complex high frequency admittance data that is exhibited by the CIGS alloy samples at higher temperatures. An example of the types of complex admittance behavior that is observed is shown in Fig. 46.

Initial results were poor due to problems with the numerics when we assumed a Gaussian distribution for the deep acceptor energy distribution. However, these types of problems disappeared when we assigned the deep acceptor a single discrete energy. Since the deep

acceptor in these samples has quite a narrow energy distribution in any case, approximating it with a single discrete energy still allowed us to obtain quite good fits to the admittance data. These fits are indicated by the thin lines in Fig. 46. We believe that the small remaining discrepancies could be eliminated if the program allowed us to accurately calculate with narrow Gaussian distributions.

The parameters used to obtain the fits shown in Fig. 46 are listed in Table XII. Note that the thermal emission prefactor listed for the deep acceptor was taken to be independent of temperature.* These fits assumed a constant, temperature independent carrier density and mobility over the entire series of temperatures shown. Therefore, this strengthens our above conclusion that the conductivity is indeed nearly constant over the temperature regime between 125K to 225K for the set of CIGS samples obtained from IEC.

8.2 DETERMINATING THE HOLE CARRIER MOBILITIES

Once we know the conductivity, the hole mobility can be obtained once we have the hole carrier densities. These were found using the drive-level capacitance profiling (DLCP) method. At sufficiently high frequencies and/or low temperatures the deduced DLCP density should have little contribution from deep states and thus be dominated the hole carrier density, p. This should occur at frequencies just below the dielectric freeze out condition. However, in order for N_{DL} to reflect only the free carrier density close to freeze-out, it is important that the Fermi energy not be pinned at a region of high state density in the gap. Otherwise, even at freeze out, there may be a significant contribution to N_{DL} from such defects, resulting in an overestimate of the carrier density based upon this method. In Fig. 46 we display both the admittance and 1MHz DLCP data obtained at a series of measurement temperatures for the same CIGS sample as in Fig. 44. From Fig. 47(a) we see that 1MHz is indeed a reasonable choice since it lies well below the freeze-out regime that extends from about 3MHz to 20MHz. In Fig. 47(b) we see that, in fact, the value of N_{DL} is nearly independent of temperature between 125K and 175K, although it shows some spatial variation (less than a factor of 2 over 0.5μm). The N_{DL} profiles do appear to be indicative of the free hole carrier densities for this sample between 125K and 175K and, using the values of $\rho\varepsilon$ deduced from Fig. 45, we deduce a nearly temperature independent hole mobility in this temperature range of 7.5 ± 1.8 $cm^2V^{-1}s^{-1}$.

The major source of uncertainty in the determined mobility arises from the spatial variation in the free carrier density (the statistical uncertainty for this case is only ±0.4 $cm^2V^{-1}s^{-1}$). Above 175K the DLCP profile values increase and then reach a second plateau at about 245K. We can offer two possible explanations for this: Either a band of deeper states within the depletion region can respond at these higher temperatures and thus adds to the DLCP determined density, or the free hole carrier density actually increases as a band of deeper acceptors becomes fully

---

* If one assumes a T^2 temperature dependence to the thermal emission prefactor, then the activation energy for the deep acceptor should be decreased by about 30meV to 0.155eV.

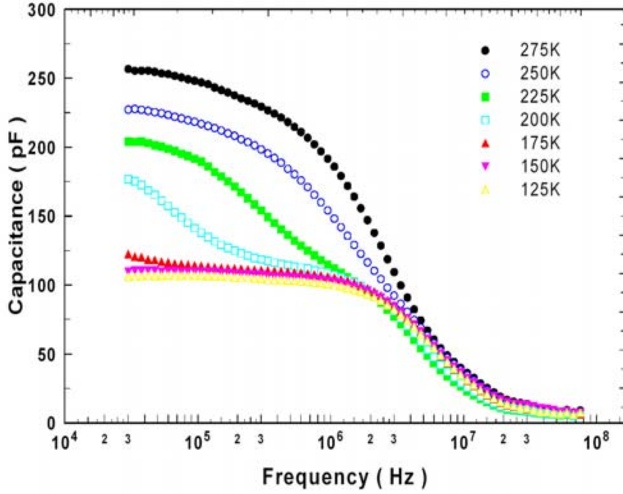

FIG. 47(a). High frequency admittance vs. frequency for the 27at.% Ga CIGS sample 33456 under 0V applied bias at several measurement temperatures.

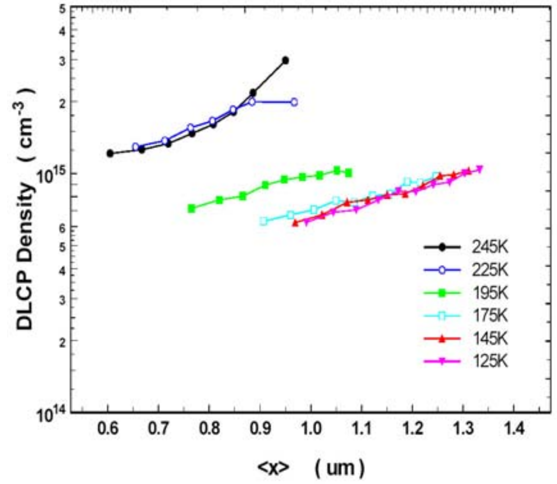

FIG. 47(b) 1MHz DLCP profiles vs. $\langle x \rangle \equiv \varepsilon A/C_0$ for a similar range of temperatures as in (a). These data imply a hole mobility near 150K of 10±2 $cm^2V^{-1}s^{-1}$.

ionized at these higher temperatures. For now we have restricted our estimates of the mobilities to the lower temperature regime (near 150K) where this issue does not arise.

Results of hole mobilities determined for six CIGS samples using this method are listed in Table XIII. We see that the 150K hole mobilities vary by nearly an order of magnitude, from about 3 $cm^2V^{-1}s^{-1}$ to over 20 $cm^2V^{-1}s^{-1}$. These mobilities do not appear to be correlated in any obvious manner to the cell performance. All of the mobilities listed lie well within the range of Hall mobilities determined previously for polycrystalline CIGS samples [45,46], and about an order of magnitude lower than Hall mobilities determined for epitaxial CIGS films.[47,48]

TABLE XIII. Summary of samples and the hole mobilities determined by high frequency admittance measurements. Cell efficiencies for each device sample are included. The deduced values of $\rho\varepsilon$, and the hole carrier densities determined by DLCP, are also indicated.

Sample #	Ga fraction (at.%)	Efficiency (%)	**p (10^{14} cm^{-3})**	$\rho\varepsilon$ **(ns)**	μ_h **(cm^2/Vs)**
33469	0	9.62	8.8 ± 0.6	2.5 ± 0.2	2.9 ± 0.3
33456	27	11.6	7.5 ± 1.5	1.15 ± 0.1	7.5 ± 1.8
33400	32	16.1	6 ± 0.5	1.55 ± 0.1	7.0 ± 0.8
33233	32	14.3	5.9 ± 0.8	0.92 ± 0.1	12 ± 2.1
33264	32	11.8	4.8 ± 1.1	0.77 ± 0.1	18 ± 4.0
33444	34	12.3	5.0 ± 0.4	0.58 ± 0.1	22 ± 4.2

8.3 HOLE MOBILITIES VERSUS METASTABILITY IN CIGS

In one attempt to gain some insight into the mechanisms limiting the mobilities in such samples, we examined one sample over a series of metastable states. As was discussed in some detail in Section 7.1, it has been well established that, in particular, the free hole carrier density can be increased significantly following long term light exposure [50,51], and that these changes anneal away within a few hours at room temperature. Exploiting such metastable effects, we measured both the high frequency admittance (10^5 to 10^8 Hz) and 1MHz DLCP profiles of one 32at.% Ga sample at 125K. We then light soaked this sample at room temperature using 780 nm monochromatic light at 100mW/cm^2 light intensity for 3 hours. It was then immediately cooled to 125K and re-measured. We found that both spectra changed significantly: the depletion capacitance increased by a factor of about 1.7, while the DLCP determined hole carrier density increased by roughly a factor of 2 [see Fig. 48]. However, the change in conductivity was by a much smaller factor, as indicated by the frequency of the dielectric freeze-out.

We next subjected the samples to a series of 10 minute isochronal anneals in the dark, beginning with 200K, increasing in 20K steps, until a 10 minute anneal at 320K had been completed. After each such anneal, the admittance and DLCP profiles were re-measured at 125K. Following the 320K anneal we found that the sample exhibited nearly the same characteristics as it had prior to light-soaking. These data are displayed in Fig. 48. Note that the admittance spectra exhibit a marked change even after the first (200K) anneal, while the DLCP curves do not change significantly until after the 260K anneal. We believe that the latter indicates the temperature at which the CIGS absorber properties begin to recover, while the changes in admittance seen at lower temperatures are restricted to changes in sample properties

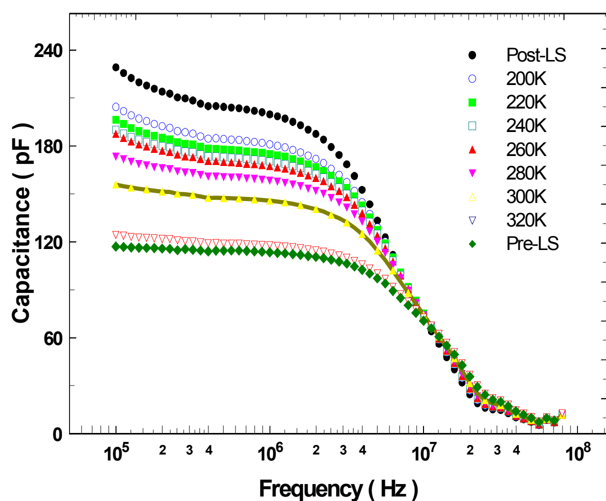

FIG. 48(a). Set of 125K admittance data at 0V applied bias for a sequence of metastable states of a 32at.% Ga CIGS sample (33400).

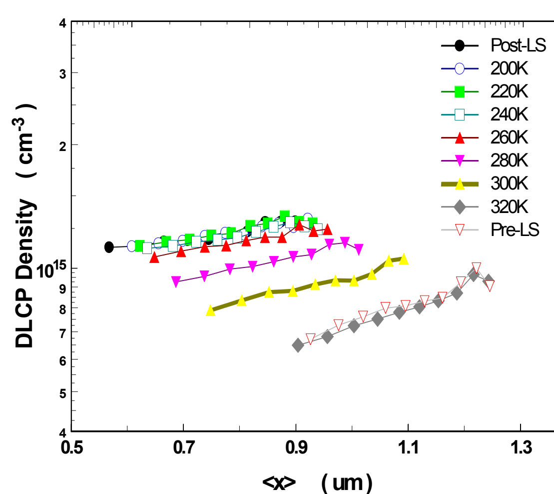

FIG. 48(b) 1 MHz DLCP data for the same metastable states as in (a). The sequence of 10 min. anneal temperatures are indicated.

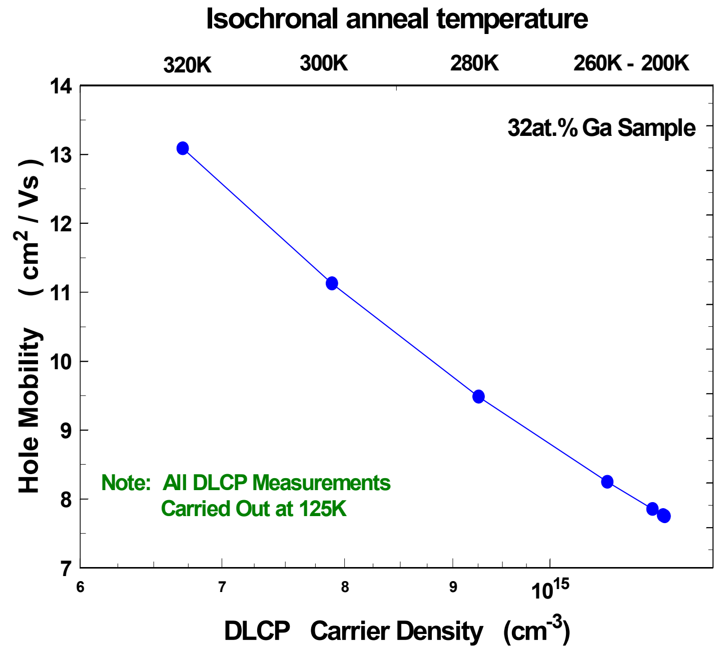

FIG. 49. Hole mobilities for the sequence of metastable states as derived from the data in Fig. 47. The inverse relation between the mobilities and carrier densities reflect the fact that the conductivity is nearly constant over this set of metastable states.

near the barrier junction (which effectively modify the built in potential and hence the depletion capacitance). The hole mobilities determined from these measurements are plotted in Fig. 49. The nearly inverse relationship between mobility and carrier density reflects the very small change in the deduced conductivities.

8.4 DISCUSSION REGARDING HOLE MOBILITY MEASUREMENTS

The above results have amply demonstrated that high frequency admittance techniques can be used to obtain the resistivity of the undepleted region of the absorber in CIGS solar cells. Taken together with drive-level capacitance profiling measurements to determine the hole carrier densities, we are then able to estimate the hole mobilities directly within these working devices. This eliminates the need for depositing companion films on insulating substrates to examine the carrier mobility properties, at least over a restricted temperature range.

The experimental results reported above indicate fairly good agreement using this method as compared to coplanar measurements, but this is somewhat surprising. The lower carrier mobility in polycrystalline versus epitaxial CIGS films has been interpreted to imply the existence of potential barriers at grain boundaries that limit carrier transport.[48] However, because the grains are typically 1μm in size, and comparable to the thickness of our films, we would not expect such grain boundary effects to play as significant a role. Thus, the agreement between the coplanar and sandwich measurements of resistivity was not really expected. Further measurements are planned to try to understand the implications of this result.

9.0 CONCLUSIONS AND FUTURE DIRECTIONS

Our research for the High Performance Program under NREL Subcontract No. XAT-4-33624-08 has focused on four major activities. The first was directly related to our primary goal to assist in the development of higher bandgap absorbers in the CIS alloy system that might lead to higher efficiency multijunction devices. The second activity was to develop better numerical analysis tools so that we could extract more information from our capacitance profiling and admittance data. The third activity involved using metastable induced changes in the deep acceptor density in CIGS devices to test whether the deep acceptor defect was functioning as an important recombination center. Finally, by extending admittance measurements to higher frequencies, we have been able to develop a method to determine majority carrier mobilities directly within working CIGS solar cells.

In the first area we continued our work, in collaboration with Bill Shafarman at the IEC, to explore the suitability of absorbers with significant sulfur alloying as a possible route to wider gap, higher performance devices. We began with the characterization of several CISS quaternary samples without Ga, and then progressed to the characterization of a set of CIGSS pentenary alloy devices, all with bandgaps slightly in excess of 1.5eV. Within these first two sets of samples it appeared that those with S/(Se+S) fractions near 30at.% gave the best performance; for example, a $Cu(In_{0.49}Ga_{0.51})(Se_{0.67}S_{0.33})_2$ sample exhibited an open circuit voltage in excess of 820mV and a 10.5% efficiency. Our characterization of the electronic properties of these best absorbers indicated possible reasons for these variations in device properties: The Urbach energies for the highest efficiency devices were generally significantly smaller than for the others. Based upon these results we then examined a set of CIGSS samples with roughly 25at.% S/(Se+S) ratios and varying Ga fractions. Here a sample with a bandgap of 1.37 eV exhibited a V_{OC} in excess of 770meV and a 14.6% efficiency, while a sample with a bandgap of 1.44eV gave V_{OC} = 819mV and an efficiency of 13.0%. We note that in the former case we found a very narrow bandtail with an Urbach energy of only 22meV, the lowest of any sulfur containing alloy.

Our photocapacitance spectra also suggested that, although the dominant deep defect band of transitions was much broader in these CIGSS absorbers than in the CIGS absorbers, it also lay closer to the conduction band, and therefore was less likely to behave as an efficient recombination center compared to the higher bandgap CIGS devices. Indeed, we found that electrons excited into this dominant deep defect band in the sulfur containing alloys readily thermalize into the conduction band at moderate temperatures (above 200K) in contrast to the alloys containing no sulfur where we could not observe this. This means that the dominant defect band in the sulfur containing alloys is much less likely to behave as an efficient recombination center.

It thus appears that the potential for higher efficiency high bandgap devices within the CIGSS alloy materials remains fairly good. For example we found up to a 50mV improvement in open circuit voltage for the pentenary $Cu(InGa)(SeS)_2$ alloys with bandgaps above 1.4eV

compared to the Cu(inGa)Se_2 alloys. We also believe that further improvement in these pentenary alloys should be possible if we can overcome the limitations due to (1) low hole carrier densities that are often below the mid-10^{14} cm^{-3} in these materials, and (2) excessive alloy disorder that often leads to bandtails with Urbach energies exceeding 30meV. We have fairly conclusive evidence that improvements in these properties of the absorber properties would lead directly to increases in V_{OC}.

We also examined several CGS based devices from NREL, as well as a couple from IEC. We first examined the compositional uniformity of the CGS absorbers using our in-house TOF-SIMS facility and found a much greater non-uniformity in the Na spatial distributions in the IEC deposited CGS layers. This may partially account for the somewhat poorer performance of these samples compared to those fabricated at NREL. Indeed our DLCP studies also indicated much higher and more non-uniform densities of deep defects in the interior of the IEC absorbers and the device efficiencies. In general the performance of these 1.7eV bandgap CGS devices was not as good as the 1.52eV CIGSS devices primarily because of smaller values of J_{SC}, which one would expect from the larger bandgaps of the CGS devices, without the expected increase in V_{OC} that would compensate for this. However, our current sample set did not include any of NREL's highest performing CGS devices whose efficiencies have now exceeded 10%.[4]

Second, we have made major progress in our ability to numerical simulate the results of admittance, DLCP, and CV profiling measurements on thin film chalcopyrite devices. Our simulation programs are specifically designed to incorporate much large spatial variations in the electronic properties across the absorber than have previously been examined. In particular, we have been obtaining DLCP and CV profiling data in which the applied voltage is varied well into forward bias, and we believe these profiles contain significant information about defect states quite close to the barrier interface that our simulations should be able to extract. An example was given to illustrate this approach when applied to the data of one standard IEC high performance CIGS device. We also have preliminary evidence suggesting that the deep defects very close to the barrier interface may be the most important for predicting device performance.

Third, we have advanced our understanding of light-induced metastable changes in CIGS and then used this to learn about how the deep acceptor defect band affects the performance of actual devices. First we established in greater detail the one-to-one relationship between the increase in hole carrier density and deep acceptor density that followed prolonged light exposure. In particular, we examined the kinetics of these metastable changes in some detail and found that changes occurred under light exposure over very long periods of time with a sub-linear power law, and also a sub-linear power law intensity dependence. Based upon these observations, we explored possible defect creation rate equations. The most successful of these was one in which the initiating event involved the capture of two electrons into some initial precursor state, and possibly the $(V_{Se}\text{-}V_{Cu})^+$ complex that has been proposed by Lany and Zunger.

Using such metastable treatments to modify the carrier density and deep acceptor density within a single device, we decided to use this to understand the details of how CIGS cell

performance was impacted by changing the density of the deep acceptors (along with the hole carrier density). Indeed, we can increase these in a metastable fashion by up to a factor of 4 to 5. Examining the corresponding changes in the J-V curves, we typically observed a significant decrease in J_{SC} and fill-factor, but with almost no accompanying change in V_{OC}. Then, by using SCAPS modeling, we showed that such a result could *not* come about if the deep acceptor was acting as the only major recombination center in this device. After examining a host of other possibilities we determined that we could quite successfully account for our observations by a mechanism in which deep midgap (positive) donors were converted, via light soaking, into deep (neutral) acceptors (plus hole carriers). In such a scenario the net density of recombination centers would be nearly constant, and the observed changes in J_{SC} and fill-factor occurred simply because the depletion width became smaller as the deep acceptor and hole carrier densities were increased. This defect conversion model also seems consistent with the mechanism for metastable changes in CIGS proposed by Lany and Zunger.

We believe that the results of this study are valuable for several reasons. First, it demonstrates in detail how one can make the connection between the absorber electronic properties and the cell performance in a manner that is free of the usual ambiguities, such as differences in film morphology, junction properties, etc. This is because we are able to compare the device characteristics within a single device, with all of these other characteristics kept constant. Second, our results strongly argue against the belief of many in the CIGS community that the deep acceptor plays the sole dominant role in recombination. Third, it has also allowed us to estimate the minority carrier diffusion length in a very direct manner, and this is one of the most important parameters needed to understand current collection in CIGS devices.

The final (fourth) major accomplishment during our NREL Subcontract has been our development of high frequency admittance measurements to enable the determination of hole mobilities directly on working devices. This development required a lot of effort in the design of a new sample probe with an integrated current preamplifier and calibration capacitor so that we could be certain that we were measuring admittance accurately (up to nearly 100MHz). Our efforts proved successful, and we demonstrated that we could easily determine hole mobilities in the range 1 to 30 $cm^2 V^{-1} s^{-1}$ in CIGS samples.

Clearly there is still much left to be done before we can claim to have succeeded in our efforts to assist in the development of higher performance higher bandgap CIGS related alloys. However, we have shown that the approach using a significant degree of sulfur alloying still holds potential promise provided one can find ways to further improve alloy order in these materials, and increase their hole carrier densities somewhat. In addition, we have added substantially to our tools for better evaluating and understanding the performance of these devices. Here I refer specifically to our advances in computer modeling to obtain more detailed profiles of carrier and defect distributions, to our ability to understand cell performance via a better understanding of metastable effects in CIGS, and our ability to directly determine hole carrier mobilities within working devices.

10.0 SUBCONTRACT SUPPORTED PUBLICATIONS

1. JinWoo Lee, J. David Cohen, and William N. Shafarman, "The determination of carrier mobilites in CIGS photovoltaic devices using high-frequency admittance measurements", Thin Solid Films **480-481**, 336-340 (2005).

2. JinWoo Lee, Jennifer T. Heath, J. David Cohen, and William N. Shafarman, "Detailed study of metastable effects in the Cu(InGa)Se_2 alloys: Test of defect creation models", Mat. Res. Soc. Symp. Proc. **865**, 373 (2005).

3. Adam F. Halverson, Peter T. Erslev, JinWoo Lee, J. David Cohen, and William N. Shafarman, "Characterization of the electronic properties of wide bandgap $CuIn(SeS)_2$ alloys", Mat. Res. Soc. Symp. Proc. **865**, 519 (2005).

4. Adam Halverson, Shiro Nishiwaki, William Shafarman, J. David Cohen, "Electronic properties of wide bandgap pentenary chalcopyrite alloys and their photovoltaic devices", *Proceedings of the 2006 IEEE 4th World Conference on Photovoltaic Energy Conversion* (IEEE, Waikoloa Village, 2006), pp. 364-367.

5. JinWoo Lee, Jennifer T. Heath, J. David Cohen, and William N. Shafarman, "Role of bulk defect states in limiting CIGS device properties", in *Proceedings of the 2006 IEEE 4th World Conference on Photovoltaic Energy Conversion* (IEEE, Waikoloa Village, 2006), pp. 360-363.

6. Adam Halverson, Julian Mattheis, Uwe Rau, and J. David Cohen, "Reverse bias induced metastable effects in Cu(In,Ga)Se_2 photovoltaic devices", *Proceedings of the 2006 IEEE 4th World Conference on Photovoltaic Energy Conversion* (IEEE, Waikoloa Village, 2006), pp. 519-522.

7. JinWoo Lee, David Berney Needleman, William N. Shafarman, and J. David Cohen, "Understanding metastable defect creation in CIGS by detailed device modeling and measurements on bifacial solar cells", Mat. Res. Soc. Symp. Proc. **1012**, 223 (2007).

8. Adam Halverson, Shiro Nishiwaki, William Shafarman, and J. David Cohen, "Energetics of Both Minority and Majority Carrier Transitions through Deep Defects in Wide Bandgap Pentenary $Cu(In,Ga)(Se,S)_2$ Thin Film Solar Cells", Mat. Res. Soc. Symp. Proc. **1012**, 229 (2007).

9. Peter T. Erslev, Adam Halverson, William Shafarman, and J. David Cohen, "Study of the Electronic Properties of Matched Na-Containing and Reduced-Na $CuInGaSe_2$ Samples Using Junction Capacitance Methods", Mat. Res. Soc. Symp. Proc. **1012**, 445 (2007).

11.0 REFERENCES

1. W. N. Shafarman, R. Klenk, B. E. McCandless, J. Appl Phys. **79** 7324 (1996).
2. W. N. Shafarman, J. Zhu, Mat. Res Soc. Symp. Proc. **668** H2.3 (2001).
3. Mario Gossla and W.N. Shafarman, Thin Solid Films **480-481**, 33 (2005).
4. D. Young, J. Keane, A. Duda, J.A.M. AbuShama, C.L.Perkins, M. Romero, and R. Noufi, Prog. Photov: : Res. Appl **11**, 535 (2003).
5. D. L. Losee, J. Appl. Phys. **46**, 2204 (1975).
6. See, for example, T. Walter, R. Herberholz, C. Müller, and H. W. Schock, J. Appl. Phys. **80**, 4411 (1996).
7. D. L. Losee, J. Appl. Phys. **46**, 2204 (1975).
8. See, for example, T. Walter, R. Herberholz, C. Muller, and H. W. Schock, J. Appl. Phys. **80**, 4411 (1996).
9. M. Sakhaf and M. Schmeits, J. Appl. Phys. **80**, 6839 (1996).
10. C.E. Michelson, A.V. Gelatos, and J.D. Cohen, Appl. Phys. Lett. **47**, 412 (1985).
11. J.T. Heath, J.D. Cohen, and W.N. Shafarman, J. Appl. Phys. **95**, 1000 (2004).
12. A.V. Gelatos, K.K. Mahavadi, J.D. Cohen, and J.P. Harbison, Appl. Phys. Lett. **53**, 403 (1988).
13. J.D. Cohen, J.T. Heath, and W.N. Shafarman, in *Wide Gap Chalcopyrites*, ed. by U. Rau and S. Siebentritt, (Springer, 2005), in press.
14. A.F. Halverson, P.T. Erslev, JinWoo Lee, J.D. Cohen, and W.N. Shafarman, A. F. Mat. Res. Soc. Symp. Proc. **865**, 519 (2005).
15. J.T. Heath, J.D. Cohen, and W.N. Shafarman, J. Appl. Phys. **95**, 1000 (2004).
16. M. Turcu and U. Rau, Thin Solid Films **431-432, 158** (2003).
17. J.T. Heath, J.D. Cohen, W.N. Shafarman, D.X. Liao, and A.A. Rockett, Appl. Phys. Lett. **80**, 4540 (2002).
18. D. Kwon, C.-C. Chen, and J.D. Cohen, H.-C. Jin, E. Hollar, I. Robertson, and J.R. Abelson, Phys. Rev. B**60**, 4442 (1999).
19. S.H. Wei and A. Zunger, J. Appl. Phys. **78**, 3846, (1995)
20. T. Tiedje, Appl. Phys. Lett. **40**, 627 (1982).
21. K. Zhu, J. Yang, W. Wang, E.A. Schiff, J. Liang, and S. Guha, Mat. Res. Soc. Symp. Proc. **762**, 297 (2003).

22. V. Nadenau, G. Lippold, U. Rau, H. W. Schock, J. Crys. Growth **233**, 13 (2001).

23. M. R. Balboul, et. al., J. Vac. Sci. Technol. **A20**, 1247 (2002).

24. S. S. Hegedus, W. N. Shafarman, Prog. Photovolt: Res. Appl. **12**, 155 (2004).

25. V. Nadenau, U. Rau, A. Jasenek, H. W. Schock, J. Appl. Phys. **87**, 584 (2000).

26. R. Herberholz, et. al., Sol. Energy Mater. Sol. Cells **47**, 227 (1997).

27. P. J. Rostan, et. al., Sol. Energy Mater. Sol. Cells **90**, 1345 (2006).

28. A. Jasenek, U. Rau, V. Nadenau, H. W. Schock, J. Appl. Phys **87**, 594 (2000).

29. M. Gloecker, J. R. Sites, Thin Solid Films **480**, 241 (2005).

30. J.D. Cohen and D.V. Lang, Phys. Rev. B**25**, 5321 (1982).

31. J.T. Heath, J.D. Cohen, and W.N. Shafarman, J. Appl. Phys. **95**, 1000 (2004).

32. For a detailed discussion of the issue of dielectric freeze-out in CIGS films see: JinWoo Lee, J.D. Cohen, and W.N. Shafarman, Thin Solid Films **480-481**, 336 (2005).

33. S. Lany and A. Zunger, Phys. Rev. B **72**, 035215 (2005).

34. I.L. Repins, et. al., Prog. Photov. **14**, 25 (2006).

35. J.-F. Guillemoles, et. al., J. Phys. Chem. **B104**, 4849 (2000).

36. For an early example of these types of arguments to explain metastable defect creation in amorphous silicon see M. Stutzmann, W. Jackson and C. Tsai, Phys. Rev. B **32**, 23 (1982).

37. A.O. Pudov, et. al., Thin Solid Films **480-481**, 273 (2005).

38. J. Lee, J.D. Cohen and W.N. Shafarman, Thin Solid Films **480-481**, 336 (2005).

39. J. Lee, J. T. Heath, J.D. Cohen, and W.N. Shafarman, Mat. Res. Soc. Symp. Proc. **865**, 373 (2005).

40. U. Rau, K. Weinert, et. al.," Mat. Res. Soc. Symp. Proc. **668**, H9.1 (2001)

41. M. Gloeckler, J. Sites, and W. Metzger, J. Appl. Phys. **98**, 113704 (2005).

42. S.S. Hegedus and W.N. Shafarman, Prog. Photovolt: Res. Appl. **12**, 155 (2004).

43. See, for example, A.L. Fahrenbruch and R.H. Bube, *Fundamentals of Solar Cells* (Academic, New York, 1983), pp. 231-234, and references therein.

44. P. D. Paulson, R. W. Birkmire, and W. N. Shafarman, J. Appl. Phys. **94**, 879 (2003).

45. N.G. Dhere, M.C Lourenco; R.G. Dhere, L.L. Kazmerski, Solar Cells, **16** (1986). 369.

46. Y. Yamaguchi, Y. Yamamoto, T. Tanaka, Y. Demizu, and A. Yoshida, Jpn. J. Appl. Phys., **35** (1996) L1618.

47. D.J. Schröder, J.L. Hernandez, G.D. Berry, and A.A. Rockett, J. Appl. Phys., **83** (1998) 1519.

48. S. Siebentritt, A. Bauknecht, A. Gerhard, and U. Fiedeler, Sol. Energy Mat. and Sol. Cells, **67** (2001) 129.

49. M. Burgelman, P. Nollet, S. Degrave, Thin Solid Films **361-362,** 527 (2000).

50. M. Igalson and H.W. Schock, J. Appl. Phys., **80**, 5765 (1996).

51. U. Rau, M. Schmitt, J. Parisis, W. Riedl, F. Karg, Appl. Phys. Lett., **73**, 223 (1998).

REPORT DOCUMENTATION PAGE	*Form Approved OMB No. 0704-0188*

The public reporting burden for this collection of information is estimated to average 1 hour per response, including the time for reviewing instructions, searching existing data sources, gathering and maintaining the data needed, and completing and reviewing the collection of information. Send comments regarding this burden estimate or any other aspect of this collection of information, including suggestions for reducing the burden, to Department of Defense, Executive Services and Communications Directorate (0704-0188). Respondents should be aware that notwithstanding any other provision of law, no person shall be subject to any penalty for failing to comply with a collection of information if it does not display a currently valid OMB control number.

PLEASE DO NOT RETURN YOUR FORM TO THE ABOVE ORGANIZATION.

1. REPORT DATE *(DD-MM-YYYY)*	2. REPORT TYPE	3. DATES COVERED *(From - To)*
August 2008	Subcontract Report	27 April 2004 - 15 September 2007

4. TITLE AND SUBTITLE
Identifying the Electronic Properties Relevant to Improving the Performance of High Band-Gap Copper Based I-III-VI_2 Chalcopyrite Thin Film Photovoltaic Devices: Final Subcontract Report, 27 April 2004-15 September 2007

5a. CONTRACT NUMBER
DE-AC36-99-GO10337

5b. GRANT NUMBER

5c. PROGRAM ELEMENT NUMBER

6. AUTHOR(S)
J.D. Cohen

5d. PROJECT NUMBER
NREL/SR-520-43909

5e. TASK NUMBER
PVA72401

5f. WORK UNIT NUMBER

7. PERFORMING ORGANIZATION NAME(S) AND ADDRESS(ES)
Dept. of Physics and Materials Science Institute
University of Oregon
Eugene, Oregon

8. PERFORMING ORGANIZATION REPORT NUMBER
XAT-4-33624-08

9. SPONSORING/MONITORING AGENCY NAME(S) AND ADDRESS(ES)
National Renewable Energy Laboratory
1617 Cole Blvd.
Golden, CO 80401-3393

10. SPONSOR/MONITOR'S ACRONYM(S)
NREL

11. SPONSORING/MONITORING AGENCY REPORT NUMBER
NREL/SR-520-43909

12. DISTRIBUTION AVAILABILITY STATEMENT
National Technical Information Service
U.S. Department of Commerce
5285 Port Royal Road
Springfield, VA 22161

13. SUPPLEMENTARY NOTES
NREL Technical Monitor: Fannie Posey-Eddy

14. ABSTRACT *(Maximum 200 Words)*
This report summarizes the development and evaluation of higher-bandgap absorbers in the CIS alloy system. The major effort focused on exploring suitable absorbers with significant sulfur alloying in collaboration with Shafarman's group at the Institute of Energy Conversion. Three series of samples were examined; first, a series of quaternary CuIn(SeS)2-based devices without Ga; second, a series of devices with pentenary Cu(InGa)(SeS)2 absorbers in which the Se-to-S and In-to-Ga ratios were chosen to keep the bandgap nearly constant, near 1.52 eV. Third, based on the most-promising samples in those two series, we examined a series of devices with pentenary Cu(InGa)(SeS)2 absorbers with roughly 25 at.% S/(Se+S) ratios and varying Ga fractions. We also characterized electronic properties of several wide-bandgap CuGaSe2 devices from both IEC and NREL. The electronic properties of these absorbers were examined using admittance spectroscopy, drive-level capacitance profiling, transient photocapacitance, and transient photocurrent optical spectroscopies. The sample devices whose absorbers had Ga fraction below 40 at.% and S fractions above 20 at.% but below 40% exhibited the best electronic properties and device performance.

15. SUBJECT TERMS
PV; electronic properties; high bandgap; drive-level capacitance profiling; transient photocapacitance; admittance spectroscopy; chalcopyrite; thin film; devices; CIS alloys; CIGS

16. SECURITY CLASSIFICATION OF:			17. LIMITATION OF ABSTRACT	18. NUMBER OF PAGES	19a. NAME OF RESPONSIBLE PERSON
a. REPORT	b. ABSTRACT	c. THIS PAGE			
Unclassified	Unclassified	Unclassified	UL		19b. TELEPHONE NUMBER *(Include area code)*

Standard Form 298 (Rev. 8/98)
Prescribed by ANSI Std. Z39.18

F1146-E(09/2007)